Advances in the spectral modelling of wind waves in the nearshore

André van der Westhuysen

PROPOSITIONS

accompanying the thesis

Advances in the spectral modelling of wind waves in the nearshore

by André van der Westhuysen

1. The action limiter, used to enhance the stability of SWAN, does not significantly influence converged, stationary solutions produced by the model (this thesis).

2. The default criteria for run termination in SWAN often lead to non-converged solutions. Convergence is improved by using a criterion that is based on the curvature of the curve traced by the significant wave height as a function of the iteration level (this thesis).

3. A whitecapping dissipation expression that is a function of variables that are local in frequency space is more realistic in modelling the complex wave conditions occurring in coastal areas than commonly-used dissipation expressions that are functions of spectral mean variables (this thesis).

4. The performance of SWAN in the surf zone is significantly improved by replacing the LTA triad model with a two-equation expression that includes all resonant and near-resonant triad interactions (this thesis).

5. Considering the rapid advances in computational speed and capacity, the scarce development resources available to the wave modelling community should be assigned to improving the description of physical processes, rather than to developing computationally economical parameterisations.

6. In contemporary society, much creativity and many technological resources are spent on producing and consuming mass entertainment. It would benefit society much more if these resources were instead used to find creative solutions to the many problems that the world faces today.

7. There are two stages in scientific training: a first, in which one attempts to put the right dimensions to numbers and a second, in which one tries to do away with them again by non-dimensionalising.

8. Andy Warhol stated: 'In the future everybody will be famous for fifteen minutes'. In science, however, one can become famous forever—but then perhaps only to fifteen people.

9. A densely-researched field makes for a humble researcher.

10. The 'message in a bottle' is the original form of spam.

These propositions are considered defendable and as such have been approved by the supervisor, prof.dr.ir. J.A. Battjes.

STELLINGEN

behorende bij het proefschrift

Advances in the spectral modelling of wind waves in the nearshore

door André van der Westhuysen

1. De 'actie' begrenzer, die gebruikt wordt om de stabiliteit van SWAN te bevorderen, heeft geen significante invloed op de geconvergeerde resultaten van stationaire berekeningen van het model (dit proefschrift).

2. De standaard criteria voor het beëindigen van simulaties in SWAN leiden vaak tot niet-geconvergeerde resultaten. De convergentie wordt verbeterd door een convergentiecriterium te gebruiken gebaseerd op de kromming van de kromme gevormd door de significante golf-hoogte als functie van het iteratieniveau (dit proefschrift).

3. Een uitdrukking voor de dissipatie als gevolg van 'whitecapping' die een functie is van groot-heden die lokaal zijn in de frequentieruimte is meer realistisch in het modelleren van de complexe golfcondities in kustgebieden dan algemeen gebruikte dissipatie-uitdrukkingen, die functies zijn van spectraal gemiddelde grootheden (dit proefschrift).

4. De nauwkeurigheid van SWAN in de brandingzone wordt significant verbeterd door het LTA model voor drie-golf wisselwerking te vervangen door een twee-vergelijking model dat alle resonante en niet-resonante drie-golf wisselwerkingen bevat (dit proefschrift).

5. Gezien de snelle vooruitgang in de rekensnelheid en capaciteit van computers zouden de schaarse ontwikkelingshulpbronnen waarover de golfmodelleringsgemeenschap beschikt beter aangewend kunnen worden om de beschrijving van fysische processen te verbeteren dan om reken-efficiënte parameterisaties te ontwikkelen.

6. In de huidige maatschappij worden veel creativiteit en technologische hulpbronnen aange-wend om massavermaak te produceren en te consumeren. Het zou de samenleving veel meer baten indien deze hulpbronnen aangewend zouden worden om creatieve oplossingen te zoeken voor de vele problemen waarmee de wereld vandaag wordt geconfronteerd.

7. Er zijn twee stadia in de opleiding tot wetenschappelijk onderzoeker: een eerste, waarin ge-poogd wordt de juiste eenheden aan getallen toe te kennen, en een tweede, waarin geprobeerd wordt ze weer weg te halen door invoering van dimensieloze kentallen.

8. Andy Warhol heeft gezegd: 'In de toekomst zal iedereen beroemd zijn voor vijftien minuten'. In de wetenschap kan men echter beroemd worden voor altijd—maar dan misschien alleen maar in de ogen van vijftien mensen.

9. Een druk onderzocht vakgebied kweekt nederigheid bij onderzoekers.

10. Flessenpost is de oervorm van spam.

Deze stellingen worden verdedigbaar geacht en zijn als zodanig goedgekeurd door de promotor, prof.dr.ir. J.A. Battjes.

Advances in the spectral modelling of wind waves in the nearshore

Ontwikkelingen in het spectraal modelleren van windgolven in kustgebieden

Proefschrift

ter verkrijging van de graad van doctor
aan de Technische Universiteit Delft,
op gezag van de Rector Magnificus prof.dr.ir. J.T. Fokkema,
voorzitter van het College voor Promoties,
in het openbaar te verdedigen op dinsdag 16 oktober 2007 om 15:00 uur

door

André Jaco VAN DER WESTHUYSEN
Master of Science in Engineering, University of Stellenbosch
geboren te East London, Zuid-Afrika

Dit proefschrift is goedgekeurd door de promotor:
    Prof.dr.ir. J.A. Battjes

Samenstelling promotiecommissie:
    Rector Magnificus   voorzitter
    Prof.dr.ir. J.A. Battjes   Technische Universiteit Delft, promotor
    Prof.dr.ir. G.S. Stelling   Technische Universiteit Delft
    Prof.dr.ir. A.W. Heemink   Technische Universiteit Delft
    Prof.dr.ir. J.A. Roelvink   UNESCO-IHE / Technische Universiteit Delft
    Prof. J. Monbaliu   Katholieke Universiteit Leuven, België
    Dr. M. Benoit   EDF Division R&D, Frankrijk
    Dr. L. Cavaleri   ISMAR, Italië

Dr.ir. M. Zijlema heeft als begeleider in belangrijke mate aan de totstandkoming van het proefschrift bijgedragen.

Abstract

SWAN is a numerical model for the simulation of wind-generated waves in coastal regions. Application of SWAN to numerous idealised and field situations has proved the robustness and general good performance of the model, especially with respect to the prediction of wave height in both deep and shallow water. However, some inaccuracies and spurious behaviour remain. A characteristic inaccuracy of SWAN is a persistent underprediction of the wave period measures. These results are also affected by the presence of swell, which can cause a strong overprediction of wind sea growth in combined swell and wind sea conditions. In the surf zone, the reproduction of spectra tends to be rather inaccurate, leading to large scatter in the results of period measures. In addition to these concerns about model physics, some aspects of the numerical implementation of SWAN may negatively influence model outcomes. In particular, the so-called action limiter (used to enhance numerical stability) may affect model outcomes during stationary simulation.

The aim of the present study is to determine whether the general accuracy of SWAN can be improved by implementing alternative expressions for source terms in deep and shallow water, and by improving the numerical solution of the action balance equation. Two numerical aspects concerning stationary simulation are considered, namely the influence of the action limiter on model outcomes, and the criteria that determine when the iterative solution procedure should be ended. To this end, the outcomes of simulations using a number of numerical techniques for the integration of the source terms were compared, and the iteration behaviour of the model was studied. Concerning model physics, it was first investigated to what extent the accuracy of SWAN in deep water and water of finite depth can be improved by replacing the DIA quadruplet source term by an exact method that computes the full set of quadruplet interactions. Subsequently, it was investigated whether the accuracy of SWAN could be improved by using a whitecapping expression that, for breaking waves, is dependent on variables that are local in the frequency spectrum, as opposed to spectrally averaged. To improve model performance in the surf zone, a two-equation triad interaction model that includes all resonant and near-resonant interactions was implemented, for the reduced case of parallel depth contours. The performance of SWAN using this alterative triad source term was compared with the performance when using the LTA.

A major finding concerning the numerics in SWAN is that the action limiter does not significantly influence converged model results. A second important finding concerning stationary simulation is that the default convergence criteria are insufficient and can yield unconverged results that differ significantly from fully converged ones. Alternative, stricter convergence criteria are proposed. Concerning deep water source terms, it was found that replacing the DIA with an exact method for quadruplet interaction improves model performance somewhat, but is prohibitively expensive for operational applications. Model accuracy in deep and intermediate water depths is improved by using a whitecapping dissipation expression that, for breaking waves, is dependent on variables that are local in frequency space. The improvement in model performance is particularly evident under combined swell and wind sea conditions, where the default expression fails because of dependencies on mean spectral variables. Concerning shallow water source terms, it was found that the details of frequency spectra can be significantly improved through the use of a triad interaction source term that takes all sum and difference interactions into account. However, this model variant is significantly more computationally intensive than the default version (LTA).

Samenvatting

SWAN is een numeriek model voor het simuleren van door wind opgewekte golven in kust-gebieden. De toepassing van SWAN in talrijke geïdealiseerde situaties en praktijksituaties heeft de robuustheid en de relatief goede prestaties van het model bewezen, voornamelijk met betrekking tot de voorspelling van golfhoogtes in zowel diep als ondiep water. Enkele onnauwkeurigheden en onrealistische modelgedrag blijven echter bestaan. Een karakter-istieke onnauwkeurigheid van SWAN is een consistente onderschatting van periodematen. De resultaten hiervan worden ook beïnvloed door de aanwezigheid van deining, die juist een sterke overschatting van de zeegang kan veroorzaken in gecombineerde deining- en zee-gangcondities. In de brandingszone worden de spectra vaak onnauwkeurig weergegeven, wat leidt tot een grote spreiding in de resultaten van periodematen. Naast deze aspecten van modelfysica, kunnen enkele aspecten van de numerieke implementatie in SWAN de resultaten van het model negatief beïnvloeden. Met name de zogenaamde 'actie' begrenzer (gebruikt om de numerieke stabiliteit te verbeteren) zou de resultaten van het model in stationaire simulaties aan kunnen tasten.

Het doel van het onderhavige onderzoek is te bepalen of de algemene nauwkeurigheid van SWAN verbeterd kan worden door alternatieve formuleringen voor brontermen toe te passen in zowel diep als ondiep water, en door de numerieke oplossing van de actiebalans-vergelijking te verbeteren. Twee numerieke aspecten die betrekking hebben op stationaire simulaties worden beschouwd, namelijk de invloed van de 'actie' begrenzer op de resul-taten van het model en de criteria die bepalen wanneer de iteratieve oplossingsprocedure beëindigd moet worden. Hiertoe zijn de resultaten van simulaties met elkaar vergeleken met behulp van een aantal numerieke technieken voor het integreren van de brontermen en is het iteratiegedrag van het model onderzocht. Voor de modelfysica werd eerst onderzocht in hoeverre de nauwkeurigheid van SWAN in diep en ondiep water kan worden verbeterd door de DIA bronterm voor niet-lineaire vier-golf wisselwerkingen te vervangen door een exacte methode voor het berekenen van deze wisselwerkingen. Daarna werd er gekeken of de nauwkeurigheid van SWAN kon worden verbeterd door middel van een whitecap-ping formulering die, voor brekende golven, afhankelijk is van variabelen die lokaal zijn in de frequentieruimte, in tegenstelling tot een afhankelijkheid van spectraal gemiddelde grootheden. Om de prestaties van het model in de brandingszone te verbeteren, werd een twee-vergelijking model voor het berekenen van niet-lineaire drie-golf wisselwerkingen

(triades) toegepast, voor het gereduceerde geval van evenwijdige dieptelijnen, dat alle resonante en bijna-resonante wisselwerkingen bevat. De prestaties van SWAN met behulp van deze alternatieve triade bronterm werden vergeleken met de prestaties wanneer de standaard benadering (LTA) gebruikt werd.

Een belangrijke conclusie met betrekking tot de numerieke aspecten in SWAN is dat de 'actie' begrenzer de geconvergeerde resultaten van het model niet significant beïnvloedt. Een tweede belangrijke bevinding met betrekking tot stationaire simulatie is dat de standaard convergentiecriteria onvoldoende zijn en ongeconvergeerde resultaten kunnen opleveren, die aanmerkelijk verschillen van de volledig geconvergeerde resultaten. Er worden alternatieve, preciezere convergentiecriteria voorgesteld. Met betrekking tot brontermen voor diep water, is gevonden dat het vervangen van DIA door een exacte methode voor vier-golf wisselwerkingen de prestaties van het model enigszins verbetert. Het gebruik van deze methode is echter onbetaalbaar voor operationele toepassingen. De nauwkeurigheid van het model in diep water en intermediaire waterdieptes kan worden verbeterd door middel van een whitecapping dissipatie formulering die, voor brekende golven, afhankelijk is van variabelen die lokaal zijn in de frequentieruimte. De verbetering van de prestaties van het model is met name zichtbaar onder gecombineerde deining- en zeegangcondities, waarvoor de huidige uitdrukking ontoereikend is vanwege een afhankelijkheid van spectraal gemiddelde grootheden. Met betrekking tot brontermen voor ondiep water werd vastgesteld dat de details van de frequentiespectra significant kunnen worden verbeterd door gebruik van een triade bronterm die rekening houdt met alle som- en verschilinteracties. Deze variant van het model is echter aanmerkelijk rekenintensiever dan de LTA.

Contents

Chapter 1

Introduction

1.1   General background

The ocean's interior and boundaries play an important role in many human activities. The water system formed by ocean's interior is essential to transportation: most of the world's goods are moved by ship between the world's seaports, making the global economy of goods possible. The ocean also harbours vast amounts of the earth's remaining carbon-based energy reserves, and the ocean's sea life is an important source of food. The ocean's boundaries too are increasingly of importance. Today, humans are increasingly embracing coastal regions for their growing infrastructural needs. More than half the world's population lived within 200 km of a coastline in the year 2001. Three of the five largest cities of the world—Tokyo, Mumbai and New York City—are coastal (UN-Oceans 2007). Recent years have seen bold projects such as the Hong Kong International Airport, located on a large man-made island, and the offshore Palm Island holiday resorts in the United Arab Emirates of Dubai. It is therefore essential that coastal regions are managed well and sustainably developed. However, recent disasters, such as the devastation caused by Hurricane Katrina in New Orleans, have underlined the risks involved in such coastal habitation. Well-designed systems of coastal protection are thus required to protect human life and economic interests in highly-developed coastal regions. From an engineering point of view, an important element in the design of offshore rigs, structures for coastal protection and systems for ship routing and coastal management is the estimation of the environmental loads imposed by the ocean. An important forcing in this regard is wind-generated waves, of which reliable estimates are required for both the long term (e.g. wave climates for the design of structures) and the short term (e.g. wave forecasts for operational systems).

In this regard, the technology for obtaining reliable wind-wave predictions has been in development over the past 60 years. Sverdrup and Munk (1944a, b) and Bretschneider (1952) were the first to produce empirically-based growth curves of wave height and period

as functions of wind speed and fetch. A key development was the subsequent suggestion of Pierson *et al.* (1955) to analyse surface water waves as the sum of a large number of harmonic waves, in analogy to techniques applied in signal processing. This led to the development of so-called phase-averaged, spectral wind wave models that simulate the short-term statistics of the wave field, namely the variance density spectrum, rather than the phase-resolved surface displacement itself. (The variance density spectrum is formally defined as the Fourier transform of the auto-covariation function of the surface displacement.) When modelling on oceanic scale, this approach has the main benefit of allowing a much coarser spatial and temporal resolution to be used than if a phase-resolving approach were to be followed.

The development of spectral wind wave models has gone through three 'generations', stimulated by increasing knowledge of the generation processes and available computational resources (Young 1999). Gelci *et al.* (1957) produced the first spectral wind wave model by introducing the concept of a spectral energy balance equation. These and other first-generation models describe the generation and dissipation of energy in the wave spectrum and the transport of this energy in geographical space. The work of Phillips (1957) and Miles (1957) provided the theoretical basis for the modelling of wave generation, whereas wave breaking (whitecapping) was considered to dissipate all excess energy upon reaching an equilibrium level prescribed by an assumed universal spectral shape. Subsequently, a theoretical basis for the nonlinear interaction between frequency components was provided by Hasselmann (1962), and the results of the JONSWAP field experiment (Hasselmann *et al.* 1973) demonstrated the central role of four-wave (quadruplet) nonlinear interaction in the evolution of the spectrum. However, the full description of this process given by Hasselmann (1962) (the so-called exact calculation of quadruplet interaction) was too computationally expensive for operational models. Consequently, second-generation models included this process explicitly, but highly parameterised, as an additional term in the energy balance equation. Dissipation was handled in a similar way as in first-generation models.

Later, the development of a numerically efficient approximation of the quadruplet interaction expression, the Discrete Interaction Approximation (DIA) by Hasselmann and Hasselmann (1985), paved the way for third-generation models. Using the DIA, it became possible to solve the energy balance equation for operational application without any prior restrictions on the spectral shape. The first third-generation model was WAM (WAMDI Group 1988), which has been implemented for global wave prediction on oceans and shelf seas. Numerically, the transport part of the energy balance equation in WAM is implemented with an explicit upwind flux scheme, so that the size of the time step is limited by the Courant stability condition. Furthermore, the time step for the source term integration was limited to a size equal to or smaller than that of the propagation time step. This imposed a serious limitation to the extension of the WAM model to coastal application, since the high spatial resolution in shallow water required impractically small time steps. Monbaliu *et al.* (1999) partially remedied this situation by removing the link between the

source term integration time step and the Courant-limited propagation time step. This modification, together with the addition of a source term for depth-induced breaking and some additional adjustment to the numerics (Monbaliu *et al.* 2000), made it possible to extend the WAM model to coastal application with grid cell sizes down to the order of 1 km.

The first third-generation spectral model designed specifically for coastal application was SWAN (Ris 1997; Booij *et al.* 1999). SWAN uses the basic energy balance equation and source term expressions of WAM, but features two key alterations that make coastal application possible. The first of these is the substitution of the explicit propagation scheme by an implicit four-direction Gauss–Seidel scheme (Wesseling 1992). In this way, the Courant condition is removed, allowing the use of arbitrary spatial grid cell sizes (from 100 km, say, on the ocean to 10 m, say, in coastal regions and 10 cm in the laboratory). This provides the spatial resolution required to resolve spectral evolution in coastal regions and through the surf zone. The second alteration is the addition of depth-induced breaking (using Battjes and Janssen (1978)) and a parameterization of shallow water nonlinearity. Elgar and Guza (1985) show that at finite depths a set of three waves (a triad) can exchange energy amongst themselves, transporting energy from the spectral peak to both its sub- and superharmonics. A first attempt at describing these triad nonlinear interactions in terms of a spectral energy source term was made by Abreu *et al.* (1992). In contrast to the case with quadruplet interaction, no theory is available yet by which to describe triad interactions within a directional spectrum over fully two-dimensional varying topography. Available expressions, however, are prohibitively expensive to use in operational spectral wave models. Therefore, Eldeberky (1996) developed the Lumped Triad Approximation (LTA), a highly simplified, computationally cheap expression for the triad interaction term. Incorporating this expression in SWAN made it possible to model spectral evolution through the surf zone economically and with reasonable accuracy (Ris *et al.* 1999).

Initial versions of SWAN were designed for stationary application, using the time independent action balance equation (Ris 1997)). Stationary simulation is computationally cheaper and is acceptable in small-scale coastal applications where the residence time of the waves is shorter than the time scales of change of the forcing (Booij *et al.* 1999; Ris *et al.* 1999). Rogers *et al.* (2007) show that stationary simulation may even yield acceptable results on large scale shelf sea applications. Later versions of SWAN included the possibility of nonstationary simulation, using the time-dependent action balance equation. This made it possible to simulate rapidly changing coastal wave fields, such as hurricane waves. Subsequently, expressions for propagation over great circles were included and higher-order propagation schemes were implemented (Rogers *et al.* 2002). This allowed the extension of the computational domain to shelf and oceanic scale areas (e.g. Rogers *et al.* 2003), although here SWAN is computationally not as attractive as other ocean-scale models such as WAM.

1.2   Problem statement

Application of SWAN to numerous idealised and field situations has proved the robustness and generally good performance of the model, especially with respect to the prediction of wave height in deep and shallow water. However, experience with SWAN has also brought to light some inaccuracies and spurious behaviour. A characteristic problem experienced with the default version of SWAN is a persistent underprediction of the period measures of the spectrum (e.g. Ris *et al.* 1999; Rogers *et al.* 2003). Furthermore, these results are affected by the presence of swell in the simulation domain—the presence of swell can result in a strong overprediction of wind sea growth, and therefore lead to an *over*prediction of the period measures. In the surf zone, where the processes of depth-induced breaking and triad nonlinear interaction become dominant, the reproduction of spectra tends to be rather inaccurate, leading to large scatter in the results of period measures (Groeneweg *et al.* 2003). These findings can readily be related to the expressions used to model physical processes in SWAN.

In addition to these concerns about model physics, some aspects of the numerical implementation of SWAN may negatively influence model outcomes. In particular, it has been suggested that the so-called action limiter (a measure to enhance numerical stability) may affect model outcomes during stationary simulation, and should therefore be altered or removed (Haagsma and Otta 2001; De Waal 2001). There are therefore concerns about SWAN's performance in both deep and shallow water, which may have their roots in either the modelling of physical processes or in numerics. These issues need to be addressed in order to reliably apply SWAN to wave modelling studies.

1.3   Progress by others

The inaccuracies presented above, some of which SWAN shares with models for oceanic-scale application, have received various degrees of attention in the literature. A significant amount of attention has been given to the improvement of expressions for the source terms that are dominant in deep water and intermediate depth, namely quadruplet interaction, whitecapping dissipation and generation by wind. Concerning quadruplet interaction, improved algorithms for computing the full interaction expression of Hasselmann (1962) have been presented (e.g. Hashimoto *et al.* 2003; Van Vledder 2005). Also, extensions to approximate methods such as the DIA have been proposed, in order to improve their accuracy (Van Vledder 2001; Hashimoto and Kawaguchi 2001; Hashimoto *et al.* 2003; Benoit 2005). Schneggenburger *et al.* (2000) proposed to do away with the quadruplet interaction source term altogether, in favour of nonlinear dissipation. Concerning whitecapping dissipation, alterations to the Komen *et al.* (1984) expression have been proposed that would improve the prediction of period measures in pure wind sea (Rogers *et al.* 2003), and also improve

model performance in combined swell and wind sea conditions (Holthuijsen and Booij 2000; Bidlot *et al.* 2005). In addition, alternative whitecapping formulations have been proposed by Alves and Banner (2003), Hurdle and Van Vledder (2004) and, recently, Young and Babanin (2006). Wind input modelling has been refined in a number of respects. These include the increase of wave growth rates due to breaking-induced flow separation (Makin and Kudryavtsev 2002), the influence of swell on growth rates (Drennan et al. 1999; Chen and Belcher 2000; Kudryavtsev and Makin 2004), damping of wave energy by counter winds (e.g. Donelan 1999; Peirson et al. 2003) and, recently, the lowering of growth rates of young waves due to full separation of the air flow (Donelan *et al.* 2006).

Concerning wave modelling in the surf zone, significant progress has been made in the stochastic description of triad nonlinear interaction. As was noted above, generally applicable, isotropic expressions for triad interaction are still under active development. The triad interaction source term proposed by Abreu *et al.* (1992) is only valid for nondispersive, shallow water equations, and only for a one-dimensional wave field. Since then, the expressions have been extended in a number of respects. In terms of dispersion characteristics, models for moderately dispersive waves have been proposed (e.g. Herbers and Burton 1997), followed by models for fully dispersive waves (Agnon and Sheremet 1997; Janssen 2006). Models have also been extended with respect to the number of dimensions included: models such as that of Herbers and Burton (1997) include a full directional wave spectrum over one-dimensional topography, and the model of Janssen (2006) features a directional wave field over one-dimensional topography with weak lateral variation. As with quadruplet interactions, some computationally cheaper, parameterised expressions for triad interaction have been developed (Rasmussen 1998; Becq-Girard *et al.* 1999; Holthuijsen and Booij 2007).

Concerning the numerics of SWAN, two aspects have received attention recently, namely the accuracy of the propagation of energy in geographical space (Rogers *et al.* 2002) and the action density limiter (Haagsma and Otta 2001; De Waal 2001). All third-generation wave models require a limiter to be imposed on the amount of energy (or action) density change per computational increment, in order to remain stable using economically large computational steps. A number of studies have been done on the influence of the action limiter during nonstationary simulation of WAM and WAVEWATCH (Hersbach and Janssen 1999; Hargreaves and Annan 2001; Tolman 2002). These results are applicable to some degree to nonstationary simulation with SWAN. However, to date relatively little research has been done on the influence of the action limiter in stationary simulation in SWAN, except that Haagsma and Otta (2001) and De Waal (2001) considered it to act as an additional sink on the action balance equation.

1.4   Study objective and method

The aim of the present study is to investigate whether the general accuracy of SWAN can be improved by implementing alternative expressions for source terms in deep and shallow water, and by improving the numerical solution of the action balance equation. As a reference point, we consider SWAN version 40.20, released in August 2003, which will be referred to as the default model. In the selection of alternatives, in the first instance, no limits were imposed on the computational cost of the chosen methods—the gain in accuracy was investigated when using the theoretically most complete expressions for physical processes (for example nonlinear interaction) and expensive, but theoretically more accurate, numerical methods. Attempts were subsequently made to use the results of these initial investigations to develop variants of SWAN that would have superior accuracy but that would nonetheless be suitable for operational application.

The first step in achieving this aim was to investigate the influence of numerical solution procedure on the model accuracy. As mentioned above, the numerical implementation of the geographical propagation of energy in the action balance equation has been reviewed and improved recently (Rogers *et al.* 2002), but not the solution procedure for the source terms. Two aspects affecting the source term integration during stationary simulation are considered in the present study, namely the influence of the action limiter on model outcomes in deep and shallow water, and the criteria that determine when the iterative solution procedure should be ended. For this, the outcomes of simulations using three numerical techniques for the integration of the source terms were compared, namely action limiting, under-relaxation and nonstationary simulation with a small time step. Also, the iteration behaviour of the model was considered in detail, and based on these results, alternative criteria for run termination were investigated.

The second step in the study was to review the expressions used for the source terms. Sensitivity studies show that the source terms of wind input, whitecapping dissipation and quadruplet nonlinear interaction are dominant in deep water and at intermediate depth, whereas the source terms of bottom friction, depth-induced breaking and triad nonlinear interaction dominate in shallow water (e.g. Ris *et al.* 1999, Van Vledder 2001b and Groeneweg *et al.* 2004). Attention was therefore first given to deep water source terms, to improve model results in deep water and at intermediate depths. Since Hurdle (1998), Rogers *et al.* (2003) and Van Vledder *et al.* (2000) have shown that many of the model inaccuracies can be related to the deep water source terms of whitecapping dissipation and the DIA parameterisation for quadruplet interaction, attention was focussed on evaluating alternative expressions for these terms. It was first investigated to what extent the accuracy of SWAN in deep water and finite depth is compromised by using the DIA as opposed to a method that computes the full quadruplet interaction expression. For this purpose, model performance was investigated when using the WRT method (Webb 1978a,b; Tracy and Resio 1982), as reprogrammed by Van Vledder (2005b). Subsequently, it was investigated whether the accuracy of SWAN, in particular with regard to period measures, could be

improved by using a whitecapping expression that is dependent on variables that are local in the frequency spectrum, as opposed to spectrally averaged. For this, a whitecapping expression based on that of Alves and Banner (2003) was implemented and evaluated. The wind input source term was improved by replacing the empirical expression of Snyder *et al.* (1981) with that proposed by Yan (1987), which gives better estimates of growth rates for small wave ages.

In the surf zone, the source terms of triad nonlinear interaction and depth-induced breaking are dominant. Herbers *et al.* (2000) show that in the surf zone a balance develops between nonlinear transfer and depth-induced dissipation in the higher frequencies of the spectrum. Therefore, to improve the prediction of wave spectra and period measures in the surf zone, the source terms of both depth-induced breaking and triad interaction were considered. To investigate whether the prediction of spectra and the accuracy of period measures in the surf zone could be improved, a state-of-the-art two-equation triad interaction model by Janssen (2006) was implemented in SWAN. This model features full dispersion in linear shoaling and nonlinear couplings, and includes all sum and difference interactions in a directional wave spectrum. The model version applied is, however, limited to one-dimensional variation in topography. This triad expression is combined with a model for depth-induced breaking in which the distribution of the total dissipation is weighted by the frequency squared. This combination of first-principles computation of triad interaction and frequency-dependent depth-induced breaking is investigated as a benchmark for future model improvements for the surf zone, and is compared with the performance of a recalibrated LTA implementation.

1.5   Findings

A major finding concerning the numerics in SWAN involves the role of the action limiter in stationary simulation. It was found that the action limiter, although heavily used to maintain model stability, does not significantly influence the converged model result in either deep or shallow water conditions. This result implies that from a point of view of accuracy, alternative, less intrusive measures to ensure numerical stability, such as computationally expensive under-relaxation, are not necessary. However, the investigation did bring to light that the action limiter can significantly increase the number of iterations required for convergence in the surf zone. This is because the action limiter was designed on the basis of the self-similar deep water spectral shape, and therefore slows down the formation of harmonics in shallow water spectra. The second important finding involving the numerics of SWAN in stationary simulation is that the default stopping criteria, used for locating the point of model convergence and the appropriate point for run termination, are insufficient. These insufficient termination criteria can yield unconverged results which introduce significant error compared to fully converged outcomes. Alternative, stricter convergence criteria are proposed.

Concerning deep water source terms, replacing the DIA approximation in the default model with a method that computes the complete quadruplet interaction expression improves model performance in deep water and intermediate depth, but does not sufficiently account for all inaccuracies in fetch-limited spectra and parameters. Such a model variant is also computationally intensive, and not suitable to operational application. It was established that model accuracy in deep and intermediate water depths can be improved by combining the DIA with a whitecapping dissipation expression that, for breaking waves, is dependent on variables that are local in frequency space, and that dissipates more energy at higher frequencies than the default whitecapping expression of Komen *et al.* (1984). The improvement in model performance is particularly evident in combined swell and wind sea conditions, where the Komen *et al.* (1984) expression fails because of dependencies on mean spectral variables. This model variant is suitable for operational application. Combining the investigated wind input and whitecapping expression with the computation of the full quadruplet interaction expression yields some additional improvement in results, but at a disproportionately greater computational cost.

Concerning shallow water source terms, a major finding of this study was that the details of frequency spectra in SWAN can be significantly improved by implementing a state-of-the-art two-equation expression for triad nonlinear interaction. By taking all sum and difference interactions into account, energy levels in the spectral tail and at subharmonics are better reproduced than when using the computationally efficient LTA approximation. However, this model variant is significantly more computationally intensive than the LTA, and the implementation investigated in this study is defined for one-dimensional variation in topography (parallel contours) only, as opposed to the isotropic implementation of the LTA. This implementation of the two-equation triad model of Janssen (2006) can be considered a benchmark for later parameterisations. In this regard, it was found that the improved modelling of the spectral tail in shallow water, when used in combination with current expressions for deep water processes, leads to unexpected results that are not supported by observations. It appears that this model behaviour is caused by the way that quadruplet interaction is currently modelled in the surf zone.

1.6 Outline

The structure of this thesis is the following: Chapter 2 presents the action balance equation, gives a general description of the physical processes and details the numerical implementation of the default SWAN model. Chapter 3 describes the numerical investigations concerning the influence of the action limiter on model outcomes, the iteration behaviour of SWAN and stopping criteria. Chapter 4 deals with the deep water source terms of SWAN. Here the investigation of alternative expressions for wind generation, whitecapping dissipation and quadruplet nonlinear interaction is described. Chapter 5 considers the source terms dominant in shallow water, namely triad nonlinear interaction and depth-induced

breaking, for which alternatives are investigated. Chapter 6 presents the general conclusions of this study, which are discussed in Chapter 7. Chapter 8 concludes this thesis with recommendations.

Chapter 2

Model description

2.1 Introduction

The spectral wave model SWAN describes the evolution of wind waves by means of the action balance equation, which includes the propagation, generation and dissipation of wave energy. The action balance equation and its source terms are approximated numerically using finite differences, taken in temporal, geographical and spectral space. As general background to the model developments presented in this study, this chapter presents a description of the action balance equation, and gives an overview of its numerical implementation in SWAN.

2.2 The action balance equation

In SWAN, the evolution of the action density N (where $N = E/\sigma$, with E the variance density and σ the intrinsic radian frequency) is governed by the time-dependent wave action balance equation, which reads (Booij et $al.$ 1999):

$$\frac{\partial N}{\partial t} + \nabla_{\vec{x}} \cdot [(\vec{c}_g + \vec{U})N] + \frac{\partial c_\sigma N}{\partial \sigma} + \frac{\partial c_\theta N}{\partial \theta} = \frac{S_{tot}}{\sigma}\,, \qquad (2.1)$$

which can be reduced to a time-independent form by setting the time derivative $\partial N/\partial t$ to zero:

$$\nabla_{\vec{x}} \cdot [(\vec{c}_g + \vec{U})N] + \frac{\partial c_\sigma N}{\partial \sigma} + \frac{\partial c_\theta N}{\partial \theta} = \frac{S_{tot}}{\sigma}\,. \qquad (2.2)$$

The second term of (2.1) denotes the propagation of wave energy in two-dimensional geographical $\vec{x}$-space, with $\vec{c}_g$ the group velocity and $\vec{U}$ the ambient current velocity. This term can be recast in Cartesian, spherical or curvilinear coordinates. The third term represents the effect of shifting of the intrinsic radian frequency σ due to variations in depth and mean currents. The fourth term represents depth-induced and current-induced refraction. The quantities c_σ and c_θ are the propagation velocities in spectral space (σ, θ), in which θ is the wave propagation direction (see Ris 1997). The right-hand side contains the source term S_{tot} that represents all physical processes that generate, dissipate or redistribute wave energy. In water of finite depth, six processes contribute to S_{tot}:

$$S_{tot} = S_{in} + S_{wc} + S_{nl4} + S_{bot} + S_{surf} + S_{nl3} . \tag{2.3}$$

The terms on the right-hand side of (2.3) denote processes that generate, dissipate or redistribute wave energy. They represent, respectively, the transfer of energy from the wind to the waves, S_{in}, the dissipation of wave energy due to whitecapping, S_{wc}, the nonlinear transfer of wave energy due to quadruplet (four-wave) interaction, S_{nl4}, dissipation due to bottom friction, S_{bot}, dissipation due to depth-induced breaking, S_{surf}, and nonlinear transfer due to triad (three-wave) interaction, S_{nl3}.

In deep water, the processes of wind input, whitecapping dissipation and quadruplet nonlinear interaction form, together with the propagation terms, the primary spectral evolution balance in (2.1). The processes of wind input and whitecapping are modelled using the expressions of Komen *et al.* (1984); for quadruplet interaction the Discrete Interaction Approximation (DIA) of Hasselmann *et al.* (1985) is applied. In the default model, both the expressions for wind input and whitecapping dissipation are linear in the variance density, respectively adding and removing energy from the spectrum. Quadruplet interaction, on the other hand, is a nonlinear function of the variance density, and tends to impress a frontal shape (in frequency space) onto the spectrum. Quadruplet interaction therefore has a dominant role in imposing a self-similarity onto the wave spectra during all stages of development (Young and Van Vledder 1993).

In water of finite depth, the deep water processes are complemented by the processes of bottom friction dissipation, depth-induced breaking dissipation and triad nonlinear interaction. In intermediate depths, the balance in (2.1) can be considered to be between propagation, the deep water source terms and bottom friction. The latter process, inducing gradual energy loss from the spectrum, is modelled using the expression of Hasselmann *et al.* (1973). In the surf zone, the source terms of triad interaction and depth-induced breaking dominate the right-hand side of (2.1). Triad interaction produces characteristic shallow water spectra featuring sub- and superharmonics of the spectral peak (e.g. Elgar and Guza 1985). This process is approximated by the LTA of Eldeberky (1996). Depth-induced breaking dissipates energy over shoals and on the foreshore. It is modelled using the expression of Battjes and Janssen (1978). Extensive details on the formulations of

these processes can be found in Holthuijsen *et al.* (2006). A number of these formulations are reproduced in the following chapters, where relevant to the discussion.

In order to obtain a unique solution for (2.1), initial and boundary conditions should be provided. The incoming wave components at the offshore boundaries are specified by directional spectra. The closed boundaries (e.g. a coastline) are fully absorbing for wave energy leaving the geographical domain. The lower and upper boundaries in frequency space are indicated by $\sigma_{\min}$ and $\sigma_{\max}$, respectively. These boundaries are fully absorbing, although a f^{-4} diagnostic tail is added above the high-frequency cut-off, which is used to compute nonlinear wave-wave interactions and for computing integral wave parameters. Since the directional space is a closed circular domain, no boundary conditions are required.

2.3 Numerical framework

2.3.1 Discretisation

This section describes the main features of the discretisation and solution method of (2.1) in SWAN. For the sake of clarity, we shall restrict ourselves to Cartesian coordinates. Replacing the horizontal gradient operator $\nabla_{\vec{x}}$ by $(\partial/\partial x, \partial/\partial y)$ and the geographic velocity vector $\vec{c}_g + \vec{U}$ by (c_x, c_y), (2.1) can be rewritten as

$$
\frac{\partial N}{\partial t} + \frac{\partial c_x N}{\partial x} + \frac{\partial c_y N}{\partial y} + \frac{\partial c_\sigma N}{\partial \sigma} + \frac{\partial c_\theta N}{\partial \theta} = \frac{S_{tot}}{\sigma} \, .
\tag{2.4}
$$

We choose a rectangular grid with constant mesh sizes Δx and Δy in the x and y direction, respectively. The spectral space is divided into elementary bins with a constant directional resolution $\Delta\theta$ and a constant relative frequency resolution $\Delta\sigma/\sigma$ (resulting in a logarithmic frequency distribution). We denote the grid counters as $1 \leq i \leq \mathcal{M}_x$, $1 \leq j \leq \mathcal{M}_y$, $1 \leq l \leq \mathcal{M}_\sigma$ and $1 \leq m \leq \mathcal{M}_\theta$ in x, y, σ and θ spaces, respectively. All variables are located at points (i, j, l, m). Time discretisation is implemented with the implicit Euler technique. Hence the following approximation of (2.4) is obtained:

$$\frac{N_{i,j,l,m}^n - N_{i,j,l,m}^{n-1}}{\Delta t} +$$

$$\frac{[c_x N]_{i+1/2,j,l,m}^n - [c_x N]_{i-1/2,j,l,m}^n}{\Delta x} + \frac{[c_y N]_{i,j+1/2,l,m}^n - [c_y N]_{i,j-1/2,l,m}^n}{\Delta y} +$$

$$\frac{[c_\sigma N]_{i,j,l+1/2,m}^n - [c_\sigma N]_{i,j,l-1/2,m}^n}{\Delta \sigma} + \frac{[c_\theta N]_{i,j,l,m+1/2}^n - [c_\theta N]_{i,j,l,m-1/2}^n}{\Delta \theta} =$$

$$\frac{S_{tot}}{\sigma}\Big|_{i,j,l,m}^n , \tag{2.5}$$

where n is a time level with Δt a time step. Note that locations between consecutive counters are indicated by half-indices. Since the unknown values of N and the propagation velocities are only given at points (i, j, l, m), further approximation is needed. In Rogers *et al.* (2002), a number of higher-order upwind schemes are presented for the calculation of the fluxes $c_x N$ at $(i \pm 1/2, j, l, m)$ and $c_y N$ at $(i, j \pm 1/2, l, m)$. For simplicity, we present here a first-order upwind scheme in geographical space:

$$c_x N|_{i+1/2,j,l,m} = \begin{cases} c_x N|_{i,j,l,m} , & c_x|_{i,j,l,m} > 0 \\ c_x N|_{i+1,j,l,m} , & c_x|_{i+1,j,l,m} < 0 \end{cases} \tag{2.6}$$

and

$$c_y N|_{i,j+1/2,l,m} = \begin{cases} c_y N|_{i,j,l,m} , & c_y|_{i,j,l,m} > 0 \\ c_y N|_{i,j+1,l,m} , & c_y|_{i,j+1,l,m} < 0 \end{cases} . \tag{2.7}$$

The fluxes at $(i - 1/2, j, l, m)$ and $(i, j - 1/2, l, m)$ are obtained from (2.6) and (2.7) respectively by decreasing the indices by 1.

The approximations to the fluxes $c_\sigma N$ at $(i, j, l + 1/2, m)$ and $c_\theta N$ at $(i, j, l, m + 1/2)$ are usually obtained by combining central differences and a first order upwind scheme as follows:

$$c_\sigma N|_{i,j,l+1/2,m} = \begin{cases} (1 - \frac{1}{2}\mu)c_\sigma N|_{i,j,l,m} + \frac{1}{2}\mu c_\sigma N|_{i,j,l+1,m} , & c_\sigma|_{i,j,l,m} > 0 \\ \\ (1 - \frac{1}{2}\mu)c_\sigma N|_{i,j,l+1,m} + \frac{1}{2}\mu c_\sigma N|_{i,j,l,m} , & c_\sigma|_{i,j,l+1,m} < 0 \end{cases} \tag{2.8}$$

and

$$c_\theta N|_{i,j,l,m+1/2} = \begin{cases} (1 - \frac{1}{2}\nu)c_\theta N|_{i,j,l,m} + \frac{1}{2}\nu c_\theta N|_{i,j,l,m+1} , & c_\theta|_{i,j,l,m} > 0 \\ \\ (1 - \frac{1}{2}\nu)c_\theta N|_{i,j,l,m+1} + \frac{1}{2}\nu c_\theta N|_{i,j,l,m} , & c_\theta|_{i,j,l,m+1} < 0 \end{cases} , \tag{2.9}$$

where the parameters μ and ν are still to be chosen. Similar expressions can be found for the corresponding fluxes at $(i, j, l - 1/2, m)$ and $(i, j, l, m - 1/2)$ by decreasing the indices by 1.

For all values $\mu \in [0, 1]$ and $\nu \in [0, 1]$, a blended form arises between first-order upwind differencing ($\mu = \nu = 0$) and central differencing ($\mu = \nu = 1$). In the present study, we choose $\mu = \nu = 1/2$.

2.3.2 Solution algorithm

The discretisation of the action balance equation (2.1) as described in Section 2.3.1 yields a system of linear equations that need to be solved. The corresponding matrix structure can take various forms, depending mainly on the propagation of wave energy in the geographic space. For instance, suppose that $c_x > 0$ and $c_y > 0$ everywhere. Then, the matrix structure takes the following form:

$$
\begin{bmatrix}
\begin{pmatrix}
P & T & . & R & . & . & . \\
B & P & T & . & R & ., & . \\
. & B & P & T & . & R & . \\
L & . & B & P & T & . & R \\
. & L & . & B & P & T & . \\
. & . & L & . & B & P & T \\
. & . & . & L & . & B & P
\end{pmatrix} & & \\
\begin{pmatrix}
P & . & . & . & . & . & . \\
. & P & . & . & . & . & . \\
. & . & P & . & . & . & . \\
. & . & . & P & . & . & . \\
. & . & . & . & P & . & . \\
. & . & . & . & . & P & . \\
. & . & . & . & . & . & P
\end{pmatrix}
\begin{pmatrix}
P & T & . & R & . & . & . \\
B & P & T & . & R & . & . \\
. & B & P & T & . & R & . \\
L & . & B & P & T & . & R \\
. & L & . & B & P & T & . \\
. & . & L & . & B & P & T \\
. & . & . & L & . & B & P
\end{pmatrix} & \\
\begin{pmatrix}
P & . & . & . & . & . & . \\
. & P & . & . & . & . & . \\
. & . & P & . & . & . & . \\
. & . & . & P & . & . & . \\
. & . & . & . & P & . & . \\
. & . & . & . & . & P & . \\
. & . & . & . & . & . & P
\end{pmatrix}
\begin{pmatrix}
P & . & . & . & . & . & . \\
. & P & . & . & . & . & . \\
. & . & P & . & . & . & . \\
. & . & . & P & . & . & . \\
. & . & . & . & P & . & . \\
. & . & . & . & . & P & . \\
. & . & . & . & . & . & P
\end{pmatrix}
\begin{pmatrix}
P & T & . & R & . & . & . \\
B & P & T & . & R & . & . \\
. & B & P & T & . & R & . \\
L & . & B & P & T & . & R \\
. & L & . & B & P & T & . \\
. & . & L & . & B & P & T \\
. & . & . & L & . & B & P
\end{pmatrix}
\end{bmatrix}
\qquad (2.10)
$$

The sub-blocks on the main diagonal express coupling among the unknowns in the (σ, θ) space for each geographic grid point. Within each of these sub-blocks, the entries P on the diagonal represent the central bin in the stencil for the (σ, θ) space. The entries in the T and B bands represent adjacent bins in the θ dimension and the entries in the L and R bands represent adjacent bins in the σ dimension. Details on these follow below. The off-diagonal sub-blocks represent coupling across geographical grid points. This system can be solved in one step with a Gauss-Seidel technique (Wesseling 1992; Press *et al.* 1993). Generally, the velocities c_x and c_y may have different signs in the geographical domain and hence more steps are needed. However, it is well known that adapting the ordering of updates of the unknowns N in geographical space to the propagation direction can improve the rate of convergence of the Gauss-Seidel iterative procedure (Wesseling 1992). This is done as follows: for each time step and iteration, sweeping is carried out through grid rows and columns in geographical domain, starting at each of the four corners of the computational grid. The two upwave faces connecting at the geographic point (i, j), to be updated with its two upwave points, encloses those wave energy propagation directions that can be processed in the spectral space without having stability problems, i.e. without being subjected to a CFL stability criterion. This is illustrated in Figure 2.1. After four sweeps, wave energy has been propagated over the entire geographical domain. During each sweep, only a subset of the unknown values of N is updated, depending on the sign of c_x and c_y. For instance, the first sweep starts at the lower left-hand corner of the geographical domain and all grid points with $c_x > 0$ and $c_y > 0$ are updated.

After each propagation update at a geographic grid point, an update within a $90°$ quadrant of the spectral space is made. Because of the implicit nature of the spectral propagation terms in (2.5), a system of equations must be formed. Furthermore, due to the fact that the source term S_{tot} in (2.5) is nonlinear in N, linearisation is required in order to find a solution. Generally, the term S_{tot} in each bin (l, m) is dealt with by distinguishing between positive and negative contributions and arranging these in linear form (Ferziger and Perić 1999),

$$S_{tot} = S_{tot}^{+} + S_{tot}^{-} N \,, \tag{2.11}$$

where S_{tot}^{+} consists of positive contributions and S_{tot}^{-} of negative ones. Both contributions are independent of the solution N at the corresponding bin (l, m). Any negative term that does not contain N as a multiplier is first divided by N obtained from the previous iteration level (or time step) and then added to S_{tot}^{-}. This stabilizes the iteration process. Details on the application of this principle to each source term in SWAN can be found in Booij *et al.* (1999). As such, each difference equation (2.5) using expressions (2.8), (2.9) and (2.11) provides an algebraic relation between N at a particular bin and its nearest neighbours:

$$a_{\mathrm{P}} N_{\mathrm{P}} = a_{\mathrm{L}} N_{\mathrm{L}} + a_{\mathrm{R}} N_{\mathrm{R}} + a_{\mathrm{B}} N_{\mathrm{B}} + a_{\mathrm{T}} N_{\mathrm{T}} + b_{\mathrm{P}} \,, \tag{2.12}$$
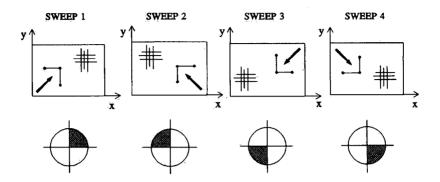
Figure 2.1: The solution procedure for wave energy propagation in geographical space with the appropriate directional quadrant (indicated by shaded area) for each of four sweeps (Ris 1997).

where P corresponds to central bin (l, m) and L(eft), R(ight), B(ottom) and T(op) correspond to $(l - 1, m)$, $(l + 1, m)$, $(l, m - 1)$ and $(l, m + 1)$, respectively. Furthermore, the coefficients a_k, $k \in \{P, L, R, B, T\}$ arise from the discretisations of the fluxes $c_\sigma N$ and $c_\theta N$ and b_P contains the positive contributions of the source term S_{tot}^+ in (2.11) and the updated fluxes $c_x N$ (2.6) and $c_y N$ (2.7). Note that coefficient a_P includes $-S_{tot}^-$. In case of an instationary simulation, a_P and b_P may contain the contributions of the time derivative $1/\Delta t$ and $N_{i,j,l,m}^{n-1}/\Delta t$, respectively.

The linear system of equations (2.12) for all bins within a directional quadrant at a particular geographical point is denoted by

$$A \vec{N} = \vec{b}, \tag{2.13}$$

where $A \in I\!\!R^{K \times K}$ contains the coefficients a_k, $k \in \{P, L, R, B, T\}$ (and corresponds to a sub-block on the main diagonal of (2.10)), $\vec{b} \in I\!\!R^K$ contains the coefficient b_P and boundary values and $\vec{N} \in I\!\!R^K$ denotes an algebraic vector containing the unknown action density values. Matrix A is non-symmetric. The dimension K equals $N_\sigma \times \frac{1}{4} N_\theta$, corresponding to the directional quadrant. Note that linearisation of the source term (2.11) enhances diagonal dominance of A, thereby improving numerical stability. Also note that neither A nor $\vec{b}$ depends on the unknowns. Each row in the matrix A corresponds to a bin (l, m). The main diagonal contains the coefficient a_P and directly to the left and right are the coefficients $-a_B$ and $-a_T$, respectively. The coefficients $-a_L$ and $-a_R$ are on the diagonals that are $\mathcal{M}_\theta$ positions to the left and right of the main diagonal, respectively.

The solution $\vec{N}$ is given by $A^{-1}\vec{b}$. Since the only non-zero matrix elements are situated in

five diagonals, iterative solution methods that utilize the sparsity of A optimally are very attractive. In SWAN, the solution of (2.13) is found by means of an incomplete lower-upper decomposition method followed by an iteration process called the Strongly Implicit Procedure (SIP) (Ferziger and Perić 1999). This procedure is specifically designed for (non-symmetrical) penta-diagonal systems and is relatively fast. Note that in the absence of mean current there are no shifts in the frequency, and consequently the structure of A reduces to a tri-diagonal one, i.e. $a_L = a_R = 0$, which can be inverted efficiently with the Thomas algorithm (Press et al. 1993; Ferziger and Perić 1999).

Due to refraction and nonlinear wave energy transfer, interactions occur between the directional quadrants. To properly take these interactions into account, as well as the fact that we employ the Gauss-Seidel technique and linearisation of the source term (2.11), the quadrant sweeping and the solution of system (2.13) need to be repeated until some convergence criteria are met. These criteria are presented and investigated in detail in Chapter 3. The iterative solution procedure is accelerated by calculating a reasonable first guess of the wave field based on the second-generation source terms of Holthuijsen and De Boer (1988).

Chapter 3

Accuracy of the numerical solution

3.1 Introduction

The accuracy with which formulations describing the physical processes involved in wave growth and propagation are approximated numerically is of crucial importance to assessing the predictive realism of spectral wave models. There is a need to separate these numerical errors from errors due to physical modelling. A common example of reducing numerical error is to ensure that wave energy is propagated accurately through geographical space in the model, which, as mentioned in Section 2.3.1, was investigated for SWAN by Rogers *et al.* (2002). Of equal importance is the accurate numerical implementation and solution of the source terms describing wave growth and decay. In this respect, third-generation wave models such as WAM (WAMDI Group, 1988; Komen *et al.* 1994), WAVEWATCH III (Tolman 1991) and SWAN pose a numerical difficulty caused by the presence of multiple time scales in the action balance equation (2.1). This is a reflection of the physical nature of wind waves, which consist of a wide range of frequencies. The ratio of the largest to the smallest time scale of spectral components is often large. When this is the case, the action balance equation (2.1) is called stiff (Press *et al.* 1993))[1]. Taking proper account of these time scales during the modelling of wave growth is a necessary condition for numerical accuracy. This would require the use of a very small time step in a numerical algorithm, which may be impractical. Moreover, the action balance equation is usually so stiff that its numerical implementation, combined with economically large time steps, often prevents a stable solution. In this respect, nonlinear four-wave interaction usually poses the biggest problem, since this process is associated with a high sensitivity to spectral change.

In a number of papers concerning spectral wave growth computation, numerical measures are proposed to achieve stable model results in an economical way. The WAMDI Group (1988) suggests the use of a semi-implicit time integration scheme with a time step that

---

[1] The equivalent situation for such an equation is to have eigenvalues of very different magnitudes.

matches the time scale of low-frequency waves. However, numerically stable solution of the resulting system of equations cannot be guaranteed (Press *et al.* 1993; Hargreaves and Annan 2001). The ratio of the largest eigenvalue to the smallest eigenvalue of the stiff system of equations, called the condition number, can be so large that even a fully-implicit method combined with large time steps does not yield a stable solution. Examples of this are provided by Hargreaves and Annan (2001). The only remedy is time-step reduction or under-relaxation, so that the modified system of equations has a spectrum of eigenvalues with a more favourable condition number.

To guarantee numerical stability at relatively large time steps in deep water applications, the so-called action density limiter was introduced in WAM in the early 1980s (Hersbach and Janssen 1999). This limiter restricts the change in the energy spectrum at each time step. Because low-frequency waves carry the most energy, it is desirable to solve the balance equation in this part of the spectrum accurately without intervention by the limiter, whereas, in deep water, using an equilibrium level may be considered sufficient for high-frequency waves. Although the technique of action limiting lacks a rigorous foundation and is not generally applicable or generally valid, it appears to guarantee numerical stability at relatively large time steps, even when these do not match the time scales of wave growth. Moreover, it is believed that the limiter does not affect the stationary solution when convergence is reached. This assumption is widely employed as a justification for the use of limiters. For an overview, we refer to Hersbach and Janssen (1999) and Tolman (2002), and the references quoted therein. Tolman (1992) proposes an alternative to the action density limiter in which the time step is dynamically adjusted where necessary to ensure accurate wave evolution. The calculation of this optimal time step is related to the action density limiter. Further details can be found in Tolman (1992, 2002).

Whereas the models WAM and WAVEWATCH III consider non-stationary problems on oceanic scales, with SWAN, wave propagation is often calculated within coastal regions by means of solving the time-independent wave action balance equation (2.2). This is considered to be acceptable, since the residence time of the waves in the coastal zone is expected to be far less than the time scale of variations of the ambient current, the wind or the tide (Booij *et al.* 1999). This steady-state solution in SWAN is obtained in an iterative manner, which can be regarded to be a time marching method with a pseudo time step. This pseudo time step generally does not match the relatively small time scale in frequency space and as a result divergence will occur. SWAN therefore makes use of the action density limiter also in time-independent simulation, to stabilise the iteration process (Booij *et al.* 1999). However, experience with SWAN has revealed that the limiter acts not only over the equilibrium frequencies, but also on the energy-containing part of the wave spectrum. This finding is confirmed by Tolman (2002). Furthermore, the limiter appears to be active over almost all spectra in the geographical domain, and during the entire iteration process. This activity has been associated with poor convergence behaviour, such as small-amplitude oscillation in integral parameters from one iteration to the next. Ris (1999) and Bottema (2001b) demonstrate that stationary SWAN results can be influenced

by the settings of the action limiter (if the limiter is not strict enough) whereas De Waal (2001) suspects that the limiter acts as a hidden sink in the source term balance at the equilibrium stage of depth-limited wave growth. In the present study we continue these initial investigations into the effect of the limiter on the solutions of stationary simulation with SWAN, and consider alternative means of model stabilisation.

An alternative means of restricting the high rate of change at higher frequencies is under-relaxation, i.e. making smaller updates by means of a much smaller (pseudo) time step (Ferziger and Perić 1999). As a result, a limiter may no longer be needed. Although this approach may be suitable to SWAN, it slows down convergence significantly. In this chapter, we propose a new method that finds a compromise between fast convergence on the one hand and minimizing the role of the limiter in the energetic part of the spectrum on the other. The key to achieving this is to link the extent of updating to the wave frequency—the larger the frequency, the smaller the update. This approach is therefore called frequency-dependent under-relaxation.

Unlike the oceanic scale models such as WAM and WAVEWATCH III, the application area of SWAN extends over shallow water and into the surf zone. The nature of the physical processes dominant here is significantly different to that of the deeper water processes discussed above. Whereas the processes in deep water—and quadruplet interaction in particular—have a sensitivity to the short time scales of the high spectral frequencies, those dominant in the surf zone, such as triad interaction and depth-induced breaking, are governed by the longer time scales of the spectral peak frequencies. There is therefore less need for a convergence enhancing measure active over the higher frequencies (such as action limiting) in this context.

Since the limiter was believed to influence the results of shallow water source terms, in earlier versions of SWAN it was partially deactivated in shallow water. To retain the very rapid but realistic decrease of wave energy in geographical space near the shore due to depth-induced breaking, Booij et al. (1999) deactivate the action limiter over negative spectral change when waves break. Because of a perceived influence of the action limiter on the reproduction of superharmonics in shallow water spectra, it was also deactivated where triad interaction is active—typically in the surf zone (Haagsma and Otta 2001). To avoid numerical instability, quadruplet interaction is deactivated along with the action limiter in these regions. However, Bottema (2001a, 2001b) shows that both these measures can lead to bad iteration behaviour during wave growth in shallow water, such as lakes, including unexpected growth bursts and oscillations in wave height and period. As a result, from version 40.20 of SWAN onward, the limiter is *always* active, and triad and quadruplet interaction are allowed to coexist. The implications of these model choices, in particular with regard to the impact of the action limiter on the reproduction of spectra in the surf zone, have not been sufficiently studied to date, and are considered here.

The second objective of this chapter concerns the formulation and the use of the termination criteria required by the iteration procedure in SWAN. In principle, the iterative process

should be ended if the convergence error, defined as the difference between the current iterate and the stationary solution, is smaller than a prescribed tolerance. At present, the stopping criteria in SWAN make use of the difference between successive iterates as a measure of the error in the converged solution. Experience in the application of SWAN has shown that the iteration process is often more erratic, and typically much slower than reported by Booij *et al.* (1999). As a result, the current stopping criteria often lead to the premature termination of simulations. This is due to the fact that, because of the relatively low rate of convergence, the convergence error is typically much larger than the difference between the successive iterates. A stopping criterion is proposed that uses the second derivative or curvature of the series of successive iterates of the calculated wave height. The premise is that this curvature approaches zero upon full convergence.

This chapter is structured as follows: Firstly, Section 3.2 describes the implementation of two convergence-enhancing measures, namely the action density limiter and the proposed frequency-dependent under-relaxation technique. Subsequently, Section 3.3 presents the default stopping criteria and the proposed criterion based on the curvature of the iterate series of the calculated wave height. In Section 3.4, the impact and effectiveness of the frequency-dependent under-relaxation technique and the new termination criterion are subsequently investigated by means of a series of SWAN simulations, featuring idealised fetch-limited cases and a number of depth-limited field cases. Section 3.5 closes this chapter with conclusions. The principal results of this chapter have been published by Zijlema and Van der Westhuysen (2005) and Van der Westhuysen *et al.* (2005).

3.2   Convergence-enhancing measures

As discussed in the introduction to this chapter, many time scales are involved in the evolution of wind waves. The high-frequency waves have much shorter time scales than the low-frequency waves, rendering the system of equations (2.13) stiff. If no special measures are taken, the need to resolve high-frequency waves at very short time scales would result in extremely long computational times. For economy, it is desirable to have a numerical technique that can be used with a large, fixed time step. For stationary problems, we are interested in obtaining the steady-state solution. Unfortunately, the convergence to the steady state is dominated by the smallest time scale and, in the absence of remedial measures, destabilizing over- and undershoots occur during the iteration process.

These oscillations arise because of the off-diagonal terms in matrix A, which can be dominant over the main diagonal, particularly when the ratio $\sigma_{\max}/\sigma_{\min}$ is large. As a result, convergence is slowed and divergence often occurs. To accelerate the iteration process without generating instabilities, appropriately small updates must be made to the level of action density. Below, two measures of achieving this goal are described, namely the action density limiter and frequency-dependent under-relaxation. The former, described

in Section 3.2.1, is the default method of convergence enhancement used in SWAN. The latter, described in Section 3.2.2, is the alternative method developed and investigated in this study.

3.2.1   Action density limiter

With the development of the WAM model, a so-called action density limiter was introduced as a remedy to the stability problems described above. This action limiter restricts the net growth or decay of action density to a maximum change at each geographic grid point and spectral bin per time step. This maximum change corresponds to a fraction of the omni-directional Phillips equilibrium level (Hersbach and Janssen 1999). In the context of SWAN (Booij *et al.* 1999), this is

$$\Delta N \equiv \gamma \frac{\alpha_{\mathrm{PM}}}{2\sigma k^3 c_g} , \tag{3.1}$$

where $\gamma \geq 0$ denotes the limitation factor, k is the wave number and $\alpha_{\mathrm{PM}} = 8.1 \times 10^{-3}$ is the Phillips constant for a Pierson-Moskowitz spectrum (Komen *et al.* 1994). Usually, $\gamma = 0.1$ (Tolman 1992)[2]. Denoting the total change in $N_{i,j,l,m}$ from one iteration, $s - 1$, to the next, s, after (2.5) by $\Delta N_{i,j,l,m}$, the action density at the new iteration level is given by

$$N^s_{i,j,l,m} = N^{s-1}_{i,j,l,m} + \frac{\Delta N_{i,j,l,m}}{|\Delta N_{i,j,l,m}|} \, \min\{|\Delta N_{i,j,l,m}|, \Delta N\} . \tag{3.2}$$

For wave components at relatively low frequencies, (3.2) yields the pre-limitation outcome of (2.5), because, for these components, the pseudo time step matches the time scale of their evolution. For high-frequency waves, however, (3.2) gives the upper limit for the spectrum to change per iteration due to the limiter (3.1). For typical coastal engineering applications, it is sufficient to compute the energy-containing part of the wave spectrum accurately. In other words, action densities in the region of the spectral peak should not be imposed by the limiter (3.1). However, experience with SWAN has shown that the limiter is active even close to the peak. Furthermore, during the entire iteration process, the limiter is typically active at almost every geographic grid point, as will be shown in Section 3.4.

---

[2]It should be noted here that the effective γ used in SWAN is not equivalent to that of WAM: the former is a factor 2π larger.

even though the converged solution has not yet been found. In particular, this happens when convergence is non-monotonic, such that the process is terminated at local maxima or minima that may not coincide with the converged solution.

3.3.2 Curvature-based stopping criteria

To deal with the difficulties described above, convergence criteria were sought that would impose a stricter requirement than simply fixed tolerances on the absolute change and the gradient of the series of successive iterates. In evaluating alternatives, it became apparent that, unlike H_{m0}, the quantity T_{m01} is not an effective variable on which to base stricter convergence criteria: It was found that the relative error in T_{m01}, i.e. $|T_{m01}^s - T_{m01}^{s-1}|/T_{m01}^{s-1}$, does not monotonically decrease near convergence, but reduces to a slow, small-amplitude oscillation during the iteration process (see e.g. Figure 3.17 below). This behaviour is due to small variations in the spectrum at high frequencies, something to which T_{m01} is sensitive. Since the rates of convergence of H_{m0} and T_{m01} are comparable due to the use of convergence-enhancing measures (e.g. Figures 3.4 and 3.7 below), the convergence speed of significant wave height can be considered representative for both these variables when stricter criteria are considered.

An alternative way of evaluating the level of convergence is to treat the sequence of iteration values $\{H_{m0}^1, H_{m0}^2, H_{m0}^3, ...\}$ as a continuous variable (an 'iteration curve'), and to evaluate the latter's second derivative, or curvature. Since the curvature of the iteration curve must tend towards zero as convergence is reached, terminating the iteration process when a certain minimum curvature has been reached would be a robust break-off procedure. The curvature of the iteration curve of H_{m0} may be expressed in the discrete sense as

$$\Delta(\Delta \tilde{H}_{m0}^s)^s = \tilde{H}_{m0}^s - 2\tilde{H}_{m0}^{s-1} + \tilde{H}_{m0}^{s-2}, \tag{3.8}$$

where $\tilde{H}_{m0}^s$ is some measure of the significant wave height at iteration level s. To eliminate the effect of small amplitude oscillations in the iteration curve on the curvature measure, we define $\tilde{H}_{m0}^s \equiv (H_{m0}^s + H_{m0}^{s-1})/2$. The curvature measure is made non-dimensional through normalisation with H_{m0}^s. The resulting curvature-based termination criterion at grid point (i, j) is then

$$\frac{|H_{m0}^s(i,j) - (H_{m0}^{s-1}(i,j) + H_{m0}^{s-2}(i,j)) + H_{m0}^{s-3}(i,j)|}{2H_{m0}^s(i,j)} < \varepsilon_{\mathrm{C}}, \quad s = 3, 4, ..., \tag{3.9}$$

where ε_{C} is a given maximum allowable curvature. Condition (3.9) must be satisfied in at least 98% of all wet grid points before the iterative process stops. This curvature requirement is considered to be the primary criterion. However, the curvature is zero if the

iteration curve is linear locally, passes through zero between local maxima and minima and, at convergence, the solution may oscillate between two constant levels due to the action limiter, whereas the average curvature is zero. As a safeguard against such situations, and also to guard against unexpected iteration behaviour of T_{m01}, the weaker criteria (3.5) and (3.6) are retained in addition to the stricter criterion (3.9).

3.4 Simulations

In this section, the alternative convergence-enhancing measures and stopping criteria described in Sections 3.2 and 3.3 are investigated by means of numerical simulation. To explore the comparative performance of the convergence-enhancing methods of action limiting and frequency-dependent under-relaxation, a number of idealised situations are considered. These include idealised fetch-limited wave growth, a field case representing near-idealised depth-limited wave growth and spectral evolution in the surf zone. In these tests, the convergence behaviour and the possible influence of the convergence-enhancing methods on the converged solution are of interest. Following this, attention is turned to the application of stopping criteria. The performance of the present and proposed curvature-based criteria is investigated for a diverse selection of situations, including fetch-limited wave growth and a number of shallow water field cases.

3.4.1 Convergence behaviour investigation

The first situation investigated is that of idealised, deep-water, fetch-limited wave growth over a fetch of 25 km, for spatially uniform wind with speeds of $U_{10} = 10$ and 30 m/s. The depth is set to 10^5 m. Simulations were conducted in one-dimensional, stationary mode, using a spatial discretisation of $\Delta x = 100$ m. The wave directions are discretised into 36 sectors each of 10 degrees. For the simulation with $U_{10} = 30$ m/s, the frequencies ranged from $f = 0.04$ to 1.0 Hz and were discretised into 34 bins, logarithmically distributed with $\Delta f / f \approx 0.1$. For the simulations with $U_{10} = 10$ m/s, the frequency range was shifted to $f = 0.06$–3.0 Hz to accommodate wave growth at higher frequencies. The simulations were conducted using the default third-generation physics formulations of SWAN (see Section 2.2). For the iteration behaviour up to convergence and beyond, the default stopping criteria (3.5) and (3.6) were disabled and iteration was continued up to a sufficiently large chosen maximum. The method of model convergence enhancement was varied for various runs. The following approaches were considered: (a) the application of the present default action limiter in SWAN ($\alpha = 0$, $\gamma = 0.1$), (b) using frequency-dependent under-relaxation in addition to the action limiter ($\alpha > 0, \gamma > 0$) and (c) applying frequency-dependent under-relaxation without the action limiter ($\alpha > 0$, $\gamma = \infty$). Various values of the under-relaxation parameter α were considered. To serve as a benchmark in these comparisons,
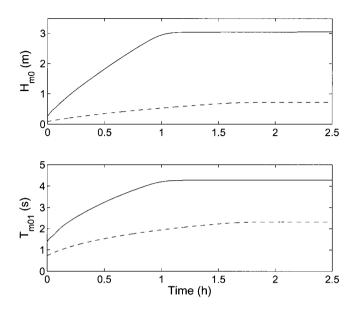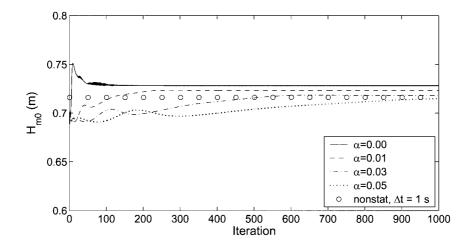
Figure 3.1: Deep-water, fetch-limited wave growth for wind speeds of $U_{10} = 10$ m/s (dashed line) and 30 m/s (solid), at fetch = 12.5 km. Results for nonstationary SWAN with $\Delta t = 1$ s and no limiter.

the test case of idealised wave growth was also calculated in nonstationary mode, using a very small time step of $\Delta t = 1$ s and no limiter[3]. The corresponding results, depicted in Figure 3.1, can be regarded as the true numerical solution of the problem. Note that the stationary solution is reached after approximately 7000 and 4000 time steps for the $U_{10} = 10$ and 30 m/s cases, respectively.

Firstly, the convergence behaviour in deep water, fetch-limited conditions is discussed when using the default value of the action limiter ($\gamma = 0.1$) and various moderate levels of under-relaxation ($\alpha = 0.00$–0.05). In these simulations, the run with $\alpha = 0$ represents the default SWAN result (base case). Figure 3.2 presents the iteration behaviour of H_{m0} for $U_{10} = 10$ and 30 m/s at a fetch of 12.5 km. As reference, the equilibrium-level results of the nonstationary benchmark simulations have been added. Figure 3.3 shows the lowest frequency bin at which the limiter was active during the simulation, for the various settings of α. It is noted that this minimum appears to be more or less independent of the spectral direction component (results not shown). With $\alpha = 0$ convergence is relatively fast, but

---

[3]For $U_{10} = 10$ m/s, the limiter (3.1) with $\gamma = 1.0$ was necessary to maintain stability at the highest frequency bin (3.0 Hz), but its impact was limited to this bin.
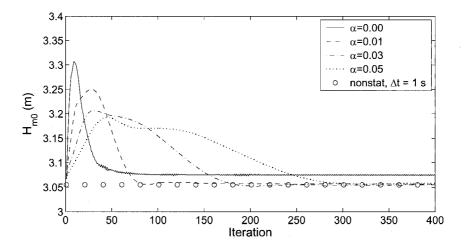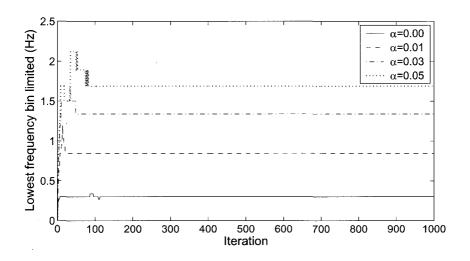
Figure 3.2: Convergence behaviour of H_{m0} in deep-water, fetch-limited simulations for wind speeds $U_{10} = 10$ m/s (top panel) and 30 m/s (bottom panel), at fetch = 12.5 km. Results for SWAN with $\gamma = 0.1$ and $\alpha = 0.0$–0.05. Also shown is nonstationary SWAN with $\Delta t = 1$ s.
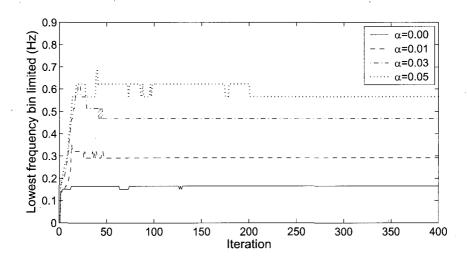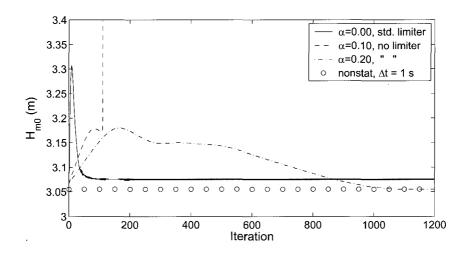
Figure 3.3: Lowest frequency bin at which limiter is active, as a function of iteration level. Results for deep-water, fetch-limited simulations for wind speeds $U_{10} = 10$ m/s (top panel) and 30 m/s (bottom panel), with $\gamma = 0.1$ and $\alpha = 0.0$–0.05.

the iteration curve features persistent small oscillations (Figure 3.2). Furthermore, the limiter was heavily used to obtain this fast convergence (Figure 3.3). The limiter was active throughout both the $U_{10} = 10$ m/s and 30 m/s simulations, up to wave periods above the highest values reached for T_{m01} (see Figure 3.1). Figures 3.2 and 3.3 also show the performance of the model variant featuring under-relaxation. Clearly, under-relaxation considerably slows down the speed of convergence, with the number of iterations required for convergence increasing with increasing values of α (Figure 3.2). For the setting $\alpha = 0.01$, the simulation with $U_{10} = 30$ m/s requires 100 iterations to converge, and that with $U_{10} = 10$ m/s requires about 250. For $\alpha = 0.05$, the number of iterations required for convergence increases to 300 and 1000 respectively. On the other hand, under-relaxation improves the iteration process on a number of points: firstly, the iterative behaviour is smoothed; secondly, the overshoot in significant wave height during iteration, observed in the default simulations, is reduced; thirdly, as shown in Figure 3.3, under-relaxation alters the activity of the limiter. At increasing levels of under-relaxation, the lowest frequency at which the updates are limited increases. This implies that the influence of the limiter on model results is reduced. In terms of numerical accuracy, the solutions of the simulations where $\alpha > 0.01$ are in good agreement with those of the nonstationary benchmark simulations (especially for higher values of α), whereas the $\alpha \leq 0.01$ simulations slightly over-estimates H_{m0}.

Considering the decreasing time scales at higher frequencies, convergence should be achievable solely by slowing down the updates of spectral energy change. This can be achieved by applying strong frequency-dependent under-relaxation. During such simulations, stable behaviour should be possible even with the limiter deactivated. Therefore, a next set of simulations was done for the idealised fetch-limited case, with under-relaxation of up to $\alpha = 0.20$, and with the limiter deactivated. Figures 3.4 and 3.5 present simulation results of H_{m0} and T_{m01} for $U_{10} = 30$ m/s, in which the nonstationary benchmark results are again displayed. The curves with $\alpha = 0$ again represent the standard SWAN result, obtained with the limiter ($\gamma = 0.1$). The remaining curves ($\alpha = 0.10$ and 0.20) show the effect of strong under-relaxation, without the use of the limiter ($\gamma = \infty$). At a relatively low level of under-relaxation ($\alpha = 0.10$), stability could not be achieved without the limiter. This represents the situation in which the pseudo time step still exceeds the time scales of spectral change. However, for intensified under-relaxation ($\alpha = 0.20$), the simulation does indeed remain stable, even in the absence of the limiter. As seen above, under-relaxation results in longer convergence times. For the strong under-relaxation applied here, convergence was only reached after 1000 iterations for the $U_{10} = 30$ m/s case (for $U_{10} = 10$ m/s, convergence was reached after 4000 iterations, results not shown). The result found here and above (Figure 3.2) that convergence is faster for the higher wind speed case is due to the fact that the ratio $\sigma_{max}/\sigma_{min}$ in the $U_{10} = 30$ m/s case is half of that in the $U_{10} = 10$ m/s case. As a result, the corresponding system of equations is less stiff, thus improving the convergence rate (see Section 3.2). Considering the growth curves of H_{m0} and T_{m01} for $U_{10} = 30$ m/s (Figure 3.5), excellent agreement is found between the results of the strongly under-relaxed, non-limited simulations and those of the nonstationary benchmark simulations. Similar results are found for $U_{10} = 10$ m/s (results not shown). This would suggest
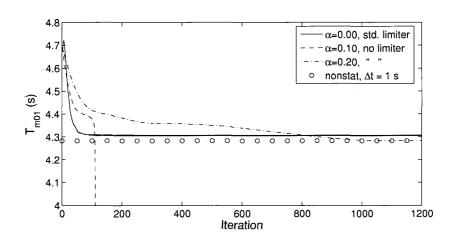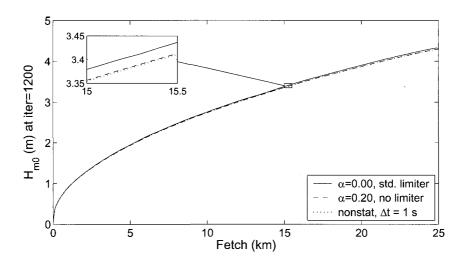
Figure 3.4: Convergence behaviour of H_{m0} (top panel) and T_{m01} (bottom panel) in deep-water, fetch-limited simulations for a wind speed of $U_{10} = 30$ m/s, at fetch $= 12.5$ km. Results for SWAN without limiter ($\gamma = \infty$) and various large under-relaxation factors ($\alpha = 0.10$–0.20). Also shown are stationary SWAN with $\gamma = 0.1$ and $\alpha = 0$, and nonstationary SWAN with $\Delta t = 1$ s.
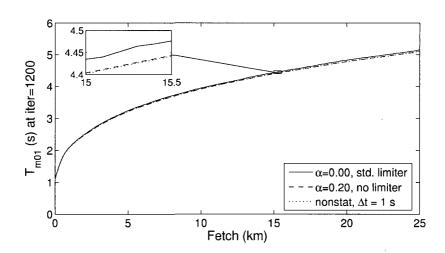
Figure 3.5: Growth curves of H_{m0} (top panel) and T_{m01} (bottom panel) in deep-water, fetch-limited simulations for a wind speed of $U_{10} = 30$ m/s. Results for stationary SWAN with limiter, for $\alpha = 0.20$ without limiter and nonstationary SWAN with $\Delta t = 1$ s.
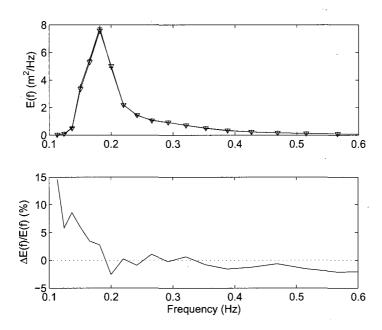
Figure 3.6: Spectra produced during deep-water, fetch-limited simulations with and without action limiter. Top panel: comparison between the converged results for the setting $\alpha = 0$ and $\gamma = 0.1$ (default limiter, line with plusses) and for the setting $\alpha = 0.20$ and $\gamma = \infty$ (under-relaxation and no limiter, line with triangles). (Note that all plusses virtually coincide with the triangles and for that reason are not separately visible.) Bottom panel: the difference between these results, expressed as $[E_{\gamma=0.1}(f) - E_{\gamma=\infty}(f)]/E_{\gamma=\infty}(f)$. Wind speed is $U_{10} = 30$ m/s and fetch is 12.5 km.

that by using frequency-dependent under-relaxation, a very good approximation of the true numerical solution is obtained.

Figure 3.5 shows that the results of the action-limited simulations also agree well with those of the under-relaxed and nonstationary simulations, with only small over-estimation of H_{m0} and T_{m01}. In analysing the origin of this minor discrepancy, it was observed that in the first few iterations the limiter ($\gamma = 0.1$) allows slightly larger growth of high-frequency energy compared to the frequency-dependent under-relaxation and nonstationary approaches. This energy is partly dissipated by whitecapping on a relatively long time scale and partly transported to lower frequencies by four-wave interactions on a significantly shorter time scale. At the point of convergence, it was found that the resulting spectra agree very well, except for the accumulation of some energy on the low-frequency face of the

spectral peak in the simulation using the action limiter (Figure 3.6). It is this accumulated energy that accounts for the small over-estimation of H_{m0} and T_{m01} observed. It will be shown below and in Chapter 4 that this small discrepancy is overshadowed by inaccuracies due to non-convergence and by variation in model outcome due to the use of alternative formulations for physical processes.

Considering the results of the two sets of simulations described above, a setting $\alpha = 0.05$, $\gamma = 0.5$ was chosen as a practical combination of frequency-dependent under-relaxation and the action limiter for field case application. For the idealised cases considered above, simulation results with this setting agree closely to those found with ($\alpha = 0.05$, $\gamma = 0.10$). With this combination, which lies between the extremes applied in the first and second simulation sets, the advantages of improved numerical accuracy and smooth convergence are obtained, while retaining a relatively fast convergence speed compared to the extreme example ($\alpha = 0.2$, $\gamma = \infty$). Next, the performance of this setting is investigated for the field case of Lake George in Australia. The Lake George field experiment of Young and Verhagen (1996a) represents near-idealised, depth-limited wave growth. Lake George is a shallow lake (depth about 2 m) with a nearly flat bottom and is approximately 20 km long and 10 km wide. Wave spectra were measured along the North-South axis of the lake using an array of eight gauges. The simulation of one representative case is presented here, which was recorded on 03/10/1993 at 17h00 local time. This case features wind-sea growth by a northerly wind of $U_{10} = 10.8$ m/s. At the downwind-most station, depth-limited wind-sea conditions of $H_{m0} = 0.42$ m and $T_p = 2.7$ s were observed. The simulations were conducted in two-dimensional stationary mode using a spatial discretisation of $\Delta x = \Delta y = 200$ m, a directional discretisation of $10°$, a frequency range of $f = 0.125$ to 1.0 Hz and a frequency discretisation of $\Delta f / f = 0.1$. The simulations were conducted using the default third-generation physics formulations of SWAN. Iteration was continued up to convergence and beyond, with the stopping criteria (3.5) and (3.6) disabled. Simulations were conducted with two settings of the convergence-enhancing methods, namely the default action density limiter ($\alpha = 0.0$, $\gamma = 0.1$) and the combination of under-relaxation and limiter $\alpha = 0.05$ and $\gamma = 0.5$.

The iteration curves of these simulations (Figure 3.7) show that the variant with the combination of under-relaxation and a weak limiter has smoother iteration behaviour, but only converges after about 300 iterations, which is considerably slower than with the default limiter. Nonetheless, the solutions of the two simulations converge to the same values. Figures 3.8 and 3.9 show comparative simulation results for these two convergence-enhancing methods after 500 iterations. It is striking that both in terms of spectra (Figure 3.8) and integral parameters (Figure 3.9) there is virtually no difference between the results produced without under-relaxation ($\alpha = 0$) and the action limiter at $\gamma = 0.1$, and with under-relaxation ($\alpha = 0.05$) and the action limiter at $\gamma = 0.5$. This correspondence would indicate that here too the action limiter has minimal influence on the simulation results. When comparing the two sets of simulation results to the observations, it is seen that total energy levels compare very well, but that there is a consistent overprediction of peak
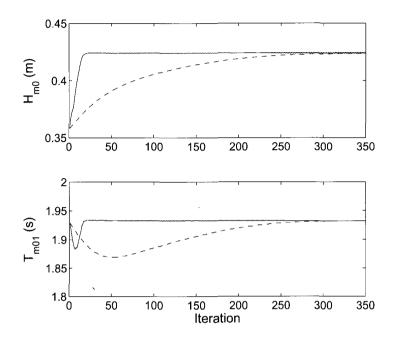
Figure 3.7: Lake George field experiment of near-idealised, depth-limited wave growth. Iteration curves at Station 8 for significant wave height (top panel) and mean period (bottom panel), for simulations with the setting $\alpha = 0.0$ and $\gamma = 0.1$ (default limiter, solid) and the setting $\alpha = 0.05$ and $\gamma = 0.5$ (strong under-relaxation and weak limiter, dashed). Wind speed is $U_{10} = 10.8$ m/s.

frequency. Having ruled out non-convergence and convergence-enhancing measures as possible explanations for this inaccuracy, the cause of the error must be sought elsewhere. We return to this subject in Section 3.5.

The simulations up to this point have considered deep and intermediate water situations, in which the source terms of wind input, whitecapping, quadruplet interaction and bottom friction play a dominant role. It was found above that in such situations the influence of the limiter on the converged solution is minimal. It may be argued that the limiter does not significantly affect the simulation of deep water spectra because the shape of the action limiter is based on the Phillips equilibrium tail (a deep water spectral shape), but that this result may not apply to shallow water spectra. In the surf zone, the source terms of triad nonlinear interaction and depth-induced breaking are dominant. Triad interactions transfer energy from the spectral peak towards higher frequencies, creating characteristic
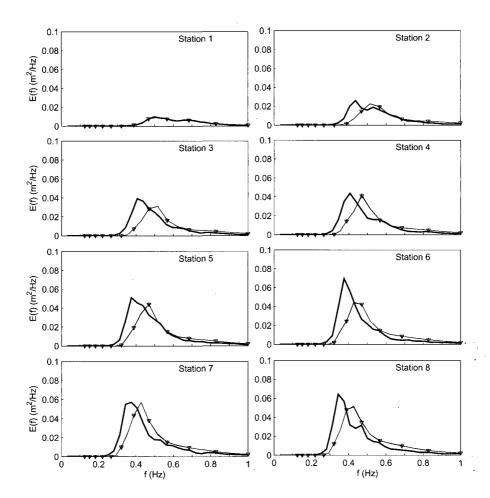
Figure 3.8: Lake George field experiment of near-idealised, depth-limited wave growth. Frequency spectra obtained with $\alpha = 0.0$ and $\gamma = 0.1$ after 500 iterations (plusses), with $\alpha = 0.05$ and $\gamma = 0.5$ after 500 iterations (triangles) and observations of Young and Verhagen (1996) (thick line). Note: all plusses virtually coincide with the triangles and for that reason are not separately visible.
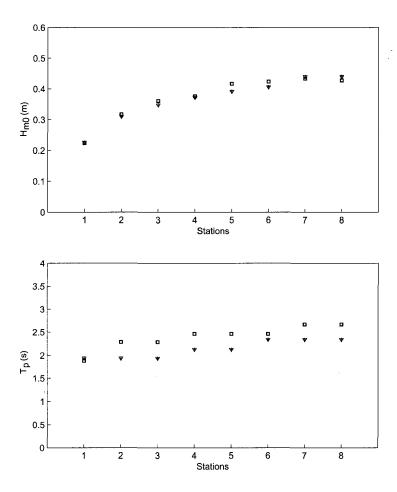
Figure 3.9: Lake George field experiment of near-idealised, depth-limited wave growth. Wave height and peak period obtained with $\alpha = 0.0$ and $\gamma = 0.1$ after 500 iterations (plusses), with $\alpha = 0.05$ and $\gamma = 0.5$ after 500 iterations (triangles) and observations of Young and Verhagen (1996) (squares). Note: all plusses virtually coincide with the triangles and for that reason are not separately visible.

shallow water spectra featuring a series of harmonics. Depth-induced breaking causes a high rate of energy dissipation, resulting in large energy losses over short spatial scales. It is not clear from the results presented above whether such shallow water spectra would be reproduced correctly would the action limiter be active in the surf zone. This issue is investigated here.
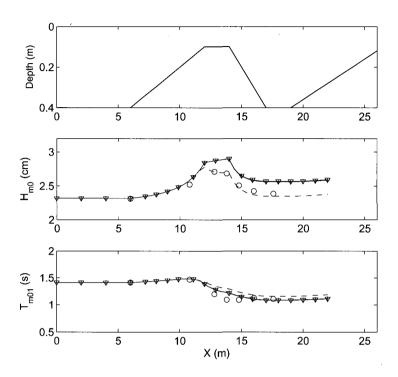
Figure 3.10: Spatial development of wave height and period during the iteration process of a case from the laboratory experiment of Beji and Battjes (1993). Top panel: Depth profile of the experiment. Middle and lower panels: Simulation results obtained with the setting $\alpha = 0.0$ and $\gamma = 0.1$ after 10 iterations (dashed) and 100 iterations (solid with plusses), and those obtained with $\alpha = 0.0$ and $\gamma = \infty$ upon convergence (after about 10 iterations, solid with triangles). Note: all plusses virtually coincide with the triangles and for that reason are not separately visible. Observations indicated by circles.

Firstly, the shallow water process of triad interaction is isolated, and the effect of the action limiter on the formation of harmonics is investigated. We consider a case from the laboratory flume experiment of Beji and Battjes (1993), which features waves propagating over a bar, creating bound sub- and superharmonics in the spectrum (Figure 3.10). The case considered features a JONSWAP spectrum with $H_{m0} = 2.3$ cm and $f_p = 0.5$ Hz generated by the wave maker. This case is simulated in SWAN using the Lumped Triad Approximation (LTA) algorithm (Eldeberky, 1996) for computing triad interaction. The only other source term active was depth-induced breaking, but it had a negligible influence on the results.
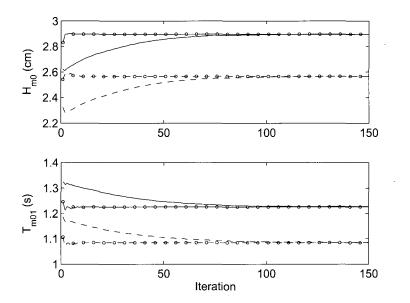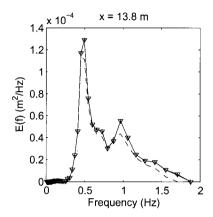
Figure 3.11: Iteration behaviour of wave height and period during the simulation of a case from the laboratory experiment of Beji and Battjes (1993). Shown are the results obtained with the setting $\alpha = 0.0$ and $\gamma = 0.1$ at $x = 13.8$ m (solid) and $x = 17.6$ m (dashed), and those obtained with $\alpha = 0.0$ and $\gamma = \infty$ at the same locations (solid and dashed respectively, with circles).

The discretisations used are $\Delta x = 0.1$ m in geographical space, $\Delta\,\theta = 0.5°$ in directional space (to capture the long-crestedness of the waves in the flume) and $\Delta\,f/f = 0.1$ in frequency space running from 0.01 to 2.5 Hz. Two sets of simulations were conducted: the first with the setting $\alpha = 0.0$ and $\gamma = 0.1$ (default limiter invoked) and $\alpha = 0.0$ and $\gamma = \infty$ (no limiter). Since the latter simulation does not feature any form of action limiting, it can be considered to be the true numerical solution and benchmark for this situation.

Figure 3.10 shows the spatial evolution of H_{m0} and T_{m01} during the simulation (at iteration 10) and at convergence for the Beji and Battjes case. It is seen that the wave height increases over the bar due to shoaling and decreases behind it. Due to the formation of higher harmonics, the mean period decreases strongly over the bar. Figure 3.11 shows the iteration behaviour of the two simulations at the end of the bar ($x = 13.8$ m) and some distance beyond the bar ($x = 17.6$ m). It can be seen that the simulations of both variants remain stable and that at both locations they converge to the same values. Figure 3.10 shows that the converged solutions of the two simulations agree over the entire simulation
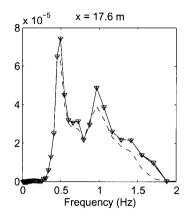
Figure 3.12: Iteration behaviour of frequency spectra at $x = 13.8$ m and $x = 17.6$ m during the simulation of a case from the laboratory experiment of Beji and Battjes (1993). Shown are the results obtained with the setting $\alpha = 0.0$ and $\gamma = 0.1$ after 10 iterations (dashed) and 100 iterations (solid with plusses), and those obtained with $\alpha = 0.0$ and $\gamma = \infty$ upon convergence (after about 10 iterations, solid with triangles). Note: all plusses virtually coincide with the triangles and for that reason are not separately visible.

domain. These results confirm that the limiter is not required here in order to ensure numerical stability, and that when the limiter is indeed used, it does not affect the converged solution. Figure 3.11 shows that the limiter does, however, have a distinct influence on the iteration behaviour of the simulation: the simulation without limiter ($\gamma = \infty$) converges after about 10 iterations, whereas the simulation with limiter ($\gamma = 0.1$) requires about 100 iterations. Figure 3.10 shows that after 10 iterations the solution of the $\gamma = 0.1$ simulation significantly differs from (lags behind) the converged solution across the entire length of the flume. Figure 3.12 presents the simulated frequency spectra at the end of the shoal ($x = 13.8$ m) and beyond it ($x = 17.6$ m), for the two sets of simulations. In the spectra of the $\gamma = 0.1$ simulation the first superharmonic is slow to develop due to the influence of the limiter, leading to the underprediction of H_{m0} and T_{m01} during the early stages of iteration. Nonetheless, upon convergence the spectra of the $\gamma = 0.1$ simulation agree with those of the non-limited simulation. Finally, we remark that the converged results shown in Figure 3.10 differ from the observations, especially in terms of the significant wave height. Having ruled out non-convergence and the limiter as sources of inaccuracy, we conclude that the remaining errors are due to the description of physics in the model (see Section 3.5).
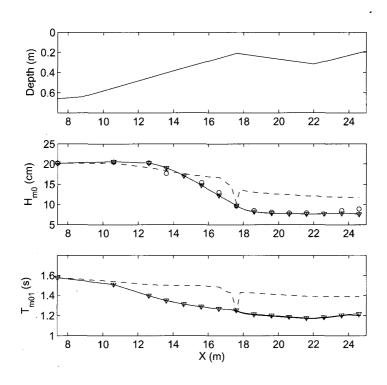
Figure 3.13: Spatial development of wave height and period during the iteration process of a case from the laboratory experiment of Battjes and Janssen (1978). Top panel: Depth profile of the experiment. Middle and lower panels: Simulation results obtained with the setting $\alpha = 0.0$ and $\gamma = 0.1$ after 50 iterations (dashed) and 1200 iterations (solid with plusses), and those obtained with $\alpha = 0.0$ and $\gamma = \infty$ upon convergence (after about 25 iterations, solid with triangles). Note: all plusses virtually coincide with the triangles and for that reason are not separately visible. Observations indicated by circles.

The second shallow water situation investigated is the combined modelling of triad interaction and depth-induced breaking in the surf zone. Here, a case from the laboratory flume experiment of Battjes and Janssen (1978), featuring nonlinear shoaling and violent depth-induced breaking over a barred beach profile, is considered (Figure 3.13). This case has a boundary condition of $H_{m0} = 20$ cm and $f_p = 0.625$ Hz, which is generated at the wave maker. This case was simulated in SWAN using the LTA and the depth-induced breaking expression of Battjes and Janssen (1978). The discretisations used are $\Delta x = 0.1$ m in geographical space, $\Delta \theta = 0.5°$ in directional space (to capture the long-crestedness of the
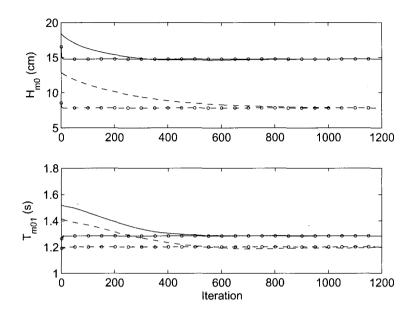
Figure 3.14: Iteration behaviour of wave height and period during the simulation of a case from the laboratory experiment of Battjes and Janssen (1978). Shown are the results obtained with the setting $\alpha = 0.0$ and $\gamma = 0.1$ at $x = 15.6$ m (solid) and $x = 23.6$ m (dashed), and those obtained with $\alpha = 0.0$ and $\gamma = \infty$ at the same locations (solid and dashed respectively, with circles).

waves in the flume) and $\Delta f/f = 0.1$ in frequency space running from 0.25 to 3.57 Hz. The same two sets of simulations as above are considered, namely the setting $\alpha = 0.0$ and $\gamma = 0.1$ (default limiter invoked) and $\alpha = 0.0$ and $\gamma = \infty$ (no limiter). Again, the latter setting can be considered to be the true numerical solution and benchmark for this situation.

Figure 3.13 shows the spatial evolution of significant wave height and mean period during the simulations and at convergence. For this situation the simulated wave height strongly decreases over the bar, accompanied by a decrease in the mean period. The converged results of H_{m0} agree well with the observations (observations of T_{m01} are not available). Figure 3.14 shows the iteration curves of the solution at a location just offshore of the bar ($x = 15.6$ m) and on the foreshore ($x = 23.6$ m). It can be seen that here too both sets of simulations remain stable, and that they converge to the same values. This is true for the entire computational domain (Figure 3.13). This result confirms that, also when the the process of depth-induced breaking is included, the limiter is not required for numerical
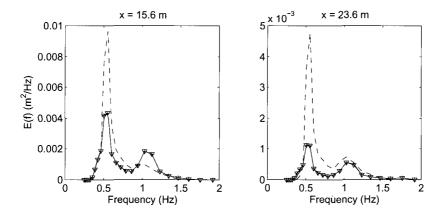
Figure 3.15: Iteration behaviour of frequency spectra at $x = 15.6$ m and $x = 23.6$ m during the simulation of a case from the laboratory experiment of Battjes and Janssen (1978). Shown are the results obtained with the setting $\alpha = 0.0$ and $\gamma = 0.1$ after 50 iterations (dashed) and 1200 iterations (solid with plusses), and those obtained with $\alpha = 0.0$ and $\gamma = \infty$ upon convergence (after about 25 iterations, solid with triangles). Note: all plusses virtually coincide with the triangles and for that reason are not separately visible.

stability, nor does it influence the converged solution when it is indeed used. However, Figure 3.14 reveals that the addition of strong depth-induced breaking significantly increases the number of iterations that the $\gamma = 0.1$ simulation requires for convergence (compare with Figure 3.11). Figure 3.13 shows that, except at the crest of the bar, many iterations are required to reduce energy levels to those prescribed by the physics. Figure 3.15 presents the simulated spectra at the upslope of the bar ($x = 15.6$ m) and on the foreshore ($x = 23.6$ m) after 50 iteration and upon convergence. At the upslope of the bar, the limiter slows down the dissipation of the peak and also the formation of the first harmonic. At the foreshore, the limiter slows down the reduction in energy across the spectrum by strong depth-induced breaking. Yet, upon convergence, the spectra produced by the limited ($\gamma = 0.1$) and non-limited ($\gamma = \infty$) simulations agree.

The results of the convergence investigation for the surf zone indicate that, contrary to earlier reports (e.g. Haagsma and Otta 2001), the limiter does not influence the converged model results in the surf zone. Consequently, there is no need to deactivate the limiter in shallow water from the point of view of accuracy. However, applying the action limiter in the surf zone was found to significantly slow down the convergence process. Unlike for the deep water situations, no convergence-enhancing methods (neither action limiting nor under-relaxation) are required to ensure stable simulation with the source terms of triad interaction and depth-induced breaking, as has been discussed in Section 3.1. Therefore, if only shallow water source terms would be active, deactivating the action limiter would improve the convergence speed considerably. However, since in shallow water field cases the deep water source terms are typically also active, we refrain from the partial deactivation of the limiter here, as has also been recommended by Bottema (2001a).

3.4.2   Termination of the iterative process

In Section 3.4.1 it was shown that in stationary simulation of deep water and finite depth situations, the convergence-enhancing methods of action limiting and frequency-dependent under-relaxation yield very similar results upon convergence. By making use of under-relaxation in this way, it was established that the default action limiter has little influence on the converged outcome of simulations. Similarly, in the surf zone, application of the action limiter was found not to affect the converged solution. However, for operational application it is also important to be able to accurately identify the point at which these converged solutions are reached. The question that remains, therefore, is whether, in practical applications in which a stopping criterion and significantly fewer iterations are used, such well-converged results are obtained.

Next, the current default stopping criteria of SWAN are compared to the criteria proposed in Section 3.3. For this, the performances of the two stopping criteria were compared for a collection of 14 cases, featuring a diverse selection of idealised and field situations, taken from the so-called ONR Testbed (Ris *et al.* 2002). These situations include idealised, fetch-
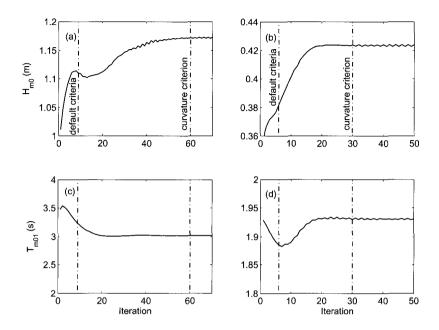
Figure 3.16: Iteration behaviour and location of break-off points for a field case from the Haringvliet Estuary (left hand panels) and from Lake George (right-hand panels). Shown are the positions of run termination using the default stopping criteria (3.5) and (3.6) with $\varepsilon_H^r = \varepsilon_T^r = 0.02$, $\varepsilon_H^a = 0.02$ m and $\varepsilon_T^a = 0.2$ s (after 6 iterations) and criteria (3.5), (3.6) and (3.9) with $\varepsilon_C = 2\mathrm{e}\text{-}4$ (after 30 iterations).

limited wave growth, and field cases observed at Lake George in Australia (near-idealised, depth-limited growth), the Haringvliet Estuary in The Netherlands and the Norderneyer Seegat in Germany (barrier island system). These cases were all simulated using only the default action limiter ($\alpha = 0.0, \gamma = 0.1$) as a convergence enhancement measure, which was active at all times and locations. A first set of simulations was conducted with the default stopping criteria (3.5) and (3.6), and a second set with the newly-proposed curvature-based criteria (3.5), (3.6) and (3.9), using $\varepsilon_H^r = \varepsilon_T^r = 0.02$, $\varepsilon_H^a = 0.02$ m and $\varepsilon_T^a = 0.2$ s, and two values for the minimum curvature ε_C.

Figure 3.16 shows the iteration behaviour of the Lake George field case (at Station 8) considered in the previous section, as well as a field case from the Haringvliet Estuary (at its downwind-most observation station). Also indicated on Figure 3.16 are the termination points determined by the default stopping criteria (3.5) and (3.6) and the proposed criteria
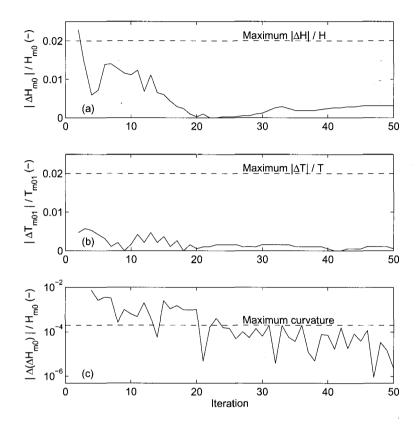
Figure 3.17: Absolute values of the gradient measures of H_{m0} and T_{m01} (panels (a) and (b)) and the normalized average curvature of H_{m0} (panel (c)) at a single grid point for Lake George, plotted against iteration level. The default value of the maximum gradient (2%) and a maximum curvature level of $\varepsilon_C = 2e\text{-}4$ are also indicated.

(3.5), (3.6) and (3.9) using $\varepsilon_C = 2e\text{-}4$. The iteration curves of H_{m0} and T_{m01} feature characteristic local minima and maxima and small-amplitude oscillations. These occur because of nonlinearities in the source term balance. As a result, the default, gradient-based criteria typically terminate iteration at local maxima or minima, or at local decreases in gradient before convergence is reached. For example, the default criteria prematurely terminate the Lake George simulation at the 6$^{\text{th}}$ iteration, resulting in about 10% underprediction of the converged value for H_{m0}. By contrast, the curvature-based criteria with $\varepsilon_C = 2e\text{-}4$

terminate the simulation at iteration 30, at which point the solutions of H_{m0} and T_{m01} have converged.

Figure 3.17 compares the values of the slope measures $|\Delta H_{m0}^s|/H_{m0}^s$ and $|\Delta T_{m01}^s|/T_{m01}^s$ from (3.5) and (3.6) and the normalised curvature measure (3.9) at Station 8 of the Lake George simulation, during the iteration process. Also indicated on these figures are the default slope criteria for convergence ($\varepsilon_H^r = 0.02$ and $\varepsilon_T^r = 0.02$) and the criterion for the normalised curvature, here with the setting $\varepsilon_C = 2e\text{-}4$. At this geographic location, the slope measures $|\Delta H_{m0}^s|/H_{m0}^s$ and $|\Delta T_{m01}^s|/T_{m01}^s$ quickly fall below the criterion value of 2% (and likewise at 98% of the wet points in the domain), so that the criteria (3.5) and (3.6) terminate the simulation after 6 iterations. These plots also reveal that the range over which the slope measures vary is not large (less than an order of a magnitude)—if the criteria ε_H^r and ε_T^r were set to a much stricter value of 0.1%, say, the run would never terminate. By contrast, the curvature measure has a clear reducing trend during the iteration process, spanning a much larger range of values. With a maximum curvature value of $\varepsilon_C = 2e\text{-}4$, this is clearly the dominant criterion for convergence. After the 24th iteration the curvature measure remains below the given ε_C, meeting the convergence test at this location; at iteration 30 this was the case at 98% of all wet grid points, which terminated the iteration process.

Figures 3.18 and 3.19 show the results of spectra and integral parameters at the eight observation points in the Lake George field case under consideration. These figures show the significant difference between the results produced using the default and curvature-based criteria. The results achieved with the latter are similar to those obtained in the fully-converged results (compare with Figure 3.8), whereas, by comparison, those produced using the default criteria are distinctly lower in total variance. Figure 3.19 shows that the improvement of model convergence has translated to a better agreement between simulated and observed values of significant wave height. However, as noted in Section 3.4.1, comparison with the observations shows that this improved model result still suffers from a consistent overprediction of the spectral peak frequency (Figure 3.18).

To evaluate the generality of the findings above, Figure 3.20 considers the simulation results of the complete set of 14 cases, and compares the results obtained using the default convergence criteria with those using the curvature-based criteria, featuring two choices of ε_C. In each field situation, the results of the downwind-most observation station, which typically requires the most iterations for convergence, are presented. Figure 3.20 shows that the curvature criteria (3.5), (3.6) and (3.9) yield significant improvement in identifying the point of convergence compared to the default criteria, with results of H_{m0} and T_{m01} closer to the fully-converged values. By comparing the scatter in the two centre panels, it can also be seen that the values for T_{m01} tend to converge faster than H_{m0}, supporting the choice of the latter as a convergence measure. A normalised curvature criterion of $\varepsilon_C = 2e\text{-}4$ clearly ensures better convergence than the less stringent $\varepsilon_C = 1e\text{-}3$, but at the cost of having to use more iterations. The latter is an inevitable consequence of more stringent convergence criteria, since the underlying iteration behaviour has not been altered. The comparison in
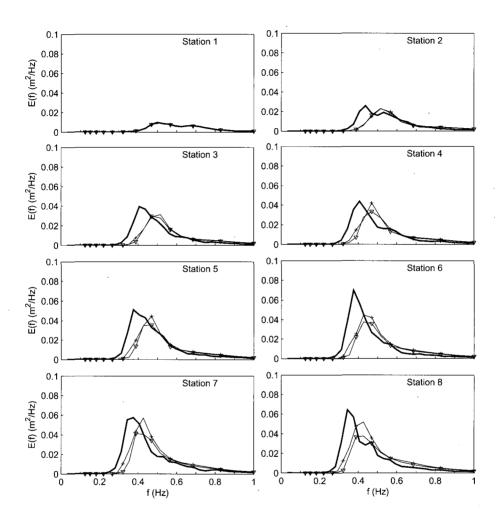
Figure 3.18: Lake George field experiment of near-idealised, depth-limited wave growth. Frequency spectra obtained with the default stopping criteria (3.5) and (3.6) with $\varepsilon_H^r = \varepsilon_T^r = 0.02$, $\varepsilon_H^a = 0.02$ m and $\varepsilon_T^a = 0.2$ s (6 iterations, triangles), with the criteria (3.5), (3.6) and (3.9) with $\varepsilon_C = 2e\text{-}4$ (30 iterations; plusses) and observations of Young and Verhagen (1996) (thick line).
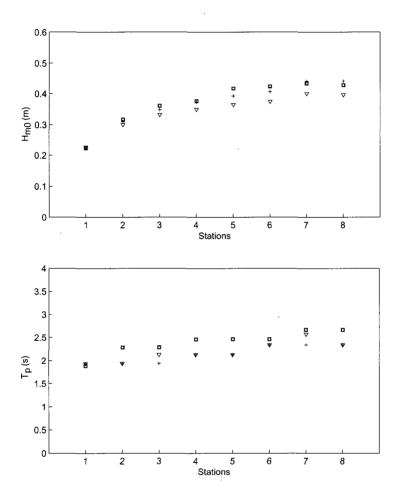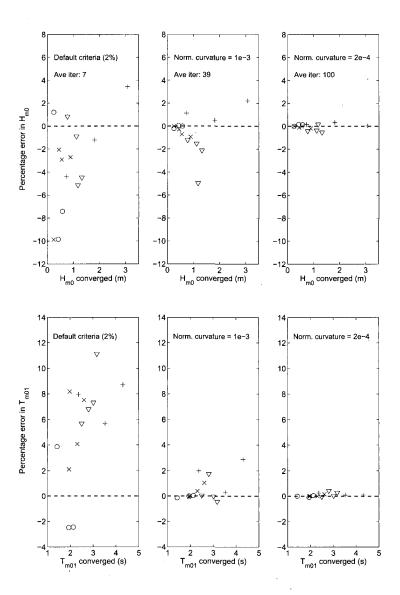
Figure 3.19: Lake George field experiment of near-idealised, depth-limited wave growth. Wave height and peak period obtained with the default stopping criteria (3.5) and (3.6) with $\varepsilon_H^r = \varepsilon_T^r = 0.02$, $\varepsilon_H^a = 0.02$ m and $\varepsilon_T^a = 0.2$ s (6 iterations, triangles), with the termination criteria (3.5), (3.6) and (3.9) with $\varepsilon_C = 2\text{e-}4$ (30 iterations, plusses) and observations of Young and Verhagen (1996) (squares).

Figure 3.20: Top panels: Percentage error in H_{m0} at output points incurred using three different stopping criteria, defined as $(H_{m0,stopped} - H_{m0,converged})/H_{m0,converged}$, plotted against $H_{m0,converged}$, for various test cases. Left-hand panel: default criteria, centre panel: new curvature criterion with $\varepsilon_C = $ 1e-3, right-hand panel: curvature criterion with $\varepsilon_C = $ 2e-4. The average number of iterations before run termination is indicated in each case. Bottom panels: Corresponding results for T_{m01}. In all panels the results plotted are of 14 individual cases, featuring: + deep water fetch-limited growth, $\bigcirc$ Lake George, $\times$ Norderneyer Seegat and $\triangledown$ Haringvliet.

Figure 3.20 suggests that a value of $\varepsilon_C = 1e\text{-}3$ for criterion (3.9) provides a good compromise between numerical accuracy and computational cost for the cases considered, yielding an average number of iterations between 30 and 50.

3.5 Conclusions

This chapter investigated the influence of two numerical aspects of stationary simulation in SWAN, namely convergence-enhancing measures and stopping criteria, on model accuracy. The impact of these numerical measures on model outcomes was investigated for idealised fetch- and depth-limited wave growth situations and for a selection of shallow water field cases.

A number of issues concerning the iteration behaviour and convergence of SWAN were addressed. It was shown that stable iteration behaviour can be obtained by means of nonstationary calculation using a very small time step. Since such an approach is time-consuming, in coastal application, iterative solution of the stationary form of the action balance equation is often applied, in which an infinitely large pseudo time step is involved. To ensure stable iteration whilst using a time step that is larger than that allowed by the physical processes modelled, convergence-enhancing measures are required. In the default model the technique of action limiting is used, and in this chapter the use of an alternative method, namely frequency-dependent under-relaxation, was investigated. From the investigation into these two convergence-enhancing measures, the following conclusions can be drawn:

(a) In deep water, the action limiter, as used in the default model, leads to relatively fast convergence and globally stable iteration behaviour. However, iteration curves of significant wave height and mean period display local maxima and minima, and feature small-amplitude oscillations.

(b) By using the technique of frequency-dependent under-relaxation, smoother iteration behaviour is achieved than with the action limiter, although more iterations are required to reach convergence. Because of this increased computational cost, the method of frequency-dependent under-relaxation is probably not well suited to operational application. Nonetheless, it can be considered to be an important numerical aid for scientific applications.

(c) Since frequency-dependent under-relaxation imposes no external limitation on wave growth, it can be considered to be a true numerical solution to the formulations of physics in SWAN. This was confirmed by the fact that the results of simulations in deep water and at intermediate depth using this method are in excellent agreement with those of nonstationary calculations using a very small time step and no limiter.

It is therefore a significant finding that the converged results produced by the action limiter differ very little from those of frequency-dependent under-relaxation, and also from those without any stabilizing measure, for a range of stationary cases. This would suggest that the limiter may not have a significant impact on stationary model solutions. This finding implies that, also from the point of view of accuracy, there is little to be gained in applying under-relaxation in practical applications.

(d) A significantly different situation is found in the surf zone, where the source terms of triad interaction and depth-induced breaking dominate quadruplet interaction, wind input and whitecapping. Here, as in deep water, the action limiter does not affect the converged solution, but it does slow down the iteration process considerably. Earlier reports that the limiter affects model outcomes (e.g. Haagsma and Otta 2001) can therefore only be ascribed to the non-convergence of the results considered by these authors. Since the use of the limiter does not affect model results in the surf zone, it can be left active along with the deep water terms, as has also been recommended by Bottema (2001a). We return to this issue in Chapter 5.

Proceeding from the choice that the action limiter is an acceptable method of enhancing model stability, it is required that reliable criteria be set for the termination of the iteration process. Such criteria should effectively locate the point of convergence, and neither terminate the iteration process prematurely nor continue it unnecessarily. Here the default, gradient-based criteria of SWAN were compared to proposed stricter stopping criteria based on the curvature of the series of successive iterates of the significant wave height. The following conclusions may be drawn from this investigation:

(e) The default stopping criteria tend to terminate the iteration process prematurely during periods of slow convergence or at local maxima or minima in the iteration curve. This was shown to lead to significant discrepancies between the results for wave height and mean period at run termination, and the actual values of these quantities produced at full convergence. Since these convergence criteria are based only on the absolute change and slope of the iteration curves, which go to zero at maxima and minima and which have relatively small dynamic ranges, using a smaller tolerance in gradient is not generally successful at improving these criteria.

(f) The curvature-based criterion has been shown to be significantly better at locating the point of convergence than the current default criteria, since it is not affected by local minima and maxima or slow convergence, and proves to have a far greater dynamic range of values. It has been shown that, with a sufficiently strict limiting value for normalised curvature, fully-converged model outcomes are obtained.

(g) Since the underlying iteration speed of the model has not been improved, the result that run termination has been postponed until a higher level of convergence has been reached implies that more iterations are required. It was shown that at present, a

compromise can be found between the number of iterations used and the accuracy achieved, leading to errors in H_{m0} and T_{m01} due to non-convergence of about $\pm 2\%$ when 30–50 iterations are used. However, there are also possibilities for the speeding up of the iteration process. The application of such measures are discussed in Chapter 7.

The investigation presented in this chapter has provided improved understanding of the impact of numerics, especially those involved in source term integration, on the performance of SWAN. This makes it possible to make a clearer distinction between inaccuracies due to numerics and those due to approximations in the formulations of physical processes. Examples of these are the remaining underprediction of peak wave period in the model results for Lake George (Figures 3.8 and 3.9), and the inaccurate prediction of the significant wave height in the laboratory case of Beji and Battjes (1993) (Figure 3.10). With the improved understanding of numerical influence, these discrepancies can, with greater certainty, be ascribed to shortcomings in the formulations of model physics. In Chapters 4 and 5 it is investigated whether the remaining inaccuracies in these—and other—cases can be reduced by addressing the expressions describing physical processes in deep water and in finite depth.

Chapter 4

Deep water source terms

4.1 Introduction

SWAN has been developed for the simulation of waves in coastal areas, featuring spatial scales ranging from shelf seas down to the scales of the surf zone. Considering that the domain boundary typically lies in deeper water, it is important that wind wave growth in deep water and at finite depth is accurately included in the model. Application of SWAN to field situations in coastal regions has shown that the significant wave height tends to be well predicted, but that period measures are typically somewhat underestimated (refer Chapter 3, also Ris *et al.* 1999; Bottema *et al.* 2003; Rogers *et al.* 2003). The underprediction of period measures is related to the following: For pure wind-sea, the energy density at lower frequencies is typically underpredicted, whereas energy levels in the tail are generally overpredicted. This leaves both the peak and mean periods underpredicted. Moreover, in combined swell–sea situations, SWAN predicts higher dissipation of swell in the presence of wind-sea than without it, whereas the wind-sea part of the spectrum experiences reduced dissipation in the model due to the presence of the swell, leading to accelerated wave growth (Hurdle, 1998; Holthuijsen and Booij, 2000). This behaviour is at odds with observations in the field and the laboratory, for example Donelan (1987), which suggests that the presence of low-frequency waves may actually reduce the growth of the wind-sea part of the spectrum, while the swell energy is not dissipated.

The dominant source terms in deep water and finite depths are wind input, whitecapping dissipation and quadruplet nonlinear interaction. This chapter investigates to what extent the formulations for these deep water source terms used in SWAN contribute to the inaccuracies described above, and proposes alternatives by which model performance can be improved. In default mode, SWAN uses the wind input and whitecapping expressions of Komen *et al.* (1984), with wind input based on Snyder *et al.* (1981) and whitecapping based on Hasselmann (1974), together with the Discrete Interaction Approximation

(DIA) for quadruplet interaction (Hasselmann and Hasselmann 1985). Of these three, the wind input based on Snyder *et al.* (1981) is the best-established experimentally, at least for light winds over fairly mature wind-sea. Quadruplet interaction, although difficult to measure experimentally, is well-established theoretically for homogeneous, random-phase wave fields. However, because of the high computational cost of calculating all possible interactions, SWAN employs the DIA approximation, which only includes a small subset of these interactions.

Studies by Van Vledder *et al.* (2000), Gorman *et al.* (2000) and Van Vledder and Bottema (2003) suggest that some of the inaccuracy described above may be due to the use of the DIA for the computation of quadruplet interaction. Comparison between the source term results of the DIA and those of algorithms in which all possible interactions are calculated (the so-called exact methods) show an incorrect position and width (in frequency space) of the DIA's low-frequency positive interaction lobe and an overestimation of its directional width. In water of finite depth, Van Vledder and Bottema (2003) and Tsagareli *et al.* (2006) show that discrepancies between the results of exact methods and those of the DIA—combined with a depth scaling of Herterich and Hasselmann (1980)—are even more pronounced. Due to the finite water depth, the low-frequency positive interaction lobe computed by exact methods increases in magnitude and shifts toward lower frequencies. The depth scaling of Herterich and Hasselmann (1980) takes the former of these effects into account, but not the latter, potentially contributing towards period underprediction. Therefore, the first topic of this chapter is a comparison between the performance of SWAN when using the DIA (the default model) and the performance when an exact method is used for computing quadruplet interaction. Here the WRT exact method, implemented by Van Vledder (2005b), is used. It will be shown that some improvement is found in the prediction of the peak frequency, but that energy levels in the spectral tail remain overpredicted.

In comparison to wind input and quadruplet interaction, there is much uncertainty concerning the physical mechanism of whitecapping in deep and shallow water, and hence the appropriate form for its source term. The expressions available for whitecapping are therefore mostly speculative. The whitecapping formulation of Komen *et al.* (1984) has been associated with many of the model errors described above: it has been found that the erroneous model behaviour in the presence of swell is caused by the expression's dependence on the mean spectral wavenumber and steepness (Hurdle 1998), and that the overprediction of energy levels in the tail appears to be caused by insufficient dissipation in this spectral region (Rogers *et al.* 2003). The main focus of this chapter is therefore the improvement of the modelling of whitecapping dissipation in SWAN.

A number of modifications to the whitecapping expression have been proposed in the literature to improve the simulation results of SWAN (all in combination with the DIA). A first group of modifications considers pure wind-sea conditions: Booij *et al.* (1999) apply a rescaled version of the Komen *et al.* (1984) whitecapping formulation in combination

with the wind input expression of Janssen (1991) (the so-called WAM Cycle 4 physics, see Komen *et al.* (1994)). They find, however, that this source term combination produces less accurate predictions of significant wave height and peak period than the default model. This implementation was revised by Lalbeharry *et al.* (2004), who show, for pure wind sea, improvement over the default model in terms of period prediction. Rogers *et al.* (2003) alter the weighting of the relative wavenumber factor in the Komen *et al.* (1984) whitecapping formulation, by which the distribution of dissipation over frequency is changed. This is considered to compensate for underprediction of the peak period caused by the use of the DIA, in addition to increasing dissipation in the tail region. This leads to improved period measures, but unfortunately wave energy is overestimated as a result (Figure 4.1).

The second group of modifications considers combined swell–sea situations. Holthuijsen and Booij (2000) suggest that the dependence of wind-sea dissipation on swell in the Komen *et al.* (1984) expression be removed by making the dissipation at a particular frequency a function of the mean wavenumber and steepness of only the frequencies higher than itself. This method succeeds in removing the dependence of wind-sea dissipation on swell, but does not appear to be based on any physical considerations. Furthermore, this method retains the problem of enhanced dissipation of swell in the presence of wind-sea. Hurdle and Van Vledder (2004) propose an opposite approach (the so-called Cumulative Steepness Method, CSM), where dissipation at a particular frequency depends on the cumulative steepness of all spectral components *up to* the frequency considered, rather than on the mean values of wavenumber and steepness taken over the entire spectrum. This approach is based on the principle of surface straining, by which shorter waves are steepened by their superposition on longer waves, thus inducing breaking. Hurdle and Van Vledder demonstrate that their dissipation source term successfully decouples the growth of wind-sea from the presence of low-energy swell, but their model variant does not reproduce the fetch-limited growth curve in energy for pure wind sea at all (Figure 4.1). Rogers *et al.* (2003) propose to disallow the dissipation of swell energy, so that the dissipation of swell in combined swell–sea conditions is prevented. The spurious influence of swell on wind-sea, however, is not addressed. Bidlot *et al.* (2005) proposed to redefine the mean spectral wavenumber used in the Komen *et al.* (1984) whitecapping expression such that more weight is given to the higher wavenumbers. Ardhuin *et al.* (2007) show that this altered parameterisation of the wavenumber reduces, but does not eliminate the spurious effect of swell on wind sea generation. This result strengthens the case against the use of spectral mean variables in whitecapping expressions.

Many alternative dissipation formulations exist besides those implemented in SWAN which were reviewed above. Donelan and Yuan (1994) distinguish between the following classes of models for dissipation due to wave breaking: whitecap models (e.g. Hasselmann (1974) in SWAN), probability models (e.g. Longuet-Higgins, 1969b) and quasi-saturated models (e.g. Phillips, 1985). Recently, a line of investigation that relates breaking probability to local spectral steepness was initiated, prompted by the apparent link between deep water wave breaking and wave groups observed by Donelan *et al.* (1972) and Holthuijsen and
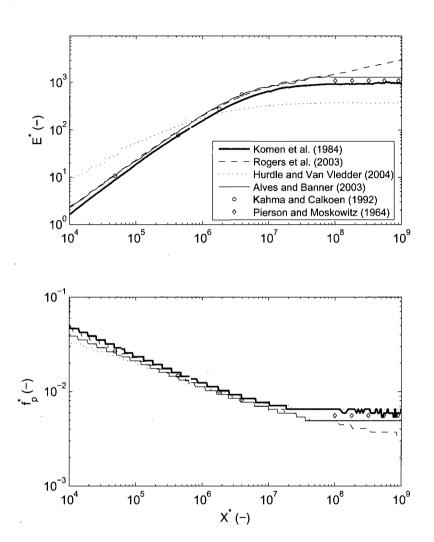
Figure 4.1: Comparison of the deep water, fetch-limited growth curves produced using Komen *et al.* (1984) source terms (default model) with those produced using the Rogers *et al.* (2003), Hurdle and Van Vledder (2004) and Alves and Banner (2003) alternatives for whitecapping. In all cases the DIA is used for quadruplet interaction. Results for $U_{10} = 10$ m/s, presented in terms of dimensionless energy $E^* = g^2 E_{tot}/u_*^4$ and peak frequency $f_p^* = f_p u_*/g$ as functions of dimensionless fetch $X^* = gX/u_*^2$, with friction velocity u_* calculated using Wu (1982).

Herbers (1986), amongst others. Assuming that dissipation occurs at the peaks of wave groups, Banner *et al.* (2000) demonstrated that the mean steepness of dominant waves (integrated over a bandwidth around the spectral peak) is well-correlated with their breaking probability, prompting them to propose this quantity as the primary variable determining the breaking of dominant waves. It was also found that there is a dominant wave steepness below which no breaking was observed: the so-called breaking threshold. Banner *et al.* (2002) extend the study of Banner *et al.* (2000) to investigate the breaking probability over spectral intervals up to 2.48 times the spectral peak frequency. In their study, the mean steepness parameter used by Banner *et al.* (2000) is replaced by the spectral saturation as a convenient, bandwidth-independent measure of the local spectral steepness. Banner *et al.* (2002) demonstrate a relation between the saturation spectrum and breaking probability across the spectrum from the peak frequency f_p to $2.48 f_p$, and found that, also in this spectral region, breaking only commences once a saturation threshold has been reached. Alves and Banner (2003) incorporate these findings into a dissipation formulation, proposing an expression that features a primary dependence on the (frequency-local) spectral saturation. We note, however, that there are doubts as to whether their proposed dissipation expression can still be directly related to wave groups (Babanin and Van der Westhuysen 2007). Figure 4.1 shows the growth curve produced with the whitecapping expression of Alves and Banner (2003) implemented in SWAN, using their calibration BYM1 (applied here in combination with the DIA). The model results fit the observations well, and corrects the frequency overprediction of the default model.

A central question regarding expressions for dissipation due to breaking is whether the dissipation is local or broad-banded in frequency space. From experimental data, Phillips *et al.* (2001) and Melville and Matusov (2002) find that the dissipation is local in frequency space, whereas Banner *et al.* (1989), Meza *et al.* (2000) and, recently, Young and Babanin (2006) present evidence that, in addition to dissipating energy locally, breaking longer waves dissipate energy of shorter waves too. Although breaking is considered to be the main mechanism of wave energy dissipation, additional dissipation is possible due to, for example, the interaction of waves with turbulence (e.g. Tolman and Chalikov 1996; Ardhuin and Jenkins 2006) and interactions between long and short waves (Longuet-Higgins 1969a; Hasselmann 1971). Independent formulations for such mechanisms do exist, but they still require much development.

In this study, a new set of deep water source terms, featuring a wave breaking expression based on that of Alves and Banner (2003), is developed and implemented in SWAN to address the inaccuracies concerning period measures reviewed in the opening paragraph. The saturation-based expression of Alves and Banner (2003) regards dissipation as essentially local in wavenumber space, and consequently offers a way to resolve the spurious behaviour of SWAN under combined swell–sea conditions. In the present study, the proposed dissipation expression is used together with a wind input term based on that of Yan (1987), which is a combination of Plant (1982)'s expression for strongly forced waves with that of Snyder *et al.* (1981) for weakly forced waves. Based on the scaling arguments of Phillips (1985)

and Resio *et al.* (2004), the choice of parameters for the dissipation term is made in such a way that it has the same frequency scaling as the wind input term. This yields a whitecapping source term that has a secondary dependence on wave age. The resulting source term combination is calibrated against fetch- and depth-limited growth curves and subsequently evaluated for two field cases featuring combined swell–sea wave conditions and a number of finite depth field cases, where it will be shown to yield satisfactory results.

The structure of this chapter is as follows: Firstly, the default deep water source terms are presented in Section 4.2, after which the performance of the default wind and whitecapping expressions in combination with the WRT exact method for quadruplet interaction is investigated (Section 4.3). Secondly, the new saturation-based source term combination is presented in Section 4.4, followed by a calibration and evaluation of the new model for a number of idealised and field cases (Section 4.5). This evaluation is done predominantly using the DIA, but the performance of the saturation-based model is also checked for use in combination with exact quadruplet calculation. Section 5.5 closes this chapter with a discussion and conclusions. Parts of this chapter have been published in somewhat different form in Van der Westhuysen *et al.* (2005), Van der Westhuysen *et al.* (2007), Mulligan *et al.* (2007) and Babanin and Van der Westhuysen (2007).

4.2   Default deep water source terms

In this section, the default expressions for the deep water source terms of wind input, whitecapping and quadruplet interaction are presented. The expressions for wind input and whitecapping shown here are applied in Section 4.3, where the impact of using alternative methods of computing quadruplet interaction is investigated. In Section 4.5 below, these expressions are contrasted against a newly proposed source term combination based on the whitecapping expression of Alves and Banner (2003).

4.2.1   Whitecapping dissipation

Whitecapping dissipation is currently represented in SWAN by the pulse-based, quasi-linear model of Hasselmann (1974). The formulation used in the model is that of Komen *et al.* (1984):

$$S_{wc,Komen}(\sigma,\theta) = -C_{ds}\left(\frac{k}{\tilde{k}}\right)^{q}\left(\frac{\tilde{s}}{\tilde{s}_{PM}}\right)^{r}\tilde{\sigma}\,E(\sigma,\theta) \tag{4.1}$$

in which k is the wavenumber, with a spectral mean $\tilde{k}$, and $\tilde{\sigma}$ is the spectral mean radian frequency. These mean quantities are defined respectively as $\tilde{k} = \left[E_{tot}/\iint k^{-1/2}E(\sigma,\theta)\,d\sigma d\theta\right]^{2}$

and $\tilde{\sigma} = E_{tot} / \iint \sigma^{-1} E(\sigma, \theta) \, d\sigma d\theta$, where E_{tot} is the total spectral variance. Quantity $\tilde{s}$ is the mean spectral steepness, defined as $\tilde{k}\sqrt{E_{tot}}$, and $\tilde{s}_{PM}$ is the mean steepness of the Pierson-Moskowitz spectrum. The tuning parameters of this expression are C_{ds}, q and r. The default setting is $C_{ds} = 2.36 \times 10^{-5}$, $q = 1$ and $r = 4$. Note the strong dependence of this expression on the mean spectral steepness $\tilde{s}$ and spectral mean wavenumber $\tilde{k}$.

4.2.2 Wind input

The current default expression for exponential wave growth due to wind is the formulation of Komen *et al.* (1984), which is based on the empirical results of Snyder *et al.* (1981):

$$\beta_{Snyder}(\sigma, \theta) = \frac{1}{\sigma E} S_{in}(\sigma, \theta) = \max\left[0 \, , \, 0.25\frac{\rho_a}{\rho_w}\left(28\frac{u_*}{c}\cos(\theta - \alpha) - 1\right)\right] \qquad (4.2)$$

where ρ_a and ρ_w are the densities of air and water respectively, u_* is the friction velocity of the wind, c the wave phase velocity and α the wind direction. Expression (4.2) is based on field measurements of weakly forced waves $(1 < U_5/c < 3)$ where U_5, the wind speed at 5 m height, had rather low values of 5–7 m/s. Hasselmann and Bösenberg (1991) extended this study for conditions more typical of those in the open ocean, with wind speeds in the range $U_5 = 2$–12 m/s. Their data, which had a comparable wind forcing range of $1 < U_5/c < 2.5$, yielded a wind input expression similar to (4.2). Therefore, (4.2) seems to be well-established for weakly forced conditions, but its proven validity does not extend to the strongly forced conditions of young wave fields. We return to this issue in Section 4.4 below.

4.2.3 Quadruplet interaction

Nonlinear energy transfer due to resonant third-order wave–wave interactions is described mathematically by the Boltzmann integral for surface gravity waves, proposed by Hasselmann (1962). A set of four waves (a quadruplet) exchanges energy through resonant interaction when the following conditions are met:

$$\vec{k}_1 + \vec{k}_2 = \vec{k}_3 + \vec{k}_4 \qquad (4.3)$$

$$\sigma_1 + \sigma_2 = \sigma_3 + \sigma_4 \qquad (4.4)$$

where $\vec{k}_{1..4}$ are the wavenumbers and $\sigma_{1..4}$ the radian frequencies of the four interacting waves, which are in turn related by the linear dispersion relation $\sigma^2 = gk \tanh(kd)$, at a

given water depth d. The rate of change of action density at a wavenumber $\vec{k}_1$ due to all quadruplet interactions involving $\vec{k}_1$ is given by Hasselmann (1962) as

$$\begin{aligned}
S_{nl4}(\vec{k}_1) &= \iiint G(\vec{k}_1, \vec{k}_2, \vec{k}_3, \vec{k}_4)\delta(\vec{k}_1 + \vec{k}_2 - \vec{k}_3 - \vec{k}_4)\delta(\sigma_1 + \sigma_2 - \sigma_3 - \sigma_4) \\
&\quad \times [N_1 N_2(N_3 + N_4) - (N_1 + N_2)N_3 N_4]\, d\vec{k}_2\, d\vec{k}_3\, d\vec{k}_4
\end{aligned} \tag{4.5}$$

in which $N_i = N(\vec{k}_i)$ is the action density at the wavenumber $\vec{k}_i$, G is a coupling coefficient and δ is the Dirac delta function.

Various numerical integration algorithms for the Boltzmann integral (4.5) exist. These can be divided into methods aiming at efficiently solving the complete integral (so-called exact methods) and methods that approximate or parameterize the integral in some way, for the sake of computational efficiency. In this study the exact computation method developed by Webb (1978a), Tracy and Resio (1982) and Resio *et al.* (2001)—referred to as the WRT method—is applied. This algorithm was optimised and reprogrammed by Van Vledder (2005b), and is used in this form in the present study.

The most widely-used approximation of (4.5) is the Discrete Interaction Approximation (DIA) (Hasselmann *et al.* 1985), in which only a single interaction quadruplet and its mirror image are used to estimate the energy transfer. In this approach, the wave numbers $\vec{k}_1$ and $\vec{k}_2$ are taken equal and those of the remaining two components are specified by a parameter λ such that

$$\begin{aligned}
\sigma_1 &= \sigma_2 = \sigma \\
\sigma_3 &= (1 + \lambda)\sigma = \sigma^+ \\
\sigma_4 &= (1 - \lambda)\sigma = \sigma^-
\end{aligned} \tag{4.6}$$

Hasselmann *et al.* (1985) propose a value $\lambda = 0.25$. The DIA source term used in SWAN reads

$$\begin{pmatrix} \delta S_{nl} \\ \delta S_{nl}^+ \\ \delta S_{nl}^- \end{pmatrix} = \begin{pmatrix} -2 \\ 1 \\ 1 \end{pmatrix} C_{nl4}\, g^{-4}\left(\frac{\sigma}{2\pi}\right)^{11} \left(E^2 \left(\frac{E^+}{(1 + \lambda)^4} + \frac{E^-}{(1 - \lambda)^4} \right) - 2E\frac{E^+ E^-}{(1 - \lambda^2)^4} \right) \tag{4.7}$$

where C_{nl4} is a proportionality coefficient and E, E^+ and E^- are the energy densities at the wavenumbers $\vec{k}_1 = \vec{k}_2$, $\vec{k}_3$ and $\vec{k}_4$. δS_{nl}, δS_{nl}^+ and δS_{nl}^- are the corresponding nonlinear energy transfers to these wavenumbers.

4.3 Simulations with exact quadruplet interaction

As discussed in the introduction to this chapter, a number of studies have highlighted inaccuracies in the results of the DIA (4.7) when compared to computationally intensive exact methods of solving (4.5). Since these inaccuracies could account for some of the unsatisfactory model performance outlined above, this section investigates the effect on model performance of replacing the DIA by an exact expression for quadruplet interaction.

Figure 4.2 shows deep water fetch-limited growth curves produced by the wind input and whitecapping expressions (4.1) and (4.2), in combination with the DIA and WRT methods for computing quadruplet interaction. These curves were obtained using a series of nested one-dimensional simulations, with a geographical discretisation ranging from 1 m (at short fetches) to 10 km (at long fetches) and frequency and directional resolutions of $\Delta f/f = 0.1$ and $\Delta\theta = 10^o$ respectively. Here $E^* = g^2 E_{tot}/u_*^4$ and $f_p^* = u_* f_p/g$ are the dimensionless energy and peak frequency respectively and $X^* = gX/u_*^2$ the dimensionless fetch. No recalibration of the whitecapping term was done for the model variant using the WRT method. The top panels of Figure 4.2 show that both model variants reproduce dimensionless energy and peak frequencies adequately over a wide fetch range, including the observations of Kahma and Calkoen (1992) (composite dataset) and Pierson and Moskowitz (1964). However, closer inspection of the Kahma and Calkoen fetch range (bottom panels) reveals that using the WRT exact method yields somewhat smaller biases in dimensionless peak frequency with respect to the observations, than when the DIA is used. (The sawtooth shape of the bias curves of peak frequency is due to the discrete nature of the frequency domain in the model; it is the mean of these oscillations that is compared to the observations.) Furthermore, both model variants tend to underpredict the total energy somewhat—something which could reasonably be corrected by means of recalibration of the proportionality coefficient C_{ds}.

Figure 4.3 shows the corresponding directionally-integrated spectra produced using the DIA and WRT methods respectively. These results are compared to the parametric spectral form of Donelan et al. (1985), parameterised with the peak frequency and total energy of Kahma and Calkoen (1992). The results shown are for a dimensionless fetch of $X^* = 6 \times 10^5$, which lies within the Kahma and Calkoen fetch range. As shown above, the model variant using the DIA produces some overestimation of the peak frequency, and also yields a somewhat broader distribution around the spectral peak. These two characteristics are better reproduced when using the WRT exact method. On the low-frequency flank of the spectrum, both the DIA and WRT results are lower than observed values—in the case of the DIA simulation because the general position of the spectral peak is inaccurate, and with the WRT simulation because the quadruplet interactions produce a low-frequency flank that appears to be too steep. With regard to the energy-containing tail region $(1.5 < f/f_p < 3)$, the model variant using the DIA yields an overestimation of energy, which is only slightly corrected in the WRT simulation. Characteristic differences between the results produced using the DIA and the WRT method are also found in their respective
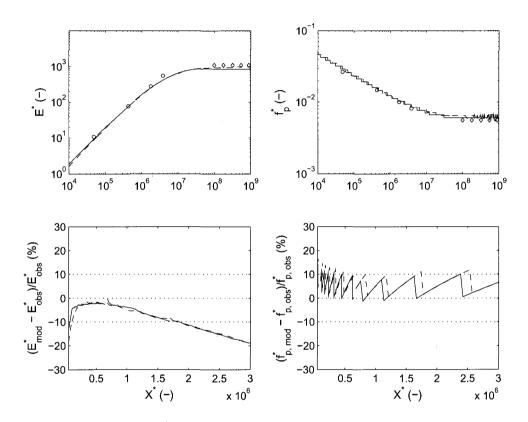
Figure 4.2: Deep water, fetch-limited growth curves produced using the default Komen *et al.* (1984) formulations for wind and whitecapping combined with respectively the DIA (dashed lines) and WRT (solid lines) quadruplet interaction expressions. Top panels: comparison with fetch-limited relations of Kahma and Calkoen (1992) (circles) and Pierson and Moskowitz (1964) (diamonds). Bottom panels: bias of model results with respect to Kahma and Calkoen (1992) data. Results for $U_{10} = 10$ m/s.
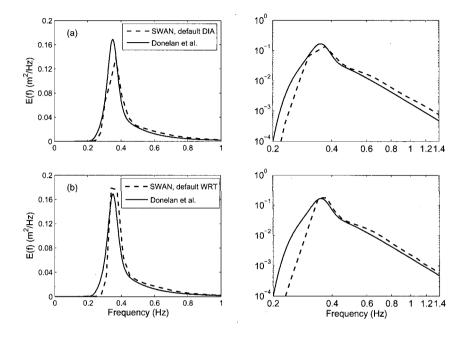
Figure 4.3: Comparison between the deep water, fetch-limited spectra produced using the default Komen *et al.* (1984) wind and whitecapping expressions and the DIA (row (a)) and the WRT exact method (row (b)) and the parametric form of Donelan *et al.* (1985) with the peak frequency and total energy according to Kahma and Calkoen (1992). Results for $U_{10} = 10$ m/s.

directional distributions. Figure 4.4 (row (b)) shows that the model using the WRT method produces significantly narrower directional distributions than the DIA variant. Also, the distributions produced with the WRT method become bi-modal at higher frequencies, as observed in the field by Hwang *et al.* (2000), whereas those produced with the DIA remain unimodal. This transition to bi-modality is also found with the WAM model when using exact quadruplet interactions (Banner and Young 1994).

Concerning simulation in depth-limited conditions, the performance of SWAN using the DIA and the WRT was investigated for the same field case at Lake George, Australia, that was considered in Chapter 3. This field case, taken from the Young and Verhagen (1996b) data set, features a wind speed of 10.8 m/s and an average water depth of about 2 m. Wave spectra were measured along an array of eight stations, the downwind-most of which (Station 8) having a fetch of 16 km. The model setup and discretizations are the same as
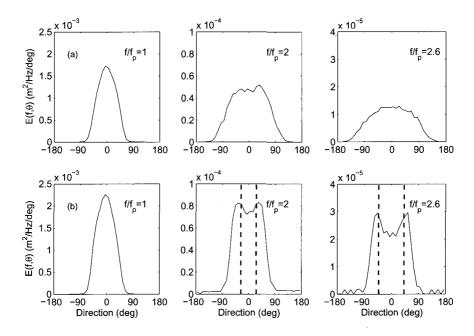
Figure 4.4: Simulated directional distributions at the peak and energy-containing tail produced using the DIA (row (a)) and the WRT method (row (b)) at three different frequencies. Results for deep-water, fetch-limited growth with $U_{10} = 10$ m/s at $X^* = 6 \times 10^5$. The dashed lines in row (b) are the locations of the bi-modal peaks observed by Hwang *et al.* (2000).

those used in Chapter 3. Figure 4.5 compares the results of directionally-integrated spectra at the downwind-most four stations, simulated using the DIA and the WRT respectively. The model variant using the DIA consistently overestimates the spectral peak frequency. Concerning the spectral tail region of $f/f_p > 1.5$, the observed spectra display a power law decay of about f^{-4}. This power law trend is reproduced well using the DIA, but the overall energy levels in this spectral region are overpredicted. Using the WRT exact method yields lower estimates of the spectral peak frequency than with the DIA, bringing these results in closer agreement with the observations, although still not matching them. This result is in keeping with the findings of Van Vledder and Bottema (2003) stating that, under the influence of finite depth, the low-frequency positive interaction lobe produced by exact calculations is shifted towards lower frequencies than is the case with the DIA. As was seen above for deep water conditions, the WRT exact method produces a narrower distribution of energy around the peak frequency than the DIA. This results in simulated spectra that are generally somewhat more peaked than the observed spectra. In the spectral tail region,
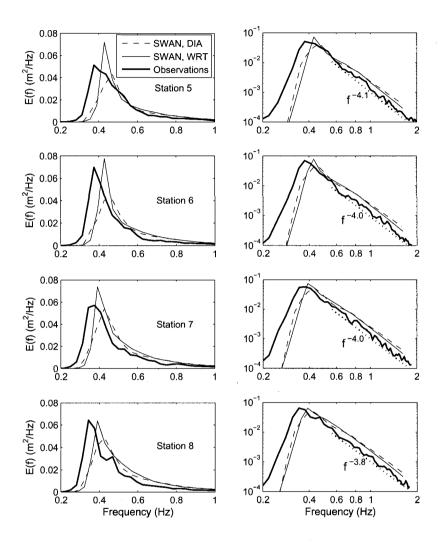
Figure 4.5: Simulations of depth-limited wave growth in Lake George, Australia. Spectra produced using the default Komen *et al.* (1984) formulations for wind and whitecapping combined with respectively the DIA (dashed lines) and WRT (solid lines) quadruplet interaction expressions. Spectra on the left are repeated on the right on logarithmic axes. Observations are of Young and Verhagen (1996), with the dotted lines indicating the power law slopes of the observed spectral tails. Average wind speed is 10.8 m/s.

energy levels produced using the WRT are only slightly lower than those produced by the DIA, and they are still higher than the energy levels in the observations.

From the results above it can be concluded that using a detailed, but computationally intensive method for computing (4.5), such as the WRT, yields some improvement in model accuracy compared to using the DIA approximation. Yet discrepancies still remain between simulated and observed peak frequencies, and energy levels in the spectral tail remain overpredicted. Furthermore, it is clear that using a more detailed computation of quadruplet interactions does not address the spurious model behaviour observed in the case of combined swell and wind sea conditions. Below, an alternative formulation for whitecapping dissipation is investigated to address these remaining inaccuracies.

4.4   Saturation-based model

In this section a new source term combination is presented that features nonlinear saturation-based whitecapping dissipation. This whitecapping expression is combined with an alternative wind input formulation, and scaling laws are applied to achieve the desired model behaviour in deep and finite depth water.

4.4.1   Whitecapping dissipation

The whitecapping formulation investigated in this study is based on that of Alves and Banner (2003), which has a primary dependence on the azimuthal-integrated spectral saturation $B(k)$:

$$S_{wc,AB}(k,\theta) = -C'_{ds} \left[\frac{B(k)}{B_r} \right]^{p/2} \underbrace{(E_{tot}k_p^2)^m}_{A} \underbrace{\left(\frac{k}{\tilde{k}} \right)^n}_{B} \sigma\, \Phi(k,\theta) \tag{4.8}$$

where $\Phi(k,\theta)$ is the polar wavenumber spectrum (which is defined such that $E_{tot} = \int_0^{2\pi} \int_0^\infty \Phi(k,\theta)k\,dk\,d\theta$), B_r a threshold saturation level, $E_{tot}k_p^2$ an integral steepness parameter and C'_{ds}, m and n tunable parameters. The azimuthal-integrated spectral saturation $B(k)$, which is closely related to spectral steepness, is given by Banner *et al.* (2002) as

$$B(k) = \int_0^{2\pi} k^4 \Phi(k,\theta)\,d\theta \ . \tag{4.9}$$

When $B(k) > B_r$, waves break, and the exponent p is set equal to a constant calibration parameter p_0. For $B(k) < B_r$ there is no breaking, and the dissipation based on $B(k)$ gives

way to other sources of dissipation (see below) by setting p to zero. A smooth function is used by Alves and Banner to make the transition between these two extremes:

$$p = \frac{p_0}{2} + \frac{p_0}{2} \tanh \left\langle 10 \left(\left[\frac{B(k)}{B_r} \right]^{1/2} - 1 \right) \right\rangle. \tag{4.10}$$

By means of numerical simulation and comparison against spectral and integral observations, Alves and Banner (2003) propose using values of B_r in the range 3.10×10^{-3} to 4.25×10^{-3} and $p_0 = 4$ to 8. These values of B_r are about double the (non-normalised) threshold saturation values found by Banner *et al.* (2002), so that they cannot be ascribed the meaning of a saturation threshold. Furthermore, the high values of p_0 imply a dependence of dissipation on the variance density of up to a power of 5. As discussed in Babanin and Van der Westhuysen (2007), it is unclear how such high rates of dissipation can be balanced by conventional wind input expressions such as those of Snyder *et al.* (1981), Plant (1982) or Janssen (1991). As an example, Figure 4.6 presents the frequency spectra produced by Alves and Banner's calibration BYM1, which corresponds to the growth curve results shown in Figure 4.1 above. Figure 4.6 also includes the level of the saturation threshold (in this case $B_r = 4.25 \times 10^{-3}$). It is seen that over most of the fetch, the spectrum has been dissipated down to the level of the threshold, so that the saturation-based component does not play an active role in the dissipation process anymore ($B(k) \approx B_r$). In the present study, these shortcomings are addressed by *a priori* limiting the value of B_r to the range 1.5–2.0×10^{-3} in accordance with Banner *et al.* (2002), and by choosing p_0 such that a balance is maintained between the source terms of wind input, dissipation and quadruplet interaction.

A third perceived shortcoming of (4.8) is that the primary dissipation mechanism based on $B(k)$ is supplemented with two multiplication factors in order to represent dissipation due to general background turbulence (factor A) and long-wave-short-wave interactions (factor B). These were included by Alves and Banner to obtain greater tunability over a wide range of wave ages. However, as discussed in the introduction, these factors re-introduce mean spectral dependencies to the expression. Moreover, being multiplication factors rather than separate terms in a sum, they also oversimplify the influence that turbulence and longer waves may have on the wave field, so that they cannot be expected to perform well in the representation of these processes. We have therefore chosen to separate the dissipation modes of breaking and non-breaking waves, so that they are active over different parts of the spectrum:

$$S_{wc,SB}(\sigma, \theta) = f_{br}(\sigma) S_{dis,break} + [1 - f_{br}(\sigma)] S_{dis,non-break} \tag{4.11}$$

where $S_{dis,break}$ is the dissipation contribution by breaking waves and $S_{dis,non-break}$ dissipation by means other than breaking (e.g. turbulence). The changeover between the
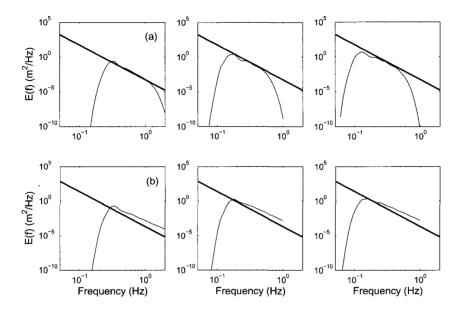
Figure 4.6: Comparison between frequency spectra produced during deep water fetch-limited wave growth and the level of the saturation threshold. Row (a): Spectra produced using Alves and Banner (2003) with the calibration BYM1, featuring a threshold level of $B_r = 4.25 \times 10^{-3}$, in combination with the DIA. Row (b): Corresponding results for the saturation-based model (4.11) and (4.15) with threshold level of $B_r = 1.75 \times 10^{-3}$. Results for $X^* = 7 \times 10^4$ (left), $X^* = 7 \times 10^5$ (centre) and $X^* = 1 \times 10^7$ (right), with $U_{10} = 10$ m/s.

dissipation of breaking waves and that of non-breaking waves is made with a smooth transition function f_{br} similar to (4.10):

$$f_{br}(\sigma) = \frac{1}{2} + \frac{1}{2} \tanh \left\langle 10 \left(\left[\frac{B(k)}{B_r} \right]^{1/2} - 1 \right) \right\rangle. \tag{4.12}$$

Expression (4.8) forms the basis for the dissipation contribution by wave breaking, $S_{dis,break}$. The influence of the multiplication factors A and B is removed by setting the exponents m and n equal to zero, reducing (4.8) to its dependence on frequency-local wave breaking only. Omitting A and B, and transforming (4.8) into frequency space (but retaining $B(k)$ and B_r in wavenumber space and replacing σ by $g^{\frac{1}{2}} k^{\frac{1}{2}}$) leads to the dissipation expression

$$S_{dis,break}(\sigma, \theta) = -C'_{ds} \left[\frac{B(k)}{B_r} \right]^{p/2} g^{\frac{1}{2}} k^{\frac{1}{2}} E(\sigma, \theta) \tag{4.13}$$

where $B(k)$ is calculated from frequency space variables as follows

$$B(k) = \int_0^{2\pi} \frac{d\sigma}{dk} k^3 E(\sigma, \theta) \, d\theta \ = c_g k^3 E(\sigma). \tag{4.14}$$

As mentioned above, the choice of the exponent p is made by taking into consideration the balance between the deep water source terms, as will be described in Section 4.4.3 below. This leaves C'_{ds} and B_r as the only remaining tuning parameters of (4.13).

4.4.2 Wind input

Since the present study is mainly concerned with the effects of altering the quadruplet interaction and whitecapping formulations in SWAN, we restrict the scope here to established empirical expressions for wind input. For strongly forced waves ($u_*/c > 0.1$) a wide variety of laboratory results (e.g. Plant 1982; Peirson and Belcher 2005) and some field observations (e.g. Hsiao and Shemdin 1983) point to a quadratic dependence of the wind-induced energy input on the wind forcing parameter u_*/c. Under weaker wind forcing ($u_*/c < 0.1$) a linear dependence on u_*/c, as used in (4.2), seems to hold (Snyder $et\ al.$ 1981; Hasselmann and Bösenberg 1991). Expressions such as that of Hsiao and Shemdin (1983) and Yan (1987) unify these two observational ranges. Yan (1987) proposes an analytical fit through the experimental datasets of Snyder $et\ al.$ (1981) and Plant (1982) of the form

$$\beta_{fit} = D \left(\frac{u_*}{c} \right)^2 \cos(\theta - \alpha) + E \left(\frac{u_*}{c} \right) \cos(\theta - \alpha) + F \cos(\theta - \alpha) + H \tag{4.15}$$

where D, E, F and H are coefficients of the fit. Yan proposes the parameter values $D = 4.0 \times 10^{-2}$, $E = 5.44 \times 10^{-3}$, $F = 5.5 \times 10^{-5}$ and $H = -3.11 \times 10^{-4}$, which produces a reasonable fit between the curves of Snyder $et\ al.$ and Plant. However, Yan's fit yields a smaller growth rate than the Snyder $et\ al.$ (1981) expression for mature waves (for u_*/c lower than 0.054). Yan (1987) confirms that this leads to an underestimation of the evolution of mature waves compared to that produced using Snyder $et\ al.$'s expression. We have therefore refitted (4.15) to better match Snyder $et\ al.$'s expression for mature waves. This yielded parameter values of $D = 4.0 \times 10^{-2}$, $E = 5.52 \times 10^{-3}$, $F = 5.2 \times 10^{-5}$ and $H = -3.02 \times 10^{-4}$. It is this refitted expression that is used throughout the present study.

4.4.3   Parameter choice for saturation-based model

In choosing the parameter p in the wave breaking dissipation term (4.13), which affects the expression's frequency scaling, it was aimed to arrive at a spectral shape that corresponds with observations in the field. A robust feature of observed spectra is the f^{-4} shape of the energy-containing part of the spectral tail (Toba 1973; Donelan *et al.* 1985; Battjes *et al.* 1987). Nonlinear quadruplet interactions have been ascribed a central role in maintaining the characteristic shape of wind-wave spectra (Young and Van Vledder 1993). Resio and Perrie (1991) have shown that in deep water, in the absence of other source terms, quadruplet interactions will tend to maintain the spectrum in a f^{-4} shape at frequencies higher than 1.5 times the peak frequency. Phillips (1985) proposes that in the equilibrium range, at frequencies much higher than the peak, a statistical equilibrium exists between the source terms of wind input, dissipation and nonlinear interaction. Assuming that S_{in} is proportional to $(u_*/c)^2$, Phillips finds that these three terms should all scale similarly with frequency. Starting from the same assumption of statistical equilibrium, Resio *et al.* (2004) suggest that it is only required that the terms of wind input and dissipation scale similarly with frequency to recover a deep water f^{-4} shape from the balance. Following the latter, we require that the dissipation term (4.13) should have the same frequency scaling as the wind input expression (4.15), which is proportional to $(u_*/c)^2$ for strongly forced wave components. This is achieved by constraining the exponent p in (4.13) to 4 for $u_*/c > 0.1$. For a tail shape of f^{-4}, the dissipation source term (4.13) then scales like f^{-1}, similar to the scaling of (4.15) for a high u_*/c (see Appendix A).

As the wave field gets older, its wind forcing u_*/c decreases over the energy-containing tail region. According to Resio and Perrie (1991) the quadruplet interactions still strive to maintain a f^{-4} shape over frequencies higher than 1.5 times the peak frequency. We therefore once again require that wind input and dissipation scale similarly with frequency to recover a spectral tail shape of f^{-4}. Under this weaker forcing, the wind input expression (4.15) goes over to a linear proportionality to u_*/c. To obtain similar frequency scaling, the exponent p in (4.13) should take the value 2 (Appendix A). It is therefore proposed that the parameter value p gradually changes from 4 to 2 as the wind input source term (4.15) goes over from a $(u_*/c)^2$ to a (u_*/c) proportionality. This suggests a secondary dependence of whitecapping on wave age, with decreasing dissipation intensity as wave age increases. Dependence of dissipation on wave age has been observed in the field by a number of investigators. Longuet-Higgins and Smith (1983) and Katsaros and Atakturk (1992) find that breaking probability increases proportionate to wind speed (or stress) and inverse wave age, and propose empirical expressions for breaking probability using these variables. More recently, Banner *et al.* (2000) and Babanin *et al.* (2001) find that for a diverse range of field situations the inclusion of wave age in the breaking determinant (alongside steepness as primary parameter) improves correlation in the prediction of breaking events. It can therefore be concluded that some dependence of the whitecapping source term on wave age appears to be justified.

Following the arguments above, the exponent p in (4.13) is constrained to $p = 4$ for $u_*/c > 0.1$ and $p = 2$ for $u_*/c < 0.1$. This is achieved by a simple transition expression for p, centred on $u_*/c = 0.1$:

$$p(u_*/c) = 3 + \tanh\left[w\left(\frac{u_*}{c} - 0.1\right)\right] . \tag{4.16}$$

where w is a shape parameter by which a smooth transition is obtained. A value of $w = 25$ is used here.

4.4.4 Finite-depth effects

Relatively little is known about the influence of finite water depth on the wave spectrum and the source terms of wind input, whitecapping and quadruplet interactions. Some guiding observations are available, however, and these were used to adapt the source term balance discussed above for use in finite water depths:

(a) Concerning whitecapping, Babanin *et al.* (2001) show that, upon correcting for breaking events due to depth restriction, data collected in the shallow Lake George $(0.7 < kd < 2.0)$ fit the relationship between breaking probability and frequency-local steepness established for deep water by Banner *et al.* (2000). This supports the applicability of the dissipation expression presented in Section 4.4 to finite depth environments.

(b) Concerning quadruplet interaction, a number of authors (e.g. Hashimoto *et al.*, 2003; Van Vledder and Bottema, 2003) have demonstrated that, according to the formulation of Hasselmann (1962), the interactions are significantly influenced by finite water depth. Yet, Resio *et al.* (2001) show that in water of finite depth—up to the surf zone—the shape stabilisation characteristic of quadruplet interaction yields an equilibrium tail shape of $F(k) \propto k^{-2.5}$, where $F(k)$ is the one-dimensional wavenumber spectrum, conforming to the deep water observations by, for example, Toba (1973) and Donelan *et al.* (1985). As the water depth further decreases, however, quadruplet interaction gives way to triad (three-wave) interaction as the dominant nonlinearity. This transition is reflected in the limitation in the applicability of the weakly nonlinear theory for quadruplet interaction in such regions. Zakharov (1999) shows that the weakly nonlinear theory is only valid for wave components for which $(ak)^2 << (kd)^5$, where a is the amplitude of the wave component.

(c) Concerning wind forcing, relations obtained in deep water are conventionally applied unaltered to finite water depth environments, except for the fact that the wind forcing parameter u_*/c may increase due to depth limitation. This approach has also been followed in the present study. Very recently, however, Donelan *et al.* (2006) have

provided field evidence that the increase in steepness of highly forced wind seas (being either very young or strongly depth-limited) may affect their growth rates significantly due to sheltering and flow separation. These effects are not included in the present study, but their potential impact is discussed in Sections 4.5 and 4.6.

(d) Concerning the wave spectrum, Kitaigorodskii *et al.* (1975) show that the deep water frequency spectrum gets affected by shallow water due to the shoaling and depth-induced breaking of its constituent waves. Bouws *et al.* (1985) propose that the frequency spectrum is transformed from $E(f) \propto f^{-5}$ in deep water to $E(f) \propto f^{-3}$ in very shallow water (the so-called TMA spectrum), based on an assumption that $F(k) \propto k^{-3}$ in deep and shallow water. By contrast, Miller and Vincent (1990) argue that the transition from deep to shallow water is rather from $E(f) \propto f^{-4}$ to $f^{-2.5}$, on the assumption of a tail shape in wavenumber space of $F(k) \propto k^{-2.5}$ (the so-called FRF spectrum).

The findings of Miller and Vincent (1990) and Resio *et al.* (2001) are in agreement with each other and also with the spectral shape of Donelan *et al.* (1985) that we have assumed for deep water. These results are therefore used as a basis for scaling the dissipation expression (4.13) for finite water depths. Assuming that quadruplet interactions will maintain a tail shape of $F(k) \propto k^{-2.5}$ in finite depth too, the same scaling arguments applied in Section 4.4.3 will maintain an $F(k) \propto k^{-2.5}$ spectral tail for the combination of all three deep water source terms as the water depth decreases. Appendix A shows that for weakly forced waves, $u_*/c < 0.1$ say, where $S_{in} \propto u_*/c$, the expressions (4.13) and (4.15) have similar scaling also in finite depth. However, for strongly forced waves, $u_*/c > 0.1$ say, where $S_{in} \propto (u_*/c)^2$, the scaling of the wind input expression (4.15) in finite depth differs from that of the whitecapping expression (4.13) by a dimensionless factor of $[\tanh(kd)]^{-1/2}$. Therefore, in order to obtain the desired equal scaling of these two source terms in finite depth, the whitecapping expression is adapted to

$$S_{dis,break}(\sigma, \theta) = -C'_{ds} \left[\frac{B(k)}{B_r} \right]^{p/2} [\tanh(kd)]^{\frac{2-p}{4}} g^{\frac{1}{2}} k^{\frac{1}{2}} E(\sigma, \theta) \qquad (4.17)$$

which reduces to (4.13) in weakly forced or deep water conditions. Due to the factor $[\tanh(kd)]^{(2-p)/4}$, strongly forced waves will experience increased dissipation in finite depth. In practice, however, this addition was found to have relatively little effect.

As mentioned above, the dominance of the source terms of wind input, whitecapping and especially quadruplet interaction decreases with decreasing water depth. Consequently, in very shallow water (defined by a high Ursell number, a high wave-height-over-depth ratio, or Zakharov's $(ak)^2 \approx (kd)^5$) the source term balance and spectral shape described above will give way to a balance determined by the shallow water source terms of bottom friction, depth-induced breaking and triad nonlinear interactions.

4.4.5 Non-breaking waves

The scaling arguments presented in the previous sections apply where $B(k) > B_r$ and waves break. According to Alves and Banner (2003), breaking-based dissipation of wave energy, dependent on $B(k)$, should cease when $B(k)$ is smaller than the threshold B_r. However, model runs using (4.17) as whitecapping expression showed that over the spectral regions where $B(k) < B_r$, typically somewhat below the peak frequency, a small amount of dissipation is required to ensure that an equilibrium growth level is reached at long fetches.

Dissipation of non-breaking waves can occur due to processes such as the interaction of waves with turbulence or momentum loss to wind (e.g. Tolman and Chalikov 1996; Ardhuin and Jenkins 2006). Since relatively little is known about the dissipation mechanisms of these low-frequency waves, they are not modelled in detail in the present study. Instead, the expression (4.1) is applied to provide general background dissipation of non-breaking waves, by setting $S_{dis,non-break} = S_{wc,Komen}$ in (4.11). Although this approach is analogous to that of Alves and Banner (2003), in the present study the expression (4.1) is only active for non-breaking waves.

To summarise, the proposed saturation-based whitecappping expression is given by:

$$S_{wc,SB}(\sigma,\theta) = f_{br}(\sigma)S_{dis,break} + [1 - f_{br}(\sigma)]\,S_{dis,non-break} \tag{4.11}$$

where

$$S_{dis,break}(\sigma,\theta) = -C'_{ds}\left[\frac{B(k)}{B_r}\right]^{p/2}[\tanh(kd)]^{\frac{2-p}{4}}\,g^{\frac{1}{2}}\,k^{\frac{1}{2}}\,E(\sigma,\theta) \tag{4.17}$$

and

$$S_{dis,non-break}(\sigma,\theta) = -C_{ds}\left(\frac{k}{\tilde{k}}\right)^q\left(\frac{\tilde{s}}{\tilde{s}_{PM}}\right)^r\tilde{\sigma}\,E(\sigma,\theta) \tag{4.1}$$

in which f_{br} is given by (4.12), $B(k)$ is given by (4.14) and p by (4.16).

For actively growing—and therefore breaking—wind sea the first term on the right-hand side of (4.11), namely the saturation-based dissipation given by (4.17) dominates. As a result, the dissipation expression has a cubic dependence on variance density for young, strongly forced waves and a quadratic dependence on variance density for mature, weakly forced waves. For non-breaking waves, for which $B(k) < B_r$, the second term on the right-hand side of (4.11), given by (4.1), dominates. For this part of the spectrum, the dissipation has a linear dependence on the variance density.

4.5   Simulations with saturation-based model

This section investigates the performance of the saturation-based model described above, and compares this performance to that of the default SWAN model. First, the calibration of the saturation-based model by means of fetch- and depth-limited growth curves is outlined. Subsequently, the calibrated model is evaluated for a number of field cases, including two cases featuring a combined swell–sea wave field, and two shallow lakes. These simulations are all conducted using the DIA for quadruplet interaction. Finally, the performance of the saturation-based model in combination with an exact method for the calculation of quadruplet interactions is investigated.

4.5.1   Calibration

Below, the calibration of the saturation-based model (4.11) in combination with the wind input expression (4.15) and the DIA quadruplet expression is presented. First, the calibration of this model for deep water fetch-limited conditions is outlined, followed by the calibration for finite depth conditions, where wave growth is limited by depth, rather than fetch or duration. All the simulations presented in this section were performed in stationary mode, with a sufficient number of iterations to ensure convergence.

Fetch-limited growth

The calibration of the saturation-based model for deep water was done by means of a series of nested one-dimensional simulations, with a geographical discretisation ranging from 1 m (at short fetches) to 10 km (at long fetches) and frequency and directional resolutions of $\Delta f / f = 0.1$ and $\Delta \theta = 10^o$ respectively. Figure 4.7 presents the deep water fetch-limited growth curves produced by the saturation-based model when the parameters of (4.17) are calibrated to $C'_{ds} \doteq 5.0 \times 10^{-5}$ and $B_r = 1.75 \times 10^{-3}$ and where p varies according to (4.16). For non-breaking waves, the proportionality coefficient C_{ds} in (4.1) was set to 3.0×10^{-5}. By means of comparison, the fetch-limited growth curves produced by the default model are also shown. In the top panels of Figure 4.7 it can be seen that both model variants (a) reproduce dimensionless energy and peak frequencies adequately over a wide range, (b) are in general agreement with the observations of Kahma and Calkoen (1992) (composite dataset) and (c) reach an equilibrium level at the Pierson and Moskowitz (1964) fetch range. The bottom panels of Figure 4.7 present the biases of the two models' results with respect to the growth curves of Kahma and Calkoen—the fetch range typically of interest to coastal wind-wave modelling. The calibrated saturation-based model produces smaller biases in both dimensionless energy and peak frequency than the default model. In particular, the general overprediction of the peak frequency by the default model is corrected.
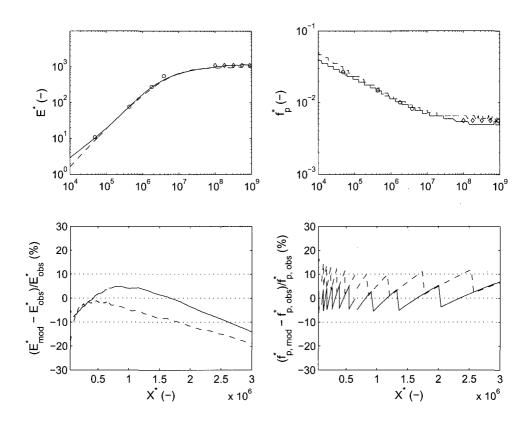
Figure 4.7: Deep water, fetch-limited growth curves produced by the saturation-based model (solid lines) and the default model (dashed lines), both using the DIA quadruplet method. Top panels: comparison with fetch-limited relations of Kahma and Calkoen (1992) (circles) and Pierson and Moskowitz (1964) (diamonds). Bottom panels: bias of model results with respect to Kahma and Calkoen (1992) data. Results for $U_{10} = 10$ m/s.
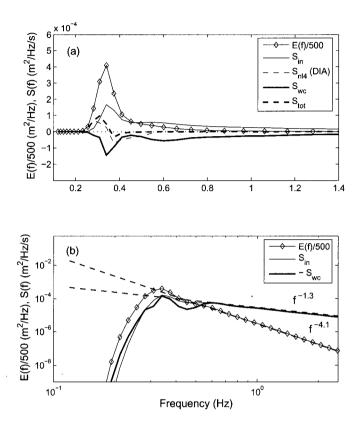
Figure 4.8: Source terms produced by the saturation-based model using the DIA quadruplet method. Panel (a): variance spectrum and all source terms on a linear scale, panel (b): variance spectrum and source terms of wind input and dissipation (absolute value) on logarithmic axes, with power law fits (dashed lines). Result for deep water, fetch-limited growth simulations with $U_{10} = 10$ m/s, at a fetch of $X^* = 7 \times 10^5$.

Figure 4.8 presents the spectral shapes of the computed source functions as well as their sum, as converged, at a dimensionless fetch of $X^* = 7 \times 10^5$. Figure 4.8(b) shows that in the spectral range above 1.5 times the peak frequency, the variance spectrum has an $f^{-4.1}$ decay, which is close to the desired tail shape found in observations. In this region the dissipation function reduces as $f^{-1.3}$, similar to the wind input function. This reflects the transition from an f^{-1} to an f^{-2} frequency scaling of these two terms at this intermediate wave age (u_*/c at the spectral peak is 0.08). At frequencies just below the spectral peak,
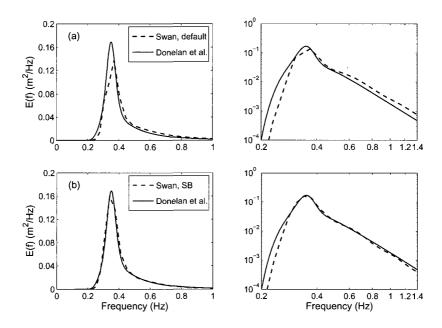
Figure 4.9: Deep water fetch-limited spectra produced using the default model (row (a)) and the saturation-based model (SB) (row (b)). Spectra on the left are repeated on the right on logarithmic axes. Results for $U_{10} = 10$ m/s at $X^* = 6 \times 10^5$.

the whitecapping term is weaker than the wind input term (Figures 4.8(a) and (b)). This is in contrast to the Komen *et al.* (1984) wind and whitecapping combination, where these terms are roughly of the same magnitude (result not shown). The dissipation just below the spectral peak is relatively low since the saturation spectrum $B(k)$ has low values here, and represents a situation in which waves cease to dissipate energy through breaking. Moving to even lower frequencies, the dissipation increases again relative to the strengh of the wind input, as the non-breaking dissipation mode in (4.11) becomes dominant. This division in dissipation modes is illustrated in Figure 4.6, in which the frequency spectra are compared with the breaking threshold B_r. It can be seen that the spectra produced by the saturation-based model lie above the saturation threshold over all frequencies except over the low frequency flank of the spectrum. Therefore, unlike in the original whitecapping expression of Alves and Banner (2003) discussed above, the saturation-based dissipation of breaking waves is active over a large part of the spectrum.

Figure 4.9 compares the spectra produced by the default and saturation-based models
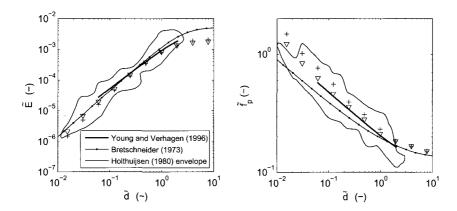
Figure 4.10: Depth-limited growth curves produced by the saturation-based model (inverted triangles) and the default model (plusses). Observations as indicated. Results for $U_{10} = 10$ m/s.

respectively with the parametric spectral shape of Donelan *et al.* (1985), parameterised with the peak frequency and total energy of Kahma and Calkoen (1992). The results shown are for a dimensionless fetch of $X^* = 6 \times 10^5$, which lies within the Kahma and Calkoen fetch range. As above, the default model produces some overestimation of the peak frequency, and predicted energy levels in the energy-containing tail region ($1.5 < f/f_p < 3$) are higher than those of the Donelan *et al.* spectrum. By contrast, the saturation-based model produces a lower peak frequency that is in good agreement with the Kahma and Calkoen value, and a tail that is lower in energy than with the default model, improving agreement with the Donelan *et al.* spectrum. Comparison with Figure 4.3 shows that the energy levels in the tail are also lower than those obtained when the default model is combined with the WRT exact quadruplet method. As noted above, these results are due to the distribution of the saturation spectrum $B(k)$, which causes greater dissipation in the spectral tail, and less around the peak than with the Komen *et al.* (1984) expression. The results produced by the saturation-based and default models also differ in their respective directional distributions. These are discussed in Section 4.5.3 below.

Depth-limited growth

The preceding section presented the calibration of the saturation-based model for deep water. Subsequently, the calibration of the saturation-based model for finite depth situations, using observations of idealised depth-limited growth, is outlined. Figure 4.10 compares the depth-limited growth results of the saturation-based model (4.11) combined with the wind input expression (4.15) with those of the default model. Here $\tilde{E} = g^2 E_{tot}/U_{10}^4$ and $\tilde{f}_p = f_p U_{10}/g$ are the dimensionless energy and peak frequency respectively and $\tilde{d} = gd/U_{10}^2$
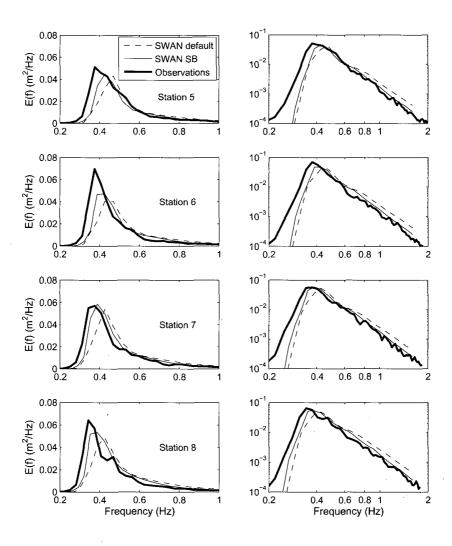
Figure 4.11: Simulations of depth-limited wave growth in Lake George, Australia. Spectra produced by the saturation-based model and by the default model, both using the DIA. Spectra on the left are repeated on the right on logarithmic axes. Observations are of Young and Verhagen (1996), with the dotted lines indicating the power law slopes of the observed spectral tails. Average wind speed is 10.8 m/s.

the dimensionless depth. The parameters of (4.17) and (4.1) retained their values as set in the deep water calibration. For both models, the shallow water source terms have been applied with their default formulations and parameter values (Booij *et al.* 1999), namely: bottom friction according to Hasselmann *et al.* (1973) with friction coefficient $C_{JON} = 0.067$ m^{2}s^{-3}, nonlinear triad interactions according to Eldeberky (1996), with co-efficient $\alpha_{EB} = 0.1$, and depth-induced breaking using Battjes and Janssen (1978), with coefficient $\alpha_{BJ} = 1.0$ and breaker parameter $\gamma_{BJ} = 0.73$. The model results are compared to the observations by Bretschneider (1973), Holthuijsen (1980) and Young and Verhagen (1996b). Figure 4.10 shows that the saturation-based model yields increased dimensionless energy and decreased peak frequencies compared to the default model, and that these results agree better with the observations than those of the default model. The improvement is the greatest at small dimensionless depths. To put this result into perspective, these changes in dimensionless energy and peak frequency are larger than those obtained when running the default model with either depth-induced breaking deactivated, or with the bottom friction coefficient C_{JON} reduced by half (results not shown).

To demonstrate the spectra produced by the saturation-based model in intermediate water depth, Figure 4.11 presents simulation results for the field case at Lake George, Australia, considered in Section 4.3 above. At Station 8, the downwind-most of the eight wave gauges, the spectral peak had a dimensionless depth of $k_p d = 1.2$, or, in relation to Figure 4.10, $\tilde{d} = 0.17$. Figure 4.11 shows that the saturation-based model, as calibrated, consistently yields more accurate predictions of the spectral peak frequency and energy than the default model. In addition, energy levels in the spectral tail are consistently lower than in the default model, improving the agreement with observations. Furthermore, comparison with Figure 4.5 shows that the saturation-based model, in combination with the DIA, also produces better agreement with observations of the peak frequency and energy levels in the tail than the default model in combination with exact computation of quadruplet interactions. On the basis of these results, it can be concluded that the saturation-based model can be applied over finite water depths without alteration to the default shallow water source terms.

4.5.2   Evaluation

In this section the saturation-based model (4.11) together with wind input (4.15), as calibrated for use with the DIA, is evaluated on the basis of a number of field cases. These include a case on a shelf sea and one in an embayment, both featuring combined swell–sea conditions, and a number of cases recorded at two shallow lakes.

Shelf sea with combined swell and wind-sea

A primary aim of this study is to address the spurious behaviour of the default SWAN model under combined swell–sea conditions, which occurs due to the dependence of the
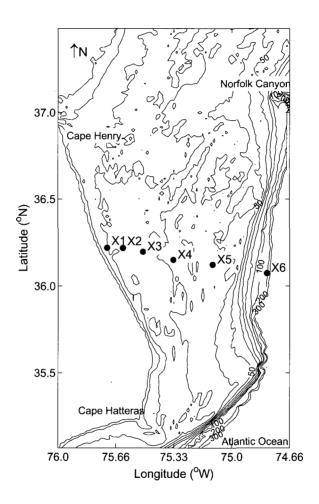
Figure 4.12: Bathymetry of the North Carolina shelf during SHOWEX (1999), including the locations of the observation stations X1 to X6 (after Ardhuin *et al.* (2007)).

Komen *et al.* (1984) whitecapping expression on mean spectral quantities. This section compares the performance of the default and saturation-based model versions, both using the DIA, under such conditions. Ardhuin *et al.* (2007) present results of field measurements off the coast of North Carolina, USA, in which deep water wave growth under near-idealised conditions was observed in combination with oceanic swell. Figure 4.12 shows the shelf sea area over which this mixed wave field was observed, including the array of wave observation stations X1 to X6. On 03/11/1999, from 12h00 to 17h00 local time, a fairly steady and uniform wind of about $U_{10} = 9.5$ m/s blew offshore from the west, at an angle of 20°–30° to shore normal. During this time, a moderate swell from ESE prevailed, nearly opposing the wind. Ardhuin *et al.* show that whereas the observed wind-sea growth at Stations X1 to X6 did not appear to be affected by the presence of the opposing swell, numerical models using the whitecapping expression of Komen *et al.* (1984) significantly overestimate the wind-sea for this field case where swell is present. The simulations conducted by Ardhuin *et al.* are repeated here using the default and saturation-based SWAN models.

Non-stationary simulations, running from 02/11/1999 23h00 to 03/11/1999 23h00, were performed over the area 76°–74.66^o W, 34.5^o–38° N with a spatial resolution of $1/60$ degree and a time step of 10 min. A frequency resolution of $\Delta f/f = 0.1$ and a directional resolution of $\Delta\theta = 10^o$ were used. A non-stationary wind field was applied, which was interpolated from observations taken at a number of offshore and nearshore stations in the area. Two sets of simulations were conducted, one without swell and one with swell included. In the latter series of simulations, the swell energy measured at the offshore Station X6 was applied as boundary condition at the offshore boundary running along 74.66^o W.

Figure 4.13 shows the simulation results at the downwind Station X6. Figure 4.13(a) presents the results of the first set of simulations, namely those in absence of swell. Following Ardhuin *et al.*, the results were averaged over the period 12h00–17h00, to reduce scatter. Ardhuin *et al.* find that the wind-sea component of the observed spectra agrees well with well-known growth curves (e.g. Kahma and Calkoen, 1992), from which they conclude that the wind-sea growth was not affected by the prevailing swell. The spectrum produced by the default SWAN model, however, overestimates the peak frequency and also the energy in the spectral tail, as was seen in the sections above (for pure wind-sea growth). The wind-sea-only simulation with the saturation-based model also yields fair agreement with the wind-sea part of the observed spectrum, with its peak frequency, peak energy density and spectral tail agreeing better with observations than those of the default model.

Figure 4.13(b) presents the corresponding model results at Station X6 for simulations in which the prevailing swell was included at the eastern model boundary, so that the wind-sea developed in the presence of an opposing swell field with a peak period of about 10 s. The default SWAN model is significantly influenced by the swell, as found by Ardhuin *et al.* in their simulations. Energy levels at both the spectral peak and tail are increased by about a factor 2. The peak frequency is also reduced, which partly corrects its overprediction in
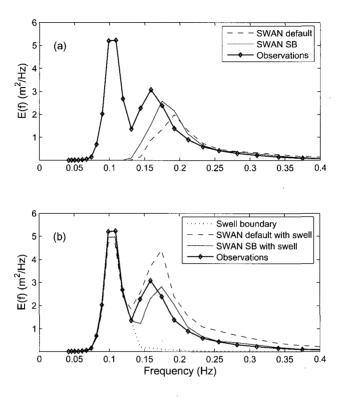
Figure 4.13: Results of simulations over the North Carolina shelf at downwind Station X6. (a) Spectra of the saturation-based and default models in simulations without swell. (b) Corresponding results of simulations with ambient swell. Average wind speed is $U_{10} = 9.5$ m/s.

simulations with wind only. However, as discussed in the introduction to this chapter, this improvement is spurious: swell reduces the mean spectral steepness, reducing the amount of whitecapping dissipation, which leads to excessive wind-wave growth. By contrast, the results produced by the saturation-based model, in which the breaking-based dissipation (4.17) does not depend on mean spectral quantities, is largely unaffected by the presence of the swell. Only small differences in the results are seen below the spectral peak frequency, where dissipation is described by (4.1).

Figure 4.14 presents the model results at Station X3, which is upwind of Station X6 and closer to the coast. At this location, the wind sea is younger than at Station X6, and
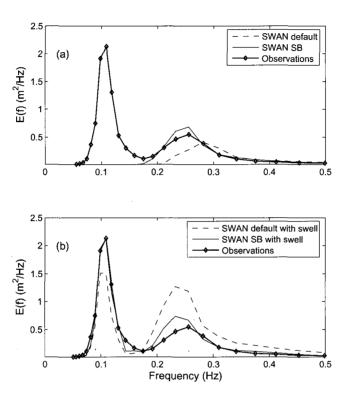
Figure 4.14: Results of simulations over the North Carolina shelf at downwind Station X3. (a) Spectra of the saturation-based and default models in simulations without swell. (b) Corresponding results of simulations with ambient swell. Average wind speed is $U_{10} = 9.5$ m/s.

the swell energy imposed on the boundary has travelled a significant distance into the model domain. Concerning the wind sea, similar results are obtained as at Station X6—in the presence of the swell condition the default model result is significantly affected, leading to a large overprediction of the wind sea component of the spectrum (compare Figures 4.14(a) and 4.14(b)). The results of the saturation-based model for the wind sea component are little affected by the presence of the swell, as seen above. A second important difference between the results of the default model and the saturation-based model here is the reproduction of the swell component. In both the default and saturation-based models the (non-breaking) swell is dissipated by an expression of the form (4.1),

which is a function of the mean frequency and mean steepness. However, since the default model significantly overestimates the wind sea component, and with it the mean frequency and steepness, swell energy is dissipated too strongly. In the saturation-based model, where the wind sea component is reproduced more accurately, the dissipation of the swell component remains limited, yielding good agreement with the observations.

From these results we conclude that in mixed swell and wind sea conditions the saturation-based model reproduces both the wind sea and the swell components more accurately than the default model.

Coastal embayment with combined swell and wind-sea

The second field case for which the model performance under combined swell and wind sea conditions is investigated is Lunenburg Bay, a coastal embayment on the southern shore of Nova Scotia, Canada (Figure 4.15). Lunenburg Bay is approximately 8 km long, 4 km wide and has an average depth of about 10 m (Figure 4.16). The bathymetry is irregular and the bay is exposed to wave and tidal energy from the North Atlantic Ocean from easterly and southerly directions. Incident waves refract around an offshore island and encounter a 2 to 5 m deep rocky shoal toward the eastern side of the bay. South of the shoal, a 20 m deep channel penetrates the bay. Swell energy is significantly reduced during its propagation through the bay, so that at the bay's western end conditions are dominated by tidal forcing. Spring and neap tides range between 2 and 1 m. Wave observations in the bay have been made by Mulligan *et al.* (2005) using several instruments, including (Figure 4.16): a directional buoy (Station D), pressure sensors with co-located acoustic current meters (stations P1 and P2), and acoustic current profilers (stations A1, A2 and A3). Wind observations were made at three sites, namely at two buoys located at stations P1 and P2, and a land-based meteorological station (Station W).

Tropical Storm Nicole passed close to the coast of Nova Scotia on 11–12 October, 2004 (Figure 4.15). The storm's passing created complex nonstationary conditions inside the bay, featuring combined swell and wind sea. Figure 4.17 shows the low-frequency wave energy registered at Station D during the course of the storm, which was created offshore by the approaching hurricane. Figure 4.18 shows the wind data observed at three stations in Lunenburg Bay during the same period. Figure 4.18 shows that ahead of the hurricane's passing there was a constant N wind. During the passing, the wind direction changed rapidly to E, subsequently to SE, and then rotated anti-clockwise to NW. Figure 4.18 also presents the water levels recorded at Station A1 during the passage, which shows mainly tidal variation, but also include surge associated with the tropical storm.

This field case was simulated with SWAN in non-stationary mode using both the default and the saturation-based whitecapping formulations, both with the DIA. The processes of bottom friction, triad nonlinear interaction and depth-induced breaking were modelled using their default formulations given in Section 4.5.1. The discretisations used for both model variants were $\Delta x = \Delta y = 60$ m in geographical space, $\Delta f / f = 0.1$ in frequency
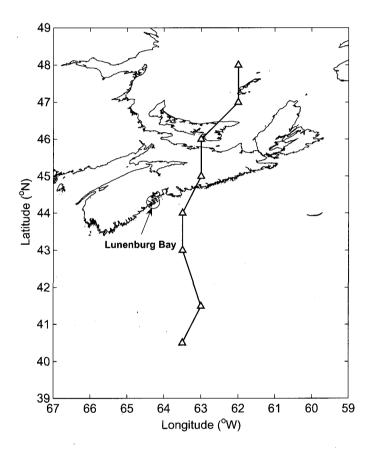
Figure 4.15: Map showing location of Lunenburg Bay in Nova Scotia, Canada, and the track of Tropical Storm Nicole, which passed in October 2004 (line with triangles).
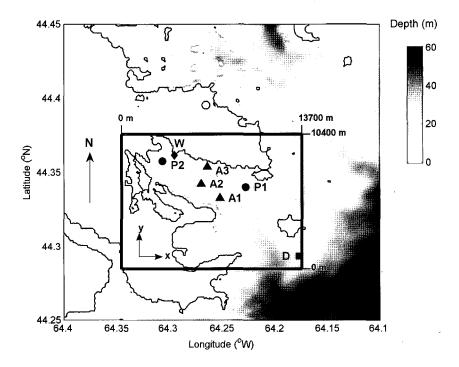
Figure 4.16: Map of Lunenburg Bay showing bathymetry and instrument locations in 2004. Instrumentation included a directional waverider buoy denoted by D, acoustic current profilers denoted by A1–A3, surface meteorological buoys and bottom pods with pressure sensors and co-located current meters, denoted by P1 and P2, and a land-based meteorological station denoted by W.
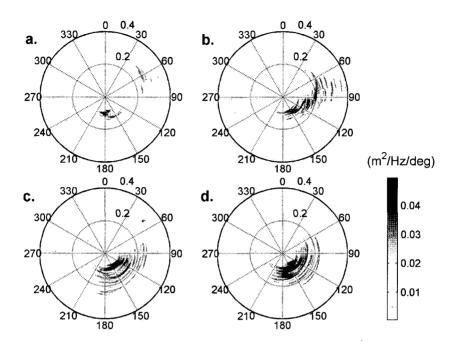
Figure 4.17: Directional spectra observed at the waverider buoy D. Observations shown at nine-hourly intervals: (a) 11/10/2004 at 17h30, (b) 12/10/2004 at 02h30, (c) 12/10/2004 at 11h30 and (d) 12/10/2004 at 20h30.

space, including the frequencies 0.03 to 3.00 Hz, and $\Delta\theta = 10°$ in directional space, around the full circle. A time step of $\Delta t = 30$ min was used both for the computation and for the updating of the wind forcing and water levels. The start time of the simulation was 11/10/2004 at 12h00. Directional spectra for the wave boundary conditions were obtained from the directional buoy at Station D with the directional spreading estimated using the Maximum Entropy Method (MEM). These observed spectra (swell) were applied uniformly along the eastern and southern model boundaries. The wind observations at Station P1 (representative of winds over the eastern half of the bay) were used as the time-varying wind forcing in the model, assumed spatially uniform over the bay. Water level observations taken at Station A1, also assumed uniform over the bay, provided the time-varying water depth.

Figure 4.19 shows the simulated frequency spectra at three instants during the simulated period, namely before the hurricane passage, during the passage and towards the end of the hurricane passage respectively. The simulated and observed spectra are compared at
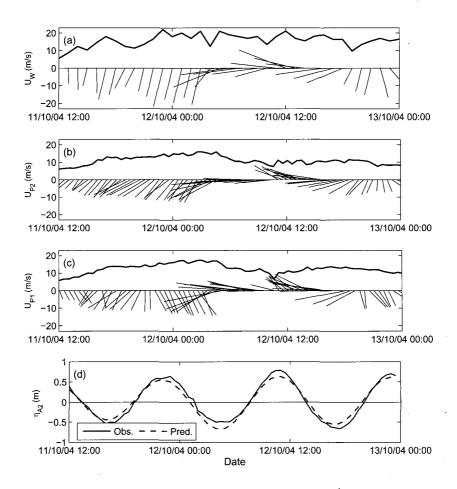
Figure 4.18: Wind and tidal water level observations over the simulation period of Tropical Storm Nicole. Wind speeds are given by the thick solid line in panels (a) to (c), with the feather plots showing speed and direction. The panels show: (a) hourly winds at land station W, (b) half-hourly winds at surface buoy P2 and (c) half-hourly winds at surface buoy P1. Panel (d) shows the water level change from mean at bottom pod A2.
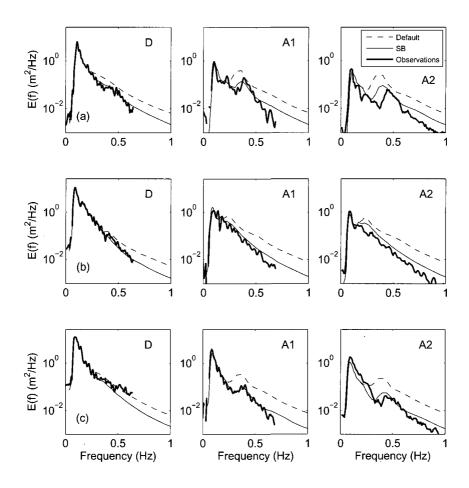
Figure 4.19: Comparison between observed and simulated spectra at three instants during the passing of Hurricane Nicole. Row (a): 11/10/2004 at 20h30; Row (b) 12/10/2004 at 14h30; Row (c): 12/10/2004 at 20h30. At each storm instant, results are shown for three locations, namely the model boundary (Station D), the bay mouth (Station A1) and at mid-bay (Station A2).
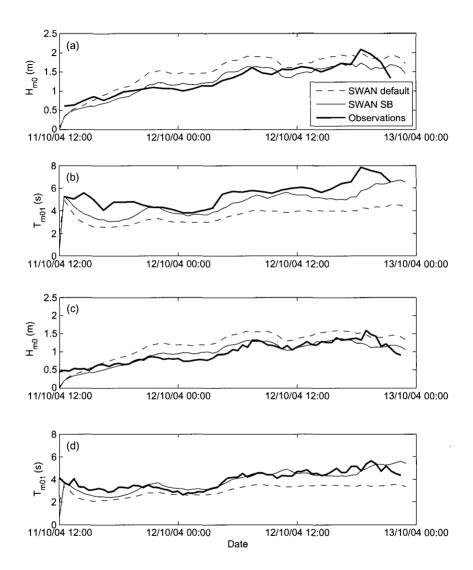
Figure 4.20: Observed and simulated time series of significant wave height and mean period at Station A1 (panels (a) and (b)) and Station A2 (panels (c) and (d)).
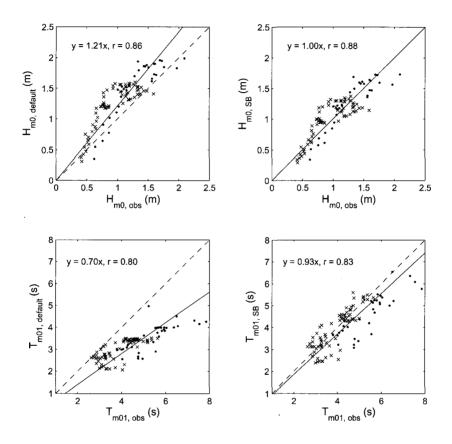
Figure 4.21: Scatter plots of model results of significant wave height and mean period against data, at sites A1 (•) and A2 (×). Left-hand panels show results of default model, and right-hand panels show results of saturation-based model. Dashed line indicates perfect agreement and solid line indicates the regression fit, forced through the origin.

the offshore wave buoy D (output at one grid cell removed from the boundary), at Station A1 in the bay mouth and at Station A2 at mid-bay. With reference to the swell and wind observations presented above, Figure 4.19(a) shows SSE swell entering the bay with a superimposed N wind sea, which appears as a spectral peak around 0.4 Hz at stations A1 and A2. During the passage of the hurricane, the swell and wind directions are aligned, resulting in single-peaked spectra at stations A1 and A2 (Figure 4.19(b)). Towards the end of the hurricane passage, the incoming swell and the local wind sea are directionally opposed, so that the spectra at stations A1 and A2 are again bi-modal (Figure 4.19(c)). The model results presented in Figure 4.19 show that, with respect to the generation of wind sea, the saturation-based model yields consistently better agreement with the observations than the default model. Due to the default whitecapping expression's dependence on the mean spectral wavenumber and steepness, the default model overestimates the magnitude of the wind sea component throughout the simulation. By contrast, the saturation-based model—in which the dissipation of the breaking wind sea is independent of the presence of the swell—gives a better estimate of the amount of wind sea energy in the bay.

The difference in model performance is also seen in the time series of significant wave height and mean period at Stations A1 and A2 (Figure 4.20). The overprediction of the wind sea growth by the default model seen above leads to an overestimation of the significant wave height and an underestimation of the mean period. This occurs at both Station A1 and A2 during most of the simulation period. Consistent with the improved estimation of the wind sea component by the saturation-based model, the integral parameters produced by this model variant are in better agreement with the observation than the default model. To summarise these results, Figure 4.21 compares scatter plots of the observed and modelled significant wave height and mean period at Stations A1 and A2. Also presented are least-squares regression lines and the coefficient of linear correlation r between the observations and model results. These scatter plots show that the default model overestimates the significant wave height and strongly underestimates the mean period due to the inaccurate estimation of the wind sea (average errors of +21% and -30% respectively). These errors are much reduced in the results of the saturation-based model (average errors of 0% and -7% respectively). In addition, the correlation r between the saturation-based model results and observations is somewhat higher than that between the default model and the observations.

It can be concluded from these results that the decoupling of swell and wind sea in the whitecapping formulation has improved the overall model performance under combined swell and wind-sea conditions.

Shallow lakes

To evaluate the saturation-based model's performance in finite depth water, this section considers the simulation of a collection of field cases recorded at Lake IJssel and Lake Sloten, two shallow lakes in The Netherlands. Figure 4.22 presents a contour plot of Lake IJssel, including the locations of five wave observation stations. Winds were measured at Stations FL2 and FL26. Lake IJssel is relatively shallow, with a depth of about 5 m
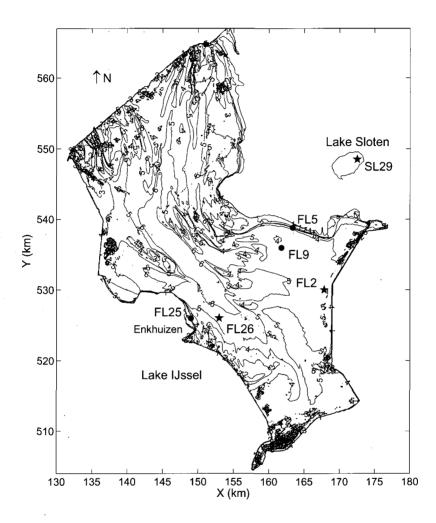
Figure 4.22: Map of Lake IJssel, The Netherlands, including the locations of wave (dots) and combined wave and wind (stars) observation stations. Depth contours in m below NAP. The outline of Lake Sloten is shown to the same scale for comparison (after Bottema 2004).

Table 4.1: Details of selected Lake IJssel cases

Case	Y-A	Y-B	Y-C	Y-D
Date	2/10/1999	27/10/2002	12/11/2002	2/4/2003
Time	3-4h	14h20-15h20	13-14h	14-15h
Water level (m NAP)	-0.12	+0.23	-0.25	-0.11
Wind speed (m/s)	15.2	23.8	10.3	15.1
Wind dir. (deg. N)	215°	249°	192°	325°

at Station FL26 in the west, sloping to a depth of about 4 m at Stations FL2 and FL9 towards the east. Bottema (2004) selected four cases suitable for model evaluation from measurements at Lake IJssel, based on the following criteria: (a) the measured wind field was to be spatially uniform (differing by less than 5% at Stations FL2 and FL26) and (b) stationary conditions were to prevail for at least two hours. These four cases, labelled Y-A to Y-D, are listed in Table 4.1. Water levels are given relative to the Dutch datum NAP (approximately mean sea level), and the direction from which the wind is blowing is measured clockwise from North. On the basis of wind speed, these storm events can be considered to range from deep water situations (case Y-C) to intermediate water depth situations (case Y-B). Considering the small geographical extent of the model area and the stationarity of the physical conditions, model runs were conducted in stationary mode. Wind fields were applied spatially uniform. A spatial discretisation of $\Delta x = \Delta y = 250$ m and spectral discretisations of $\Delta f/f = 0.1$ and $\Delta \theta = 10^o$ were used. All simulations were conducted using the DIA for computing quadruplet interaction.

Figures 4.23 and 4.24 present the simulation results for two of the selected Lake IJssel cases. Figure 4.23 shows that for case Y-C (moderate wind speed) the peak frequencies produced by the default model agree well with the observations at Stations FL9 and FL26, but are slightly higher than the observations at the downwind locations FL2 (deep) and FL5 (shallow). Similarly, total energy is fairly well predicted by the default model at Stations FL9 and FL26, but underpredicted at the downwind stations FL2 and FL5. By contrast, the saturation-based model predicts the peak frequencies well at some stations and underpredicts them somewhat at others. The values of total energy produced by the saturation-based model are consistently higher than those of the default model, improving on the latter's underestimations at downwind stations FL2 and FL5. The exception to these results is the upwind location FL25, which has a short fetch of about 1 km ($X^* \approx 7 \times 10^4$ for this wind speed). At this station, energy levels are strongly overpredicted by both the default and the saturation-based models, even though, for a corresponding dimensionless fetch X^*, the saturation-based model's result agrees with the Kahma and Calkoen (1992) growth curve (see Figure 4.7). Sensitivity analyses suggest that these overpredictions may be due to the use of a spatially uniform wind field, which does not take into account a local decrease in wind speed offshore of the land-sea transition, as described for example by Taylor and Lee (1984). Other possible explanations are that the conventional wind
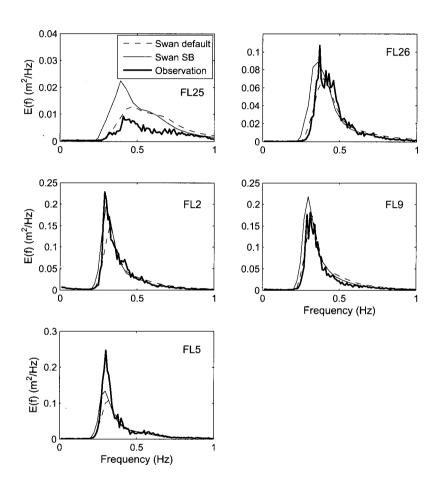
Figure 4.23: Simulated spectra at five observation points in Lake IJssel for case Y-C. Wind speed $U_{10} = 10.3$ m/s and direction 192° (SSW). Compared are the simulation results of the saturation-based and default models, and observations.
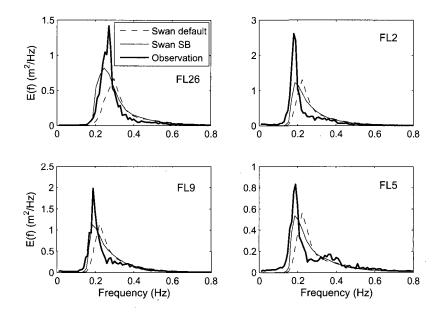
Figure 4.24: Simulated spectra at four observation points in Lake IJssel for case Y-B. Wind speed $U_{10} = 23.8$ m/s and direction 249° (WSW). Compared are the simulation results of the saturation-based and default models, and observations.

input expressions applied in the model may overestimate the momentum transfer to this very young wave field (Donelan *et al.* 2006) or that at these early stages of development the waves themselves behave in a non-self-similar fashion, falling outside the current wind-wave modelling paradigm (Badulin *et al.* 2005). Consequently, the verifiability of model results at this station remains uncertain, and the results at this station are omitted from the remainder of the evaluation.

Figure 4.24 presents the results of case Y-B, where the wind came from the same directional quadrant as in case Y-C, but had a much higher speed. Under these conditions, the default model consistently overpredicts the peak frequency and underpredicts the total wave energy. This frequency overprediction is most evident at the downwind locations FL2, FL9 and FL5. By contrast, the saturation-based model accurately predicts the peak frequency at most locations, and the predicted total energy is slightly higher than with the default model. The remaining cases Y-A and Y-D, of which the spectra are not shown, yield similar results to those discussed.

Table 4.2: Details of selected Lake Sloten cases

Case	SL-A	SL-B	SL-C	SL-D	SL-E
Date	27/10/2002	26/2/2002	12/2/2002	10/2/2002	10/10/2002
Time	15-16h	14-15h	13-14h	4-5h	12-13h
Water level (m NAP)	-0.45	-0.29	-0.43	-0.47	-0.47
Wind speed (m/s)	21.4	20.8	15.0	11.0	10.6
Wind dir. (deg. N)	252°	243°	253°	245°	88°

Lake Sloten is considerably smaller and shallower than Lake IJssel, with a greatest length of
4 km and depths of about 1.6 to 1.8 m in the cases considered here (its outline is included in
Figure 4.22 for comparison). Figure 4.25 presents a contour plot of Lake Sloten, indicating
its only wave and wind observation station, SL29. Bottema (2004) selected five cases for
this site, cases SL-A to SL-E given in Table 4.2, based on the criteria (a) that stationary
conditions prevailed, and (b) that the selected cases were typical of those found at this
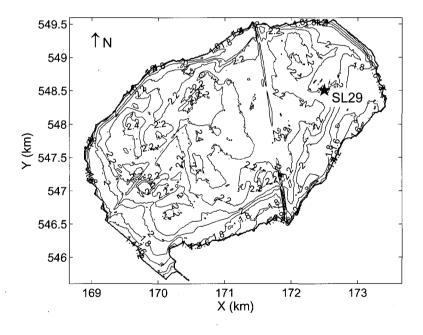
Figure 4.25: Map of Lake Sloten, The Netherlands, including the location of the wave
and wind observation station SL29. Depth contours in m below NAP (after Bottema 2004).
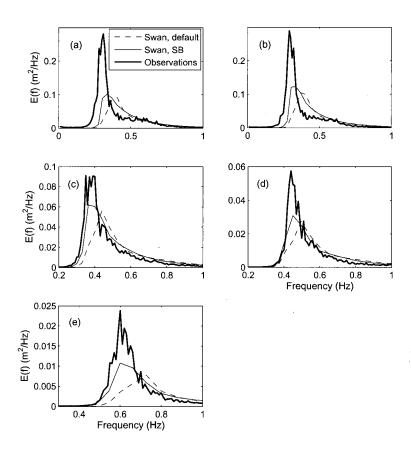
Figure 4.26: Simulated spectra of five cases observed at Lake Sloten: (a) SL-A, with wind speed $U_{10} = 21.4$ m/s, WSW, (b) SL-B, $U_{10} = 20.8$ m/s, WSW, (c) SL-C, $U_{10} = 15.0$ m/s, WSW, (d) SL-D, $U_{10} = 11.0$ m/s, WSW and (e) SL-E, $U_{10} = 10.6$ m/s, E. Compared are the simulation results of the saturation-based and default models, and observations.
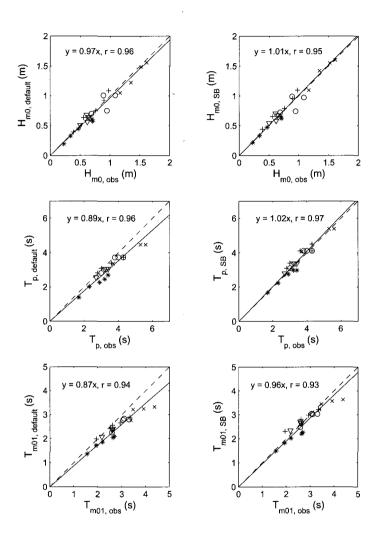
Figure 4.27: Scatter plots of H_{m0}, T_p and T_{m01} produced by the default (left-hand panels) and saturation-based (right-hand panels) models versus observations, for the Lake IJssel and Lake Sloten simulations. Included are the following cases from Tables 4.1 and 4.2: Y-A ($\circ$), Y-B ($\times$), Y-C ($\triangledown$), Y-D ($+$) and SL-A to SL-E ($*$). Dashed line indicates perfect agreement and solid line indicates the regression fit, forced through the origin.

site. Of these, cases SL-A to SL-D feature moderate to strong WSW winds with a fetch of 3 km, and case SL-E a moderate easterly wind, with a short fetch of 1 km. The wave fields in the high wind speed cases have dimensionless depths at the spectral peak as low as $k_p d = 0.9$ (or $\tilde{d} = 4 \times 10^{-2}$). Simulations were conducted in stationary mode, using a spatial discretisation of $\Delta x = \Delta y = 40$ m and spectral discretisations of $\Delta f / f = 0.1$ and $\Delta \theta = 10^o$.

Figure 4.26 presents the simulation results for these five cases at Station SL29. With the default model, peak frequencies are overpredicted and the energy density at the peak is too low throughout. The predictions of the saturation-based model consistently improve on these results. This improvement is most significant, and the correlation with observations the best, for the cases SL-C, SL-D and SL-E, where moderate to moderately high wind speeds prevailed. In cases SL-A and SL-B, where wind speeds were high, peak frequencies are still somewhat overestimated and energy levels at the spectral peak remain significantly underpredicted by the saturation-based model. Furthermore, particularly for these two cases, the observed spectral shape has a large peak enhancement, that is not found in the simulation results of either the saturation-based or the default models.

To summarise these results, Figure 4.27 presents scatter plots of the integral parameter results for Lake IJssel and Sloten produced by the default and saturation-based models. Also presented in these plots are least-squares regression lines and the coefficient of linear correlation r between the observations and model results. The left-hand panels of Figure 4.27 present the performance of the default model: significant wave heights are well predicted, with an average error of -3%, but peak and mean periods are underpredicted, with average errors of -11% and -13% respectively. The right-hand panels show the corresponding results for the saturation-based model: the significant wave height is overestimated with an average error of $+1\%$. A large improvement over the default model is found in the period measures. The peak period, which is underpredicted by the default model, is overpredicted by only $+2\%$. Furthermore, the underprediction of the mean period T_{m01} by the default model is reduced to -4% in the saturation-based model. The results of the correlation coefficient r show similar, high correlations between the results of both model variants and the observations.

4.5.3 Saturation-based model with exact quadruplet interactions

The simulations presented thus far were done by combining the saturation-based model with the DIA method for calculating quadruplet interactions. Because of its computational efficiency, the DIA is currently used in most operational wave models. However, in Section 4.3 it was shown that some gain in model accuracy is found when the DIA is replaced by an exact method for computing quadruplet interactions, such as the WRT method. In this section we shall highlight some characteristics of the saturation-based model (4.11) and wind input (4.15) when combined with the WRT exact method.

directional distributions. Figure 4.29 shows that at frequencies higher than the peak, the saturation-based model, using the DIA, produces narrower directional distributions than the default model. A similar finding was reported by Alves and Banner (2003) using (4.8). They ascribed it to the greater strength of the saturation-based whitecapping expression relative to the quadruplet term in this spectral region. This decreases the energy levels at angles away from the mean propagation direction. In addition—as was found for the default model in Section 4.3—a characteristic consequence of using an exact quadruplet method is that the directional distribution becomes bi-modal at higher frequencies. Figure 4.29 compares the directional distribution of energy with the observations of Hwang *et al.* (2000), showing that the bi-modal directional distribution is preserved when the WRT is combined with the saturation-based model.

From the above it is seen that the results of the saturation-based model improve somewhat when combined with the WRT method. However, the benefits obtained by using the more detailed description of quadruplet interactions are offset by longer computational times—simulations using the WRT method require 300 times as much computational time as those using the DIA. For typical coastal engineering applications the improvement in model results obtained by combining the saturation-based model with the WRT does not justify this large increase in computational cost. However, Van Vledder (2005b) discusses methods by which the computational cost of the WRT method can be reduced without significant loss in accuracy. Simulation time can also be reduced by using the parallel computing facilities available in SWAN (Zijlema 2005). Using such methods, model runs with the WRT may be viable for selected cases in engineering applications.

4.6   Conclusions

This study investigated whether the accuracy of SWAN, specifically with regard to period measures, could be improved by using an exact method for the calculation of quadruplet interaction and alternative formulations of the whitecapping expression. In particular, a whitecapping expression based on that of Alves and Banner (2003) was investigated, in which dissipation due to actively breaking waves is only dependent on quantities that are local in frequency space. The dissipation of non-breaking waves (typically at frequencies below the spectral peak) was modelled using the expression of Komen *et al.* (1984), which is dependent on spectral mean quantities. This combined dissipation expression was used together with a wind input term based on that of Yan (1987). The source term combination featuring the new whitecapping and wind input expressions was calibrated against fetch- and depth-limited growth curves and subsequently evaluated for field cases with combined swell–sea wave conditions and a number of shallow water field cases. Finally, the performance of the new whitecapping and wind input source terms in combination with the exact calculation of quadruplet interaction was investigated. The following conclusions can be drawn from this study:

(a) Combining the default wind input and whitecapping source terms with an exact method for computing quadruplet interaction yields some correction to the overprediction of the peak frequency observed in the default model combined with the DIA. Furthermore, using an exact quadruplet method improves the directional distribution at higher frequencies, yielding bi-modal distribution of energy in accordance with observations. However, when using the WRT exact method, some discrepancies still remain between simulated and observed peak frequencies, and energy levels in the spectral tail remain overpredicted.

(b) In idealised fetch-limited growth simulations, the investigated saturation-based model, using the DIA, yields more accurate estimates of dimensionless energy and peak frequency than the default model within the Kahma and Calkoen (1992) fetch range. In particular, the peak period underprediction of the default model is corrected by this new model. The investigated model also yields lower energy levels in the spectral tail than the default model, bringing it in closer agreement with observations.

(c) In idealised depth-limited growth simulations, the investigated saturation-based whitecapping expression yields higher dimensionless energy and lower dimensionless peak frequencies than the default model values, improving agreement with observations.

(d) In the saturation-based whitecapping expression, the dissipation of higher-frequency breaking waves is dependent on quantities that are local in frequency space. Under combined swell–sea wave conditions, the wind sea contribution produced by the saturation-based model is therefore not significantly affected by the presence of background swell. This is in contrast to the performance of the default model which—due to the dependence of the dissipation of all components on the mean spectral steepness and wave number—has been shown to greatly overpredict the wind-sea part of the spectrum under such conditions. As a secondary effect, swell is overly dissipated in the default model since the mean steepness and wave number, on which the dissipation depends, are overpredicted along with the wind sea. It should be noted that even though in this study the decoupling of the dissipation of swell and sea has been shown to improve model reliability, some studies, for example Banner *et al.* (1989), Meza *et al.* (2000) and Young and Babanin (2006), have produced evidence of coupling of dissipation across the spectrum. Such effects could be parameterised and added as additional dissipation terms to the action balance equation, as proposed by Young and Babanin (2006), for example, rather than being included as multiplication factors, as proposed by Alves and Banner (2003).

(e) In shallow lakes, the investigated saturation-based model generally yields satisfactory results. The saturation-based model yields higher peak and mean periods than the default model (biases of +2% and -4% respectively versus -11% and -13% respectively in the default model), which corrects the underprediction of these parameters by the default model for the most part. The investigated and default models perform almost

equally well in predicting significant wave height, with a bias of -3% in the default model and +1% in the saturation-based model, and high correlations.

(f) Less positive results were found in the shallow lakes over very short dimensionless fetches, such as for station FL25 at Lake IJssel under SW wind, where the total spectral energy is significantly overestimated. Such discrepancies may be caused by insufficient accuracy in the wind data, exclusion of some important wind input mechanisms (e.g. Donelan *et al.*, 2006), or non-self-similar behaviour by the waves (e.g. Badulin *et al.*, 2005). It was also found that at small dimensionless depths, such as the strong wind cases at Lake Sloten, both the spectral peak period and the peak enhancement are still underestimated by the investigated model. This may point to shortcomings in the shallow water source terms employed, or may again be due to neglected wind input mechanisms or non-self-similar behaviour in these strongly forced, shallow water waves.

(g) Combining the saturation-based model with the WRT exact quadruplet expression, instead of the rather inaccurate DIA, leads, in addition to the improvements mentioned under (b), to improvements in the details of the directional distribution at higher frequencies. However, such an exact quadruplet method requires much additional computation time, making it unsuitable for operational use at present. Van Vledder (2005b) presents various possibilities for reducing the computational cost of the WRT method without compromising its results, and parallel computing facilities are available in SWAN (Zijlema 2005), so that such model runs could be conducted for selected cases.

Chapter 5

Source terms in shallow water

5.1 Introduction

A distinguishing feature of spectral wave models such as SWAN and TOMAWAC in comparison to those designed for oceanic application (such as WAM and WAVEWATCH III) is the inclusion of source terms that model the shallow water processes of depth-induced breaking and triad nonlinear interaction. The latter process is responsible for the phase coupling of spectral components, which causes the characteristic steepening and forward pitching of wave crests in shallow water, and the generation of difference frequency components ('surf beat'). The inclusion of these shallow water processes, which dominate the other source terms in the surf zone, enables SWAN to model the evolution of swell and wind-sea spectra from the open ocean, over the oceanic shelf and through the surf zone. This capability is applied, for example, to compute wave fields for sediment transport calculations and wave conditions at coastal defenses. A number of studies have shown that within the surf zone SWAN simulates significant wave height adequately, but that wave spectra and mean period measures tend to be inaccurate (e.g. Ris *et al.* 1999). This suggests deficiencies in the redistribution of energy across the spectrum by triad interaction, or incorrect modelling of the spectral distribution of depth-induced breaking. Another possibility is that the interaction between the shallow water source terms and the expressions for wind input, whitecapping and quadruplet interaction leads to erroneous results. It is the aim of this chapter to investigate these possibilities, in order to arrive at an improvement in the accuracy of shallow water modelling by SWAN.

A stochastic description of the nonlinear evolution of the nearshore wave field is obtained by ensemble averaging of a set of deterministic equations describing the water surface displacement. This yields an infinite hierarchy of equations governing the evolution of the spectral moments of the wave field (e.g. Herbers and Burton 1997): at the lowest order, an expression for the spatial evolution equation for the variance density spectrum

(second-order moment) is found, which includes the third-order cumulant term, namely the bispectrum. The bispectrum is defined as the Fourier transform of the third-order correlation function of the time series of water surface displacement. It carries information about the statistical correlation between the phases of wave components, and therefore the departure from Gaussianity (Hasselmann *et al.* 1963). A second equation is required to describe the spatial evolution of the bispectrum, which in turn includes the fourth-order cumulant term, namely the trispectrum. This expansion can be continued indefinitely, but is typically truncated at the evolution equation for the bispectrum by means of a closure hypothesis (the fourth-order cumulant hypothesis). Similar closure hypotheses are applied in, for example, turbulence modelling.

Nonlinear spectral wave modelling through the surf zone using the above technique was first undertaken by Abreu *et al.* (1992), and has been developed further with a range of approaches in recent years. These can be categorised according to (a) the type of deterministic equations employed to describe the water surface displacement, (b) the closure hypothesis applied for the fourth-order cumulant and (c) the degree to which the evolution equation for the bispectrum is parameterised. Firstly, concerning the type of underlying deterministic equations, earlier models employed Boussinesq-type equations (Eldeberky 1996, Herbers and Burton 1997, Kofoed-Hanssen and Rasmussen 1998 and Becq-Girard *et al.* 1999) and the so-called Zakharov kinetic integral (Eldeberky *et al.* 1996). The drawback of using Boussinesq-type deterministic equations is that the description of linear dispersion and coupling coefficients is valid only for weakly dispersive waves, and is therefore only valid in relatively small dimensionless depths (Becq-Girard *et al.* 1999). The use of full-dispersion evolution equations (Agnon and Sheremet 1997, Eldeberky and Madsen 1999 and Janssen 2006) has removed this limitation.

Secondly, with regard to the closure hypothesis used, a frequently-applied technique is the so-called quasi-normal closure, in which the fourth-order cumulant is set to zero (Eldeberky *et al.* 1996, Herbers and Burton 1997 and Kofoed-Hassen and Rasmussen 1998). This approach leads to poor and even unphysical model performance in the surf zone, where nonlinearity and dissipation are strong (Herbers *et al.* 2003). Alternatives are proposed by Holloway (1980), Herbers *et al.* (2003) and Janssen (2006). In the latter two studies, the closure hypothesis includes a heuristic relaxation term, which induces a return to Gaussian statistics in the presence of strong nonlinearity and dissipation, thus improving model performance in the surf zone.

Thirdly, concerning the degree of parameterization of the bispectrum, a number of approaches have been pursued: the so-called two-equation models solve both the spectral and bispectral evolution equations entirely (save for the hypothesis for the fourth-order cumulant), and therefore give the most complete representation of the underlying physics. These models have been derived for uni-directional wave fields (Freilich and Guza 1984 and Rasmussen 1998), directional wave fields over one-dimensional topography (Herbers and Burton 1997, Agnon and Sheremet 1997, Eldeberky and Madsen 1999, Herbers *et al.*

2003) and directional wave fields over quasi two-dimensional topography (Janssen 2006). Considering the modelling of directional wave fields, the two-equation models of Agnon and Sheremet (1997), Eldeberky and Madsen (1999) and Janssen (2006) can be considered to be the current state of the art, with that of Janssen (2006) having the advantage of accommodating weak lateral variation in topography. However, the full solution of the bispectral evolution is time-consuming, so that, with a view to operational wave models, the equation for the bispectrum has been parameterised. For example, Eldeberky (1996), Rasmussen (1998) and Becq-Girard *et al.* (1999) consider the bispectrum to depend only on local variables in space, and thus to have no memory of upwave conditions. The expression for the bispectrum is subsequently incorporated into the evolution equation for the variance density spectrum, resulting in a so-called one-equation model. These are computationally less expensive than the two-equation models, but at the cost of added assumptions and simplifications.

The Lumped Triad Approximation (LTA) model of Eldeberky (1996) simplifies and speeds up the one-equation model approach even further by considering only the interactions of components with themselves, for a uni-directional wave field. Therefore, at the cost of adding these further assumptions, the LTA is very computationally efficient. This low computational cost has made the LTA attractive for use in SWAN for operational applications, and is the current default expression used. However, a number of researchers (e.g. Rasmussen 1998 and Becq-Girard *et al.* 1999) have demonstrated important deficiencies in the LTA's performance, such as the overestimation of the first superharmonic of the spectral peak (at twice the peak frequency) and the absence of the second superharmonic. It can therefore be expected that a significant proportion of the inaccuracy in surf zone predictions by SWAN is due to the LTA.

Recently, Holthuijsen and Booij (2007) proposed a new approach to triad parameterisation, by modelling this process in analogy to quadruplet interaction. Their expression is based on a quadruplet formulation, with one interaction component removed, in which the interaction coefficients are empirically determined. Although the results are incouraging, this implementation is not considered here due to its highly parameterised nature.

Concerning depth-induced breaking, Herbers *et al.* (2000) demonstrate that, in the surf zone, a balance develops in the high-frequency region of the spectrum between energy added by nonlinear triad interaction and energy dissipated by depth-induced breaking. Therefore, to model the spectral shape correctly in these geographical regions, it is important to have an accurate representation not only of the average bulk dissipation (as given by the Battjes and Janssen (1978) model, for instance), but also its distribution in spectral space. Based on a flume investigation, Eldeberky and Battjes (1996) propose a spectral distribution of this bulk dissipation that is proportional to the local spectral density. This recommendation has been incorporated in the depth-breaking source term currently used in SWAN. By contrast, based on laboratory observations and numerical simulation, Mase and Kirby (1992) suggest that the dissipation rate is proportional to the local energy density

weighted by the square of its frequency. This finding is supported by Chen *et al.* (1997) who conclude that, although simulated variance spectra are fairly insensitive to the choice of frequency-weighting, a frequency-square weighting greatly improves the reproduction of the higher-order statistics of skewness and asymmetry. Consequently, recent stochastic surf-zone models that include the computation of these higher-order statistics have incorporated frequency-squared dissipation weighting (Herbers et al. 2003, Janssen 2006). Thus, frequency-weighting of dissipation needs to be taken into account when considering such triad interaction models with a view to the replacement of the LTA in SWAN.

A final issue concerns the interaction between the shallow water source terms, the deep water source terms and the limiter. As mentioned above, SWAN is based on an extension of the WAM model toward the surf zone. The processes modelled in the WAM model, particularly those of quadruplet interaction, assume deep or intermediate water conditions in which the wave field is homogenous and the water surface displacement is Gaussian. However, it can readily be seen from the higher-order statistics of observations taken in the surf zone (e.g. Herbers and Burton 1997), that the wave field significantly departs from Gaussianity here. Zakharov (1999) shows that quadruplet interaction theoretically ceases in shallow water when the condition $(ak)^2 << (kd)^5$, where a is the amplitude, is no longer met. Based on such considerations, Schneggenburger *et al.* (2000), for example, proposed a nearshore spectral wave model in which quadruplet interaction is omitted altogether, the flux of variance density being obtained by means of a nonlinear dissipation function instead. As discussed in Chapter 3, in earlier versions of SWAN quadruplet interaction (together with the action limiter) was switched off when triad interaction was activated. This choice was made because it was believed that the action limiter (which is required for the stable computation of quadruplet interaction) affects the accuracy of model results in the surf zone (Haagsma and Otta 2001). Bottema (2001a) shows that this partial deactivation of quadruplet interaction and the action limiter can lead to poor iteration behaviour in some situations, so that in recent configurations of SWAN the processes of triad and quadruplet interaction remain active alongside each other, also in the surf zone. In Chapter 3 it was shown that the limiter does not significantly influence converged model results, so that it appears acceptable to keep quadruplet interaction (and the limiter) active in the surf zone. However, the acceptablity of this modelling choice from the point of view of physics has not been investigated yet, and is therefore considered here.

Considering the modelling uncertainties described above, the present investigation compares the performance of SWAN in the surf zone when using the LTA with that when using a state-of-the-art two-equation model for triad interaction. This comparison aims to highlight differences in model performance found by using a detailed triad expression in which considerably fewer approximations are made. Complementary aims are to assess the influence of frequency weighting of dissipation on predictions, and the performance of deep water source terms (in particular quadruplet interaction) through the surf zone, under the influence of triad interaction and depth-induced breaking. These results are to serve as a benchmark for further development of operationally-based triad modelling in SWAN.

The two-equation triad model selected for the comparison is the Stochastic Angular-spectrum Model of Janssen (2006), here used for the reduced case of prismatic bathymetry (SAM1D). This two-equation model was implemented as a sub-module into SWAN, providing the main program with triad interaction results based on a full computation of the bispectrum. It is stressed that the resulting combined model for three- and four-wave interaction is not arrived at by means of a unified theoretical derivation, but by the combination of two independently derived source term expressions in the action balance equation. This is analogous to the approach followed with the LTA in the default model.

The SAM1D model for triad interaction is combined with a model for depth-induced breaking which features frequency weighting of the spectral distribution of the bulk dissipation, which is based on that of Battjes and Janssen (1978). The resulting model is compared with the default surf zone physics of SWAN, namely the LTA and the Battjes and Janssen (1978) model applied without frequency weighting in the distribution of the bulk dissipation. These two variants are first evaluated for laboratory cases in the absence of deep water source terms, in which a number of sensitivities are considered. The performance of the combined SWAN-SAM model is additionally compared to the results of the standalone SAM1D model, in order to verify its implementation in SWAN. Subsequently, the two model variants are evaluated for a field case featuring the evolution of a wind sea condition from outside the surf zone to the shore. Here the performance of the two model variants is compared in combination with bottom friction and the deep water source terms (wind input, whitecapping, quadruplet interaction). In these tests the interdependence of the various source terms, and the influence of the choice of deep water source term formulation, are studied.

This investigation shows that, after some calibration, the model version featuring the LTA is able to reproduce integral parameters adequately. However, the details of the underlying wave spectra are reproduced inaccurately. As has been reported previously, typical errors include the overestimation of the first harmonic and the absence of a second harmonic. By comparison, the model variant featuring the two-equation SAM1D model reproduces both the directionally-integrated spectra and their integral parameters well. The simulated directional spectra, however, display directional spreading that is less than observed values. In agreement with earlier studies, the best general performance was obtained with a model configuration featuring a frequency-squared distribution of dissipation and relaxation of the nonlinear couplings that is a function of both dissipation and the strength of the nonlinear transfer. In combination with deep water source terms, both investigated model variants display increased directional spreading, but unexpected model results are obtained within the surf zone. This appears to be due to the reaction of the deep water source terms, in particular quadruplet interaction, to the departure of the spectrum from its deep water (Gaussian) shape, in particular the shape of the high frequency tail. This reaction appears to be stronger in combination with the SAM1D triad model than with the LTA, since the former yields a greater transformation of the deep water spectrum in the surf zone.

This chapter is structured as follows: In Section 5.2 the LTA model is briefly presented and its performance in SWAN is evaluated on the basis of the laboratory experiments of Beji and Battjes (1993) and Boers (1996). In Section 5.3, an overview of the SAM1D model of Janssen (2006) is given, followed by a description of its incorporation as a sub-module into SWAN. The performance and accuracy of this implementation is checked by comparison with the experiments of Beji and Battjes and of Boers. Subsequently, in Section 5.4, the performance of the two model variants, when combined with deep water source terms, is evaluated for a field case of a wind sea incident on a barred beach. Section 5.5 closes with a discussion and conclusions.

5.2   Current modelling of triad interactions

5.2.1   The LTA model and current implementation

Nonlinear triad interactions are currently modelled in SWAN using the one-equation LTA model of Eldeberky (1996) for the spectral evolution of a uni-directional wave field. The derivation of the LTA, detailed in Eldeberky (1996), has the following features: The stochastic model is based on the Boussinesq type deterministic equations of Madsen and Sørensen (1993), and is truncated by a zero-fourth-order-cumulant assumption. The bispectrum arising from the ensemble averaging, which is a complex quantity, is split up into a biamplitude and a biphase. The biphase corresponding to the interaction of the spectral peak frequency σ_p with itself (self interaction) is parameterised as a function of the local Ursell number by

$$\beta(\sigma_p, \sigma_p) = -\frac{\pi}{2} + \frac{\pi}{2} \tanh\left(\frac{0.2}{Ur}\right) \tag{5.1}$$

.in which the spectrally-based Ursell number Ur is computed as

$$Ur = \frac{g}{8\sqrt{2}\pi^2} \frac{H_{m0} T_{m01}{}^2}{d^2} \ . \tag{5.2}$$

The biamplitude is obtained by spatially integrating the evolution equation for the bispectrum, by which the biamplitude is rendered a spatially local function. This results in an expression for the biamplitude which has a spatially slowly-varying component and a fast-oscillating component, of which the latter is neglected. Using the derived expressions for the biphase and biamplitude, the spectral evolution equation (a one-equation model) can be solved. To reduce the computational cost even further, the complete set of all interacting triads is represented by only the set of self sum interactions, that is, triads in which

a component of frequency σ interacts with a component of the same frequency to exchange energy flux with a component of frequency $\sigma + \sigma = 2\sigma$. The final expression for the effect of triad interactions on a component with frequency σ is made up of two contributions—one adding energy flux to σ (transferred flux arriving from $\sigma/2$) and one subtracting energy flux from σ (transfer going to 2σ). The expression implemented in SWAN, adapted for radian frequencies, reads:

$$S_{\text{nl3}}(\sigma, \theta) = S_{\text{nl3}}^-(\sigma, \theta) + S_{\text{nl3}}^+(\sigma, \theta) \tag{5.3}$$

with

$$S_{\text{nl3}}^+(\sigma, \theta) = \max[0, \alpha_{\text{EB}} 2\pi cc_g J^2 |\sin\beta| \left\{ E^2(\sigma/2, \theta) - 2E(\sigma/2, \theta)E(\sigma, \theta) \right\}] \tag{5.4}$$

and

$$S_{\text{nl3}}^-(\sigma, \theta) = -2S_{\text{nl3}}^+(2\sigma, \theta) \ . \tag{5.5}$$

Because of a Jacobian in the transfer of the energy flux from σ to 2σ, the flux density arriving at 2σ is half that leaving σ (hence the factor 2 appearing in (5.5)). The interaction coefficient J, describing self interaction in the nonlinearity range $0 \leq Ur \leq 1$, is given by (Madsen and Sørensen 1993):

$$J = \frac{k_{\sigma/2}^2(gd + 2c_{\sigma/2}^2)}{k_\sigma d(gd + \frac{2}{15}gd^3 k_\sigma^2 - \frac{2}{5}\sigma^2 d^2)} \ . \tag{5.6}$$

Summarizing, triad interaction modelled by the LTA includes only collinear self sum interactions, for one-dimensional spectral evolution. Since only sum interaction is considered, only superharmonics are created. Furthermore, since only self interactions are included, only the first, third, etc. superharmonics are reproduced. Because of the parameterization of the bispectrum, nonlinear transfer of energy occurs only in one direction through the spectrum, excluding the phenomenon of recurrence (reversal of energy transfer back to the spectral peak, which is observed e.g. over the downslope of submerged bars). Finally, as pointed out by Becq-Girard *et al.* (1999), by (5.5) the assumption is made that energy is conserved during the triad interaction, and in the LTA it is considered that

$$\int_{\sigma=0}^\infty \frac{d\left(E(\sigma)c_g^{\text{lin}}(\sigma)\right)}{dx} d\sigma = 0 \ . \tag{5.7}$$

In the action balance equation of SWAN, all waves are assumed to be free and to propagate with the linear group velocity c_g^{lin} which, for bound superharmonics, is always lower than

their actual velocity in nature c_g^{bound}. Therefore, by assuming the conservation of energy in the LTA, the variance density $E(2\sigma)$ is overestimated. Considering all interactions across the spectrum, the result is an artificial gain in energy, referred to here as artificial shoaling.

The LTA formulation was implemented in SWAN along each propagation direction of the directional spectrum, yielding an isotropic, directionally decoupled representation of triad interaction (Booij et al. 1999). The value of the proportionality coefficient of the LTA was fine-tuned in two successive studies: Booij et al. (1999) set its value at $\alpha_{\text{EB}} = 0.25$, based on comparison to the laboratory experiment of Beji and Battjes (1993). Subsequently, after reconsidering settings of the action density limiter and convergence criteria in the surf zone, Holthuijsen et al. (1999) recalibrated the coefficient to its current default value of $\alpha_{\text{EB}} = 0.1$. The results produced by the LTA are quite sensitive to the choice of the frequency up to which the interactions are calculated, denoted here as $f_{max,EB}$. Eldeberky (1995) recommends that the interactions be computed up to a frequency of 2.5 times the mean frequency $(f_{max,EB} = 2.5 f_{m01})$, and this setting was adopted in earlier versions of SWAN. However, this high-frequency limit was lowered to $f_{max,EB} = 2.2 f_{m01}$ by Holthuijsen et al. (1999) in conjunction with the recalibration of α_{EB} to 0.1. The effect of this change is one of the topics investigated below.

5.2.2 Performance of the LTA

The performance of the LTA has been investigated by Eldeberky (1996), Rasmussen (1998), Becq-Girard et al. (1999) and, in its current implementation in SWAN, by Booij et al. (1999). These investigators report adequate performance of the LTA over sloping beaches, considering integral parameters. However, simulated wave spectra show some shortcomings, such as inaccurate levels of the first superharmonic and the absence of subharmonics. In situations without dissipation, such as wave propagation over a submerged bar without breaking, Becq-Girard et al. (1999) show that the LTA causes spurious 'shoaling' of variance density. It is also known that, due to simplification during its derivation, the LTA does not simulate recurrence at the lee of submerged obstacles. To provide a benchmark of the performance of the LTA in SWAN and to investigate some sensitivities for the settings of its implementation, a comparison is presented here between simulations and observations for two laboratory experiments, namely that of Beji and Battjes (1993) and that of Boers (1996).

Firstly, the set of laboratory flume experiments of Beji and Battjes (1993) is considered, from which a case with strong nonlinearity but negligible dissipation is selected. This experiment features a submerged bar placed in a flume of 37.7 m length, 0.8 m width and 0.4 m depth (Figure 5.1). The bar has an upslope of 1:20, a horizontal section over which the a minimum depth of 0.1 m is reached and a downslope of 1:10. An array of seven gauges was used to measure the wave conditions along the flume. The case considered features a JONSWAP spectrum with $H_{m0} = 2.3$ cm and $f_p = 0.5$ Hz, generated at the wave maker.
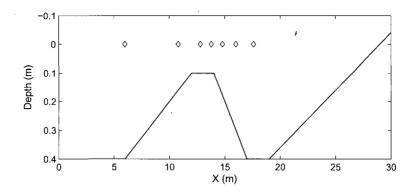
Figure 5.1: Setup of the Beji and Battjes (1993) flume experiment, showing the bottom profile and wave guage positions (diamonds).

The observations show that as waves run over the bar bound sub- and superharmonics are created in the spectrum (Figure 5.2). Over the downslope (e.g. at $x = 17.6$ m), some energy is returned from the spectral tail to lower frequencies (notably the first harmonic) during recurrence. This case was simulated using a discretisation in geographical space of $\Delta x = 0.1$ m, a fine directional discretisation of $\Delta\theta = 0.5°$ spanning a semi-circle (to capture the long-crested nature of the wave field in the flume) and logarithmically distributed frequencies ($\Delta f/f = 0.1$), running from 0.01 to 2.5 Hz. The only source terms active were triad interaction and depth-induced breaking. The latter, however, had negligible effect on the results.

Figure 5.2 shows the spectra simulated using the LTA, where two different model configurations are investigated: (a) with the proportionality coefficient $\alpha_{EB} = 0.1$ and the high-frequency cut-off at $f_{max,EB} = 2.2f_{m01}$ (the current default), and (b) with $\alpha_{EB} = 0.1$ and $f_{max,EB} = 2.5f_{m01}$. Figure 5.2 shows that for model variant (a) energy levels at the first superharmonic are generally overestimated over the horizontal section of the bar, and that the position of this harmonic in frequency space is somewhat inaccurate. Moving over the downslope into deeper water, triad interaction computed by the LTA vanishes, although the observed first superharmonic increases due to recurrence. As a result, but only by coincidence, the agreement between the model and observations at the lee of the bar is good. No energy is transferred to sub-harmonic frequencies. Due to the high-frequency limit $f_{max,EB}$ imposed on the interaction calculation, no energy is transferred to the region beyond $3.5f_p$, so that energy levels in the tail is underestimated at most stations. When this limit is relaxed in variant (b), the energy level at the first harmonic decreases, improving the agreement with observations over the horizontal section of the bar. However, energy in the tail is now overestimated by the formation of a third superharmonic in the model. Over the downslope, the observed energy levels at higher frequencies reduce due to
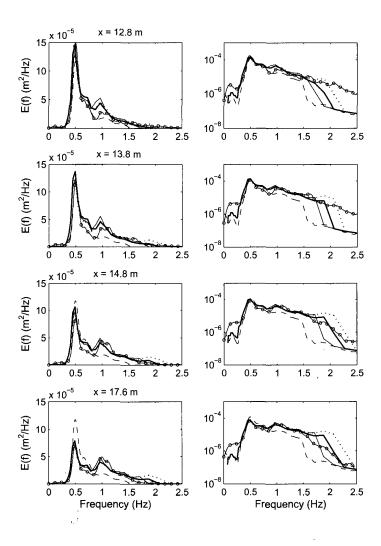
Figure 5.2: Comparison between spectra produced using the LTA and laboratory observations of Beji and Battjes (1993) at various locations, on linear (left-hand side) and logarithmic (right-hand side) axes. Spectra simulated with parameter combinations (a) $\alpha_{EB} = 0.1$ and $f_{max,EB} = 2.2f_{m01}$ (thin solid line), (b) $\alpha_{EB} = 0.1$ and $f_{max,EB} = 2.5f_{m01}$ (dotted line) and (c) $\alpha_{EB} = 0.05$ and $f_{max,EB} = 2.5f_{m01}$ (thick solid line) are shown. Observations indicated by line with circles; observed spectrum at $x = 6.0$ m (boundary value) indicated by dashed line.
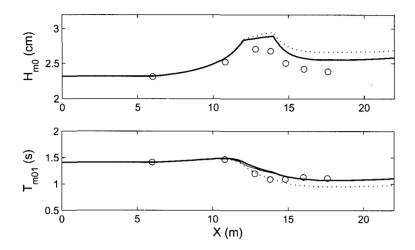
Figure 5.3: Comparison between significant wave height and mean period produced using the LTA and laboratory observations of Beji and Battjes (1993). Simulation results with parameter combinations (a) $\alpha_{EB} = 0.1$ and $f_{max,EB} = 2.2f_{m01}$ (thin solid line), (b) $\alpha_{EB} = 0.1$ and $f_{max,EB} = 2.5f_{m01}$ (dotted line) and (c) $\alpha_{EB} = 0.05$ and $f_{max,EB} = 2.5f_{m01}$ (thick solid line) are shown. Observations are indicated by circles.

recurrence. Since this does not happen in the model, it leaves the tail greatly overestimated in model variant (b).

Figure 5.3 compares the simulated and observed significant wave height and mean period, obtained by integrating the observed and simulated spectra over the frequency range of 0.01 to 2.5 Hz. It is noted that for the simulated spectra this means that the parametric tail, which is usually added in the calculation of integral parameters, was omitted[1]. In the model results, the growth of significant wave height is slightly overestimated over the upslope. As waves propagate over the horizontal section the significant wave height continues to grow, contrary to what is found in the observations. This has been shown by Becq-Girard et al. (1999) to be due to the fact that linear flux is conserved by the LTA, as discussed in Section 5.2.1 above. This effect is the strongest for model variant (b), which transfers the most energy to the higher frequencies. Behind the bar, the significant wave height is also overestimated by the model, since no energy is returned to lower frequencies by recurrence. Considering the mean period, model variant (b), with the cut-off frequency

---

[1]In shallow water, where the diagnostic tail gains significant levels of energy, adding the parametric tail has a significant impact on integral parameters, making a comparison to observations integrated over a finite frequency range unfair. In deep water, where energy levels in the diagnostic tail are generally low, integral parameters are far less affected by the presence of the parametric tail.
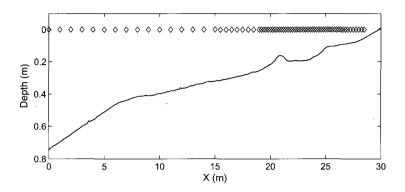
Figure 5.4: Setup of the Boers (1996) flume experiment, showing the depth profile of a barred beach and the wave guage positions (diamonds).

at $2.5f_{m01}$, agrees well with the observations up to the end of the horizontal section, but underestimates the observations thereafter. Variant (a) produces a good average fit through the observations. This is due to the fact that no energy is transfered to frequencies beyond $3f_p$, avoiding an overestimation of the tail.

The second case considered is the laboratory flume experiment of Boers (1996) which features a barred beach over which both depth-induced breaking and triad interaction takes place. Figure 5.4 presents the flume, having a length of 40 m, a width of 0.80 m and featuring a barred beach profile. Waves were measured along the length of the flume by an array of wave guages. Here the wave condition 1A from Boers (1996) is considered, which features a JONSWAP-type spectrum with parameters $H_{m0} = 0.16$ m and $T_p = 2.1$ s generated at the wavemaker. This wave field is energetic and has a relatively high mean steepness, and at the boundary already has a significant amount of energy present at the first superharmonic. Figure 5.5 shows that as waves proceed down the flume a significant amount of energy is present in the first superharmonic, but gradually decreases, along with the peak, due to depth-induced breaking. Similarly, energy levels at higher frequencies increase as the waves proceed towards the shore, but decrease beyond the bar due to breaking dissipation. At the upwave boundary energy at the subharmonic frequencies is small, but increases steadily throughout the flume due to difference triad interaction. By $x = 26$ m energy levels below the peak even surpass that of the peak, and, as a result, observations beyond this point are not considered here.

This case was simulated with the two settings of the LTA presented above (variants (a) and (b)). Depth-induced breaking was modelled using the expression of Battjes and Janssen (1978), with the default setting of $\alpha_{BJ} = 1.0$ and $\gamma_{BJ} = 0.73$. The discretisation in geographical space is $\Delta x = 0.1$ m, in directional space $\Delta\theta = 0.5°$ (spanning a semi-circle)
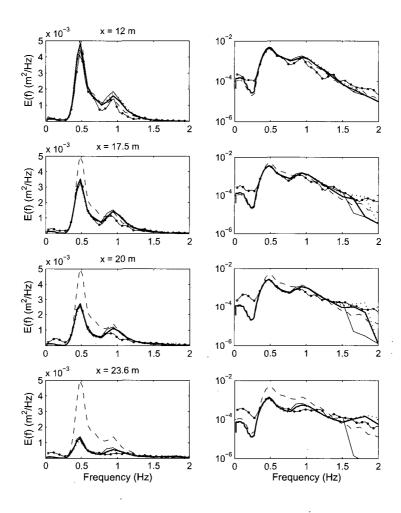
Figure 5.5: Comparison between spectra produced using the LTA and laboratory observations of Boers (1996) (Case 1A), on linear (left-hand side) and logarithmic (right-hand side) axes. Spectra simulated with parameter combinations (a) $\alpha_{EB} = 0.1$ and $f_{max,EB} = 2.2f_{m01}$ (thin solid line), (b) $\alpha_{EB} = 0.1$ and $f_{max,EB} = 2.5f_{m01}$ (dotted line) and (c) $\alpha_{EB} = 0.05$ and $f_{max,EB} = 2.5f_{m01}$ (thick solid line) are shown. Observations indicated by line with circles; observed spectrum at the boundary indicated by dashed line.
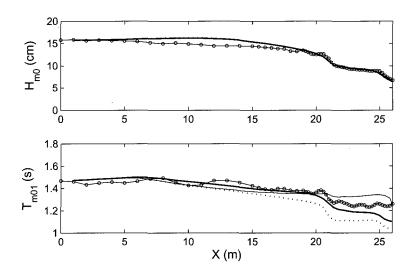
Figure 5.6: Comparison between wave height and mean period produced using the LTA and laboratory observations of Boers (1996) (Case 1A). Simulation results with parameter combinations (a) $\alpha_{EB} = 0.1$ and $f_{max,EB} = 2.2f_{m01}$ (thin solid line), (b) $\alpha_{EB} = 0.1$ and $f_{max,EB} = 2.5f_{m01}$ (dotted line) and (c) $\alpha_{EB} = 0.05$ and $f_{max,EB} = 2.5f_{m01}$ (thick solid line) are shown. Observations are indicated by line with circles.

and in frequency space logarithmically distributed ($\Delta f/f = 0.1$), running from 0.01 to 2.0 Hz. Figure 5.5 presents the spectra simulated by these model variants. Variant (b) gives a reasonable reproduction of the nearshore spectral evolution, although the energy levels at the first superharmonic are generally overestimated, and the steady growth in the energy levels of the subharmonic frequencies is not reproduced. By comparison, variant (a) underestimates the energy levels beyond $3f_p$, due to the low value of $f_{max,EB}$. Also, because the energy flux to higher frequencies is limited, energy levels at the first harmonic are overestimated somewhat more than with variant (b). Figure 5.6 presents the corresponding integral parameters, obtained by integration over the frequency range 0.25 to 2.0 Hz. Significant wave height is somewhat overestimated offshore of the bar, presumably due to inaccurate shoaling or insufficient dissipation, but wave height results agree well with the observations shoreward of the bar. Within the surf zone, depth-induced breaking is therefore evidently strong enough to compensate for the effects of the artificial shoaling that was observed in the case considered above. The mean wave period, on the other hand, is reproduced less well. Model variant (a), which underpredicts the higher frequencies of the spectrum, yields a fair result up to the bar, but overestimates the mean period beyond it. By comparison, variant (b) underestimates the mean period throughout most the flume.

From the simulation results of the laboratory cases of Beji and Battjes (1993) and Boers (1996) it can be concluded that the LTA, as currently implemented in SWAN, yields a reasonable reproduction of the main effects of triad interaction, but can lead to notable inaccuracies in both integral parameters and spectra. These results are influenced by the choice of the high-frequency cut-off $f_{max,EB}$, which affects both the spectra and mean period measures. The high-frequency cut-off is a means of limiting the inaccuracy of the LTA at higher frequencies, and it may therefore be considered a tuning parameter alongside the proportionality coefficient α_{EB}. The setting $\alpha_{EB} = 0.1$ and $f_{max,EB} = 2.2 f_{m01}$ appears to give a generally satisfactory result in terms of H_{m0} and T_{m01}. However, details of the spectra are badly reproduced: the first harmonic is overestimated and the spectral tail is underestimated. An alternative is to set $f_{max,EB} = 2.5 f_{m01}$, for which the spectral shape is better reproduced and recalibrate α_{EB} to obtain an improved fit to integral parameters, especially of the period measures of the Boers (1996) case. Based on the two generic cases considered here, a setting of $\alpha_{EB} = 0.05$ with $f_{max,EB} = 2.5 f_{m01}$ is deemed to yield acceptable results for both spectra and integral parameters (results added to Figures 5.2–5.6). This setting is used in the comparisons presented in the following sections.

5.3 Combined SWAN-SAM model

In the previous section, the performance of the LTA, the default expression for triad interaction in SWAN, was reviewed. To investigate the effect of replacing this highly parameterized expression with a theoretically more complete (but computationally more intensive) formulation, this section describes the implementation and evaluation of the SAM1D model in SWAN. In addition to the more detailed description of triad interaction, the SAM1D model also embodies a depth-induced breaking expression that features frequency-dependent distribution of dissipation. Below, an overview is given of the characteristics of SAM1D, its implementation as a sub-module into SWAN and a verification of the resulting combined model.

5.3.1 The SAM1D model

Janssen (2006) derived a two-equation stochastic wave model that describes the spatial evolution of both the spectrum and the bispectrum over quasi two-dimensional topography, that is, topography with free variation in one horizontal Cartesian dimension and weak variation perpendicular to it. In this study we consider a reduced version of this model, called SAM1D, that models spectral evolution of a directional wave field over topography that is limited to one-dimensional (prismatic) variation. Following Herbers and Burton (1997) and Herbers *et al.* (2003), a fully isotropic spectral representation of the wave field (such as used in SWAN) is discarded in favour of a so-called multi-frequency angular-

spectrum decomposition—a representation on a half plane featuring a primary spatial propagation direction with directional spreading away from this primary direction. This spectral space $E(\sigma, \lambda)$ is spanned by the radial frequency σ and a longshore wave number λ, and is related to the spectral definition of SWAN via the following Jacobian transformation (Herbers *et al.* 2003):[2]

$$E(\sigma, \lambda) = \frac{E(\sigma, \theta)}{2k \cos(\theta)} \tag{5.8}$$

The reason for applying such a non-isotropic representation is that, unlike the evolution of the spectrum and its source terms, an isotropic evolution equation for the higher-order correlations (such as the bispectrum) is unavailable at present (Janssen 2006).

The SAM1D stochastic model is obtained using the procedure of ensemble averaging of a deterministic model describing the underlying wave dynamics (e.g. Herbers and Burton 1997). For SAM1D, a deterministic spectral description is used, which features no limits to linear dispersion. The hierarchy of equations is truncated at the equation for the spatial evolution of the bispectrum, using a heuristic closure hypothesis, in analogy to Herbers *et al.* (2003), that relaxes the wave field to a Gaussian state (zero skewness and asymmetry) in areas with breaking dissipation and strong nonlinearity. The resulting hierarchy of equations, which describes the spatial evolution of a directional wave spectrum over one-dimensional topography, is (Janssen 2006):

$$\frac{d\xi_1^1}{dx} = -D_1 \xi_1^1 - 2 \sum_{v2} W_{(1-2)2}^{(1-2)2} \mathrm{Im} \left[C_{(1-2)2}^{(1-2)2} \right] \Delta\sigma\Delta\lambda \tag{5.9}$$

$$\begin{aligned}
\frac{dC_{12}^{12}}{dx} &= i \left(\Lambda_{12}^{12} + i\mu_{12}^{12} \right) C_{12}^{12} - \frac{1}{2} \left(D_1 + D_2 + D_{(1+2)} \right) C_{12}^{12} \\
&+ 2i \left[W_{(1+2)(-2)}^{(1+2)(-2)} \xi_2^2 \xi_{(1+2)}^{(1+2)} + W_{(1+2)(-1)}^{(1+2)(-1)} \xi_1^1 \xi_{(1+2)}^{(1+2)} + W_{12}^{12} \xi_1^1 \xi_2^2 \right]
\end{aligned} \tag{5.10}$$

in which ξ_σ^λ is the flux spectrum defined as

$$\xi_i^j(x) = c_g^{\mathrm{lin}}(\sigma_i, x) E(\sigma_i, \lambda_j, x) \tag{5.11}$$

and $C_{\sigma,\sigma}^{\lambda,\lambda}$ the bispectrum defined as

---

[2]Other characteristics of the angular-spectrum decomposition are that it requires many more (σ, λ) bins than an isotropic (σ, θ) description to span a spectral space with similar accuracy, and that the use of a finite range of λ components can result in an aperture limitation on incoming wave directions for a particular component frequency at a given depth.

$$C_{ij}^{ij}(x) = C(\sigma_i, \sigma_j, \lambda_i, \lambda_j, x). \tag{5.12}$$

The notation followed here is that variables in the subscripts refer to radian frequency components σ and those in the superscripts to longshore wavenumber components λ. In this model, the linear group velocity c_g^{lin} is applied to simplify the system of equations. However, as will be shown below, energy is not conserved during the triad interaction, so that the spurious 'shoaling' observed with the LTA does not occur. Quantity $W_{\sigma,\sigma}^{\lambda,\lambda}$ is the coupling coefficient describing the strength of the triad interaction, $\Lambda_{\sigma,\sigma}^{\lambda,\lambda}$ the phase mismatch between components, leading to stronger interaction as the mismatch reduces. Quanties D_σ and $\mu_{\sigma,\sigma}^{\lambda,\lambda}$ are the dissipation due to depth-induced breaking and the relaxation term respectively, which are detailed below.

Equation (5.9) describes the spatial evolution of the flux spectrum, including linear shoaling, refraction, depth-induced breaking and triad interaction (wave-current interaction is not included). Equation (5.10) describes the spatial evolution of the bispectrum. This system of equations is linked via the third-order cumulant of the evolution equation of the flux spectrum (second term on the right-hand side of (5.9)), which is a function of the bispectrum. This third-order cumulant represents the effect of nonlinear triad interactions on the evolution of the flux spectrum. It is equivalent to S_{nl3} appearing in the action balance equation (2.3), and will be used in this study to model triad interaction in SWAN (Section 5.3.2). No further simplifications or parameterisations are applied to the triad interaction expression, so that the method is considerably more intensive than, for example, the LTA. In addition, the computation of the bispectrum requires the use of a small spatial step.

The relaxation term $\mu_{\sigma,\sigma}^{\lambda,\lambda}$ in (5.10) is given by

$$\mu_{12}^{12} = \left[\frac{\beta_D |\chi_1^{(D)} + \chi_2^{(D)} + \chi_{(1+2)}^{(D)}| + \beta_{NL} |\chi_1^{(NL)} + \chi_2^{(NL)} + \chi_{(1+2)}^{(NL)}|}{\xi_1^1 + \xi_2^2 + \xi_{(1+2)}^{(1+2)}} \right] \tag{5.13}$$

in which

$$\chi_i^{(D)} = -D_i \xi_i^i \qquad \text{and} \qquad \chi_i^{(NL)} = -2 \sum_{v2} W_{(i-j)j}^{(i-j)j} C_{(i-j)j}^{(i-j)j} \Delta\sigma \Delta\lambda. \tag{5.14}$$

The speed of relaxation towards a Gaussian state increases with the coefficients β_D and β_{NL}. The coefficient β_D determines how much relaxation depends on the strength of the dissipation of the three components of the triad, and β_{NL} how much it depends on the strength of the nonlinear interaction with the background wave field. For $\beta_D = \beta_{NL} = 0$ quasi-normal closure is obtained. For $\beta_D > 0$ and $\beta_{NL} > 0$ nonlinear couplings are damped,

so that energy exchange within the triad is weaker, leading to smaller skewness and asymmetry. Equation (5.13) applied here is an adaptation of that used by Janssen (2006), in which a single $\beta = \beta_D = \beta_{NL}$ is used.

The expression for depth-induced breaking, D_σ, is given by the CRAD breaker model (Janssen 2006), which is based on the model of Battjes and Janssen (1978) as adapted by Baldock *et al.* (1998). Like the model of Baldock *et al.* (1998), the CRAD model uses the full (non-truncated) Rayleigh distribution to determine the fraction of breaking waves. This results in the following explicit expression for the average bulk dissipation D (Janssen 2006):

$$D = \frac{2\alpha_{CR}}{\pi} \frac{m_1}{h} \sqrt{2m_0} \left[\left(H_r^{\,3} + \frac{3}{2} H_r \right) \exp[-H_r^{\,2}] + \frac{3}{4}\sqrt{\pi}\,(1 - \mathrm{erf}(H_r)) \right] \tag{5.15}$$

in which α_{CR} is a proportionality coefficient. The spectral moments m_n are calculated in the angular-frequency domain as

$$m_n(x,y) = \iint |\sigma_1|^n E_1^1(\sigma, \lambda, x, y)\, d\lambda_1 d\sigma_1 \;. \tag{5.16}$$

The reference wave height is defined as $H_r = H_b/H_{rms}$, in which H_{rms} is the root-mean-square wave height, $H_b = \gamma_{CR} d$ is the breaking wave height and γ_{CR} the breaking criterion coefficient. The average bulk dissipation D produced by the CRAD model is generally similar to that computed by the Battjes and Janssen (1978) model over gentle slopes (in the order of 1:100) found in typical field conditions, but results differ for unsaturated surf zone conditions on very steep slopes (Janssen 2006). In terms of the distribution of the bulk dissipation D in the frequency space, the CRAD model differs from the application of the Battjes and Janssen model in SWAN. Based on the findings of Kaihatu and Kirby (1995) and Chen *et al.* (1997), the dissipation D calculated by CRAD is not distributed proportional to the variance density only, but has a contribution that is weighted by the frequency squared, yielding the following expression for the dissipation factor D_σ appearing in (5.9), (5.10) and (5.14):

$$D_i = \frac{1}{\tilde{m}_0} \left(r_0 + r_2 \sigma_i^2 \frac{\tilde{m}_0}{\tilde{m}_2} \right) D, \tag{5.17}$$

in which the spectral flux moments $\tilde{m}_n$ are calculated in the angular-frequency domain as

$$\tilde{m}_n(x,y) = \iint |\sigma_1|^n \xi_1^1(\sigma, \lambda, x, y)\, d\lambda_1 d\sigma_1 \;. \tag{5.18}$$

Quantity r_0 determines the fraction of uniform weighting and r_2 the fraction of weighting proportional to the frequency squared ($\sum_n r_n = 1$). Chen *et al.* (1997) find that weighting dissipation with the square of the frequency has little effect on the prediction of the spectrum (since dissipation is balanced at high frequencies by triad interaction) but that it improves the estimation of the higher-order statistics of skewness and asymmetry considerably.

In summary, the distinguishing features of the SAM1D model are the following: Because of the choice of full-dispersion deterministic equations, resonant and near-resonant triad interactions are modelled exactly, and there is no limitation to linear dispersion towards greater dimensionless water depth. The stochastic model includes the propagation of a directional spectrum over a one-dimensional topography, and the closure hypothesis of the fourth-order cumulant forces a return to a Gaussian state in the surf zone (where nonlinearity and dissipation are strong). Since both the spectral and the bispectral evolutions are computed, and all interactions are included, SAM1D is computationally intensive.

5.3.2 Implementation in SWAN

In considering the implementation of SAM1D in SWAN, there are a number of differences between the two models that need to be reconciled: Considering the computational domains, in it most general configuration, SWAN is defined over topography that varies over two horizontal dimensions, whereas SAM1D is defined for one-dimensional variation in topography (parallel contours) only. In spectral space, the propagation of spectral components in SWAN is isotropic, whereas, for the reasons given above, SAM1D is defined on a semi-circle of directions about a dominant propagation direction. Considering the primary equation solved, SWAN computes only the variance density spectrum (all higher order moments are parameterized in the nonlinear source terms or neglected), whereas in SAM1D both the variance density spectrum (embodied in the flux spectrum) and the bispectrum are solved. In terms of numerics, SWAN solves the action balance equation using an implicit four-sweep scheme, which is solved by means of iteration. SAM1D, by contrast, solves its complete spectral computational domain at each geographical grid point during a single geographical space stepping procedure, without iteration. Finally, because of the physics modelled, specifically to capture short length scale variations in the bispectrum, SAM1D requires a much finer geographical resolution than SWAN. These differences are addressed below.

The first consideration regards the combination of the computational domains of the two models. Since the SAM1D model computes triad interactions as directionally coupled (with no assumption of co-linearity as with the LTA), and also because of the unresolved issues surrounding the directional propagation of the bispectrum, an isotropic extension of SAM1D (analogous to the approach used with the LTA) is not pursued. As a result, the combination of SWAN and SAM1D developed in this study is subject to the same

SWAN, SWEEP 1

SWAN, SWEEP 4

SAM1D

SHORELINE
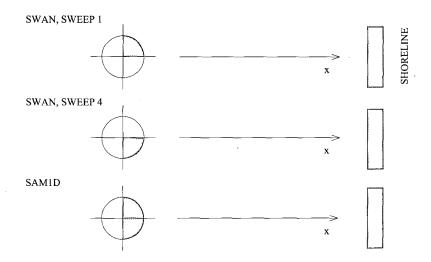
Figure 5.7: Diagram of the propagation directions in geographical space for the combination model of SWAN and SAM1D. Shown are the directional quadrants of sweeps 1 and 4 in SWAN that exchange information with SAM1D (shaded areas, refer Figure 2.1), and the semi-circle of directions that is solved during one spatial step in SAM1D.

restrictions to geographical domain as SAM1D: the combined model simulates directional wave spectra over one-dimensional topography. Such a model will therefore not be suited to the modelling of shallow areas such as tidal inlets with strong two-dimensional topography, but may find application along open coasts which often have nearly one-dimensional topography in the nearshore. For such open coast situations, the resulting model will be a means of investigating the impact of including state-of-the-art triad modelling into SWAN, to serve as a benchmark for further development.

The next consideration regards the wave field variables to be solved and the solution method to apply. In this study we do not pursue a unified theoretical derivation of three and four wave interaction. Rather, an approach is followed which is analogous to that followed with the LTA in the default version of SWAN. The nonlinear shallow water physics (including the evolution of the bispectrum) is represented in the action balance equation of SWAN by the third-order cumulant term computed by SAM1D. That is, in the action balance equation we set the triad source term equal to:

$$S_{nl3}(\sigma_1, \theta_1) = -2 \sum_{v2} W_{(1-2)2}^{(1-2)2} C_{(1-2)2}^{(1-2)2} \Delta\sigma \Delta\lambda \tag{5.19}$$

in which the cumulant term on the right-hand side is computed in (5.9). For the calculation

of the triad source term with the SAM1D model, it is required to solve the bispectrum simultaneously with the variance density spectrum. This is achieved by running SAM1D as a sub-module parallel to SWAN, solving the evolution of the bispectra and passing back the computed triad interaction results.

The incorporation of SAM1D in the iterating, implicit four-sweep numerical scheme of SWAN is achieved with the following algorithm: The geographical x axes of both SWAN (in one-dimensional mode) and that of SAM1D are directed perpendicularly toward the shoreline (Figure 5.7). This means that only the directional components of sweeps 1 and 4 of SWAN run toward to shore, and that these agree with the semi-circle of directions included in the spectral domain of SAM1D. For each iteration, during sweep 1, SWAN steps through the geographical space along the x axis from deep water up to a grid point in shallower water at which the wave field becomes sufficiently nonlinear for triad interaction to become relevant. The criterion for nonlinearity used here is a threshold value of the spectrally-based Ursell number given by (5.2). At this point the SAM1D sub-module is activated, initiating the coupled computation of the bispectrum. The bispectrum is initialized using second-order wave theory, producing a skewed but symmetrical Stokes wave field (Herbers and Burton 1997). From this point onwards, the following algorithm is repeated:

(a) During sweep 1, at the beginning of each spatial step in x, the wave spectrum that is computed in the action balance equation is passed from the SWAN main program to the SAM1D sub-module, where the bispectral evolution is computed for a single spatial step.

(b) Using the bispectrum at the end of the spatial step, the triad interaction term (5.19) is calculated for the complete semi-circle in the spectral domain of SAM1D, and passed back to the SWAN main program. Subsequently, SWAN calculates the remaining deep and shallow water source terms in the directional quadrant belonging to sweep 1, and finally solves the action balance equation for all source terms at the end of the spatial step. The program returns to step (1) for the next spatial increment in x, until the end of sweep 1 is reached (the shore).

(c) Sweeps 2 and 3 of SWAN are computed without the triad term (it is zero here).

(d) For sweep 4, a procedure similar to that of steps 1 and 2 is followed, but now for the fourth sweep. When the spatial stepping of the fourth quadrant has reached the shore the current iteration is concluded.

This procedure is repeated for every subsequent iteration. At every point where information is passed between SWAN to SAM1D the Jacobian transformation (5.8) is applied, which requires bilinear interpolation. Since the evolution of the bi-spectrum is computed in the combined model, the process of coupled spectral and bispectral computation has to be continued from the point at which the bispectrum is initialized up to the shore. This is in
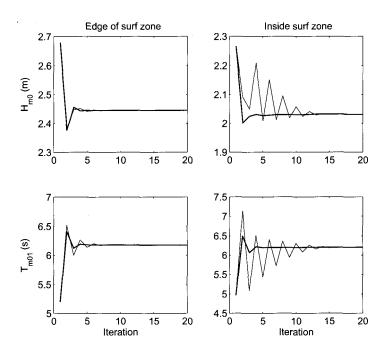
Figure 5.8: Comparison between the iteration behaviour of the combined SWAN-SAM model when computing triad interactions per sweep (thick line) and per iteration (thin line). Results for a bar beach field case at Duck, North Carolina, at the offshore edge of the surf zone (left-hand panels) and deep inside the surf zone (right-hand panels).

contrast to the procedure applied with the LTA, in which triad interaction is considered to be a function of local variables in geographical space only. As a result, in the combined SWAN-SAM model both the spectrum and bispectrum are available as output quantities, from which both the usual second-order statistics as well as third-order statistics (skewness and asymmetry) may be computed.

From the algorithm above, it is seen that the triad source term is computed per sweep. This means that the computationally expensive SAM1D model is called twice per iteration—in each sweep computing the total semi-circle of interactions (because of non-collinear interaction), of which only the quadrant relevant to the sweep is used in SWAN (Figure 5.7). The computational effort of the triad calculation could be reduced by about one half by computing the triad term explicitly—calling SAM1D only during sweep 1, and using the same computed triad interaction result in both sweeps 1 and 4. Figure 5.8 compares the iteration behaviour of these two implementations, namely triad computation per sweep and

triad computation per iteration, for a typical surf zone application. Outside the surf zone the iteration behaviour and convergence speeds of the two methods are comparable. Deep inside the surf zone, however, computing the triad source term per sweep yields much better iteration behaviour than the computation once per iteration, and converges about twice as fast. Thus the overall computational effort (computation per iteration times number of iterations) of these two approaches is comparable. However, considering its smoother iteration behaviour, preference is given to triad computation per sweep, as presented in the algorithm above.

5.3.3   Validation and calibration of combined two-equation model

In this section, the implementation of SAM1D into SWAN (hereafter referred to as the two-equation model) is validated using the laboratory experiments of Beji and Battjes (1993) and Boers (1996) introduced in Section 5.2.2. The objectives of this section are, firstly, to show that the combined two-equation model yields similar results for spectra and integral parameters as the standalone SAM1D model and, secondly, to determine appropriate settings for the calibration parameters of the expressions for nonlinear interaction (relaxation coefficients β_D and β_{NL}) and depth-induced breaking (α_{CR}, γ_{CR} and r_n).

Considering the standalone SAM1D model, Janssen (2006) shows that it reproduces directionally-integrated spectra and higher-order statistics well, certainly outside of the surf zone where the model is close to first principles. Invoking relaxation tends to yield spectra which are generally more spread out over frequencies, and in closer agreement with observations, than if no relaxation is used (quasi-normal closure). The model, including relaxation, does however have a tendency to reproduce spectra with less sharply defined harmonics than found in the observations. Higher-order statistics of skewness and asymmetry are typically reduced in amplitude when relaxation is invoked, reflecting the imposed progression towards Gaussianity. These statistics also agree well with observed values. Without conducting an extensive calibration of this model, Janssen (2006) finds that the parameter combination $\beta = \beta_D = \beta_{NL} = 1.5$, $\alpha_{CR} = 1.0$, $\gamma_{CR} = 0.85$ and $r_0 = 0.1$ produces good average performance of the model over cases representing a wide range of situations.

Firstly, the Beji and Battjes (1993) bar experiment presented above is considered, in which strong nonlinear interaction but negligible dissipation occurs. The discretisation applied in SWAN is the same as that used in Section 5.2.2 above. In the SAM1D sub-module, the frequency space up to 2.5 Hz is spanned by 60 equidistant frequency bins and the longshore wavenumber space is spanned by 101 equidistant wavenumber bins running between ± 1 rad/m. This directional discretization is sufficient to capture the long-crested nature of the wave field in the flume. For this model setup, computations took about 100 times longer than those of the LTA model. Initially, the results for weak relaxation ($\beta_D = \beta_{NL} = 0.1$) are evaluated. Figure 5.9 compares the simulation results of the combined two-equation model with those of the standalone SAM1D model and with observations. It is shown
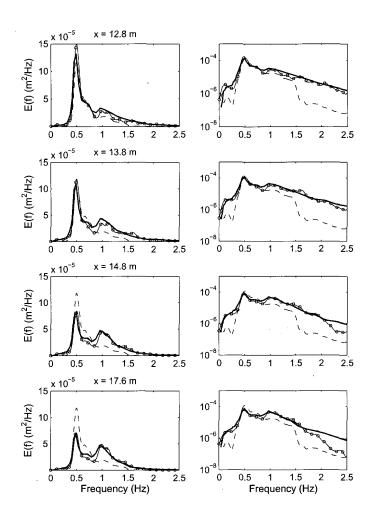
Figure 5.9: Comparison between spectra produced by the standalone SAM1D, the combined two-equation model and laboratory observations of Beji and Battjes (1993) at various locations. Panels on left-hand side are plotted on linear scales and those on the right-hand side on logarithmic axes. Results of the standalone SAM1D and the combined two-equation model (both with $\beta_D = \beta_{NL} = 0.1$) are represented by thin and thick solid lines respectively, but are indistinguishable at the present scale. Observations indicated by line with circles; observed spectrum at x = 6.0 m (boundary value) indicated by dashed line.
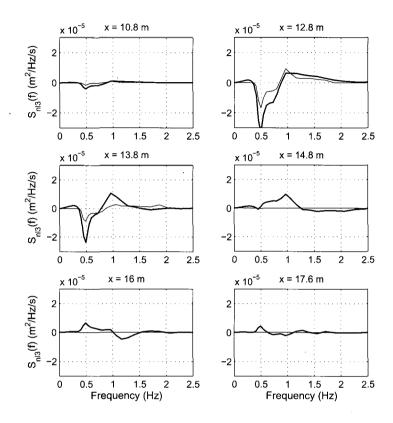
Figure 5.10: Comparison between the triad interaction computed by the combined two-equation model (thick line) and that produced by the LTA in the default model (thin line), at various locations over the Beji and Battjes (1993) bar. Vertical scale held constant to facilitate comparison.

that the agreement between the results of the two models is near-perfect, indicating that SAM1D has been correctly implemented in SWAN. Also, the agreement between the results of these two models collectively and the observations is generally very good. Over the upslope and the horizontal section of the bar, the generation of both the higher and lower harmonics is well reproduced by the models. However, behind the bar the models overestimate the amount of energy in the spectral tail. This overestimation points to an underestimation by SAM1D of the amount of energy returned to lower frequencies during the recurrence experienced on the downslope of the bar, as is also noted by Janssen (2006).
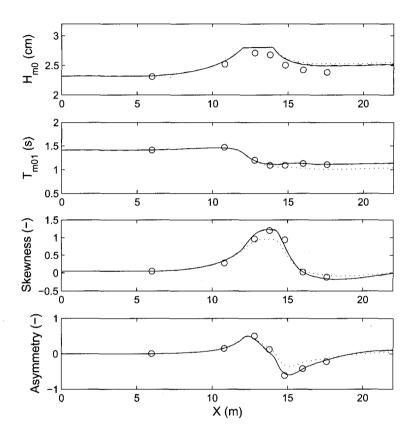
Figure 5.11: Comparison between integral parameters produced by the standalone SAM1D model, the combined two-equation model and observations of Beji and Battjes (1993). Results of the standalone SAM1D and the combined two-equation model (both with $\beta_D = \beta_{NL} = 0.1$) are represented by dashed and solid lines respectively, but are indistinguishable at the present scale. Results by the combined two-equation model with $\beta_{NL} = 1.5$ (dotted line) is included for comparison. Observations are indicated by circles.

Figure 5.10 presents the corresponding source term results produced by the combined two-equation model, and compares them with those produced using the LTA in the simulations presented in Section 5.2.2. The computed interaction of the combined two-equation model transports energy from the peak to higher and lower frequencies over the upslope and horizontal section of the bar. Over the downslope, this process is reversed. This is in contrast to the interaction computed by the LTA, which only includes transfer to higher frequencies, and for which the transfer goes to zero over the downslope due to the absence of recurrence. A striking feature of the comparison is that the interaction produced by the two-equation model is significantly stronger than that by the LTA. This is mainly because of the relatively low value chosen for the proportionality coefficient α_{EB}. A second important feature of the comparison is that the areas underneath the interaction lobes of the LTA are equal, whereas, in general, those of the combined model are not. As discussed in Section 5.2.1, the LTA conserves energy during the triad interaction, which causes an overestimation of the total variance if wave components are assumed to propagate with their linear group velocity. By contrast, energy is not conserved in the SAM1D triad source term, as can be seen in the unequal areas beneath the interaction lobes. This non-conservation compensates for the use of the linear group velocity in (5.9)-(5.12).

Figure 5.11 shows the integral parameters of wave height, mean period, skewness and asymmetry, produced by the combined two-equation model and the standalone SAM1D model. These are obtained by integration over a frequency range of 0.01 to 2.5 Hz. For all these output quantities the agreement between the results of the two models is excellent, indicating that the triad implementation performs well. Comparison between the results of the two models and the observations reveals that shoaling on the upslope appears somewhat too strong, yielding an overestimation of the significant wave height at the start of the horizontal bar section. Over the horizontal section, the significant wave height remains constant. This is in contrast to the results obtained with the LTA, in which energy is conserved during triad interactions (see Figure 5.3 in Section 5.2.2). However, over the downslope and behind the bar, the combined two-equation model, like the standalone SAM1D model, overestimates the wave height somewhat, because the underestimation of recurrence leaves too much energy in the tail. In terms of mean period and the higher-order statistics of skewness and asymmetry, the agreement between the models and the observations is very good.

Also presented in Figure 5.11 is the effect of increasing the relaxation coefficient β_{NL} in the SAM1D triad formulation. (A similar comparison is presented by Janssen (2006) for the standalone SAM1D model.) By increasing the relaxation as function of nonlinearity to $\beta_{NL} = 1.5$, the overall magnitude of skewness and asymmetry decreases, indicating that the strength of the nonlinear coupling is weakend. The impact of this is also seen in the mean period, which does not increase as strongly over the downslope of the bar during the recurrence stage. The influence of relaxation is not large here, although the correspondence between integral model results and observations generally deteriorates somewhat with the application of this setting.

Next, the laboratory experiment of Boers (1996) is considered, in which the combined performance of triad interaction and depth-induced breaking is evaluated. The discretisation applied in SWAN is the same as that used in Section 5.2.2. In the SAM1D sub-module, the frequency space up to 2.0 Hz is spanned by 60 equidistant frequency bins and, in order to model the normally-incident, long-crested wave field, the longshore wavenumber space is spanned by 101 equidistant wavenumber bins running between ± 1 rad/m. The parameter settings for the bulk dissipation were found by fitting the simulation results for the significant wave height to observations. Good correspondence with the observations was found for the parameter values $\alpha_{CR} = 1.0$, $\gamma_{CR} = 0.85$, which is in agreement with the finding of Janssen (2006). In what follows, both the influence of the relaxation parameters β_D and β_{NL}, and the frequency distribution of the depth-induced dissipation (r_0) are considered.

Figures 5.12 and 5.13 compare the computed spectra and integral parameters for three parameter settings of the combined two-equation model. The integral parameters were obtained by integration over the frequency range 0.25 to 2.0 Hz. Firstly, the model setting $\beta_D = \beta_{NL} = 0.1$ and $r_0 = 1.0$ is investigated, which represents the combination of very weak relaxation and the distribution of dissipation proportional to the local spectral density. Figure 5.12 shows that this model variant yields good agreement with observations up to the bar, with accurate energy levels at both the higher and lower harmonics of the spectrum. Beyond the bar, however, this simulation starts to diverge from the observations, and eventually becomes unstable. This behaviour is also seen in the integral parameters presented in Figure 5.13. The significant wave height is reproduced well, but the mean period starts to diverge from the observations beyond the bar. For this variant, in which the breaking dissipation is proportional to the local spectral density, the prediction of skewness and asymmetry is quite inaccurate. Subsequently, the addition of relaxation as a function of the breaking intensity ($\beta_D = 1.5, \beta_{NL} = 0.1$) and predominantly frequency-squared weighting of the breaking dissipation ($r_0 = 0.1$) is considered. It is noted that this configuration is analogous to the approach of Herbers *et al.* (2003). Figures 5.12 and 5.13 show that with this model setting the spectra appear fairly similar to the previous result, but that the integral wave parameters improve. The mean period prediction behind the bar agrees somewhat better with the observations, and the agreement between computed and observed skewness and asymmetry improves significantly. However, as with the previous model setting, the simulation becomes unstable inside the surfzone behind the bar. The final model setting investigated has the relaxation as a function of both the nonlinearity and the breaking intensity ($\beta_D = \beta_{NL} = 1.5$) and maintains the weighting of the breaking dissipation with the frequency squared ($r_0 = 0.1$). From Figure 5.12 it is seen that with this setting the spectra still correspond well with the observations, although there is a tendency towards overestimating the subharmonic frequencies. Figure 5.13 shows that all integral parameters are predicted adequately, with the exception of the skewness, which is deteriorated somewhat with respect to result of the previous variant. It is also seen that, with relaxation a function of both nonlinearity and breaking, the simulation remains stable beyond the bar and throughout the surf zone.
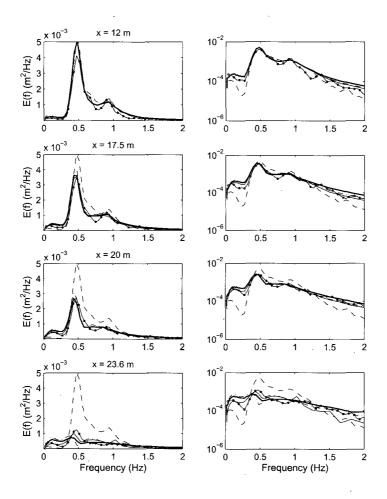
Figure 5.12: Comparison between spectra produced by the combined two-equation model and laboratory observations of Boers (1996) (Case 1A), on linear (left-hand side) and logarithmic (right-hand side) axes. Results of the two-equation model with $\beta_D = \beta_{NL} = 0.1$ (thin solid line) and $\beta_D = \beta_{NL} = 1.5$ (thick solid line) are shown. Observations indicated by line with circles; observed spectrum at the boundary indicated by dashed line.
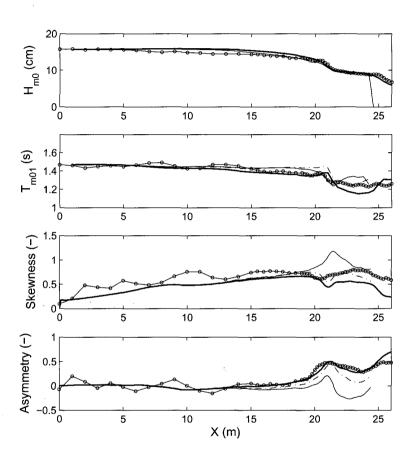
Figure 5.13: Comparison between integral parameters produced by the combined two-equation model and laboratory observations of Boers (1996) (Case 1A). Results of the two-equation model with $\beta_D = \beta_{NL} = 0.1$ (thin solid line), with $\beta_D = 1.5, \beta_{NL} = 0.1$ (dash dot line) and $\beta_D = \beta_{NL} = 1.5$ (thick solid line) are shown. Observations are indicated by line with circles.

To conclude, in this section the implementation of SAM1D as a sub-module into SWAN was validated for idealized situations over a submerged bar and for a barred beach, in which the processes of triad interaction and depth-induced breaking can be isolated. From these results it can be concluded that the implementation of SAM1D into SWAN, as a sub-module to compute the triad source term, is successful. A second objective of this section was an investigation of the appropriate settings for the parameters β_D, β_{NL}, α_{CR}, γ_{CR} and r_0 contained in the SAM1D sub-module. Using the findings of Janssen (2006) as a point of departure, it was found that for depth-induced breaking, using the CRAD model, $\alpha_{CR} = 1.0$, $\gamma_{CR} = 0.85$ and $r_0 = 0.1$ does indeed yield satisfactory results for the cases considered. Regarding the magnitude of the relaxation parameter, the setting $\beta_D = \beta_{NL} = 0.1$ (very weak relaxation) appears to yield the best result for the submerged bar situation, but gives unsatisfactory results for the barred beach. For the barred beach case, the options to include relaxation as a function of only breaking intensity ($\beta_D = 1.5$, $\beta_{NL} = 0.1$) and of both breaking intensity and the strength of nonlinearity ($\beta_D = \beta_{NL} = 1.5$) were investigated. The best agreement with observations was found for the latter setting. Considering that the applications in the remainder of this investigation will focus on barred beach situations, the preference is given here to the setting $\beta_D = \beta_{NL} = 1.5$.

5.4 Field case of a prismatic barred beach

Having validated the implementation of the SAM1D model into SWAN, the attention is now turned to a field case. Janssen (2006) demonstrated that the SAM1D model is able to simulate swell-dominated conditions over bar-beach geometries well. In the present study, Janssen's investigation is extended by considering the evolution of a mature wind sea field from outside the surfzone to the shore. For this investigation, the deep water and finite depth processes of wind input, whitecapping, quadruplet interaction and bottom friction are accounted for in addition to the surfzone source terms considered above. The aim of this investigation is firstly to determine the accuracy of the default version of SWAN using the LTA and the possible improvements found with the two-equation model and, secondly, to explore the influence of the various processes on the development of the directional spectrum outside and through the surf zone.

5.4.1 Case selection and description

The Field Research Facility (FRF), near the town of Duck, North Carolina on the Atlantic coast of the USA, serves as a coastal observatory as part of the Coastal and Hydraulics Laboratory (CHL), one of the six laboratories of the Waterways Experiment Station, and is operated by the US Army Corps of Engineers. The FRF features a main pier, running about 500 m into the sea, which during typical wave conditions covers the entire surf zone.
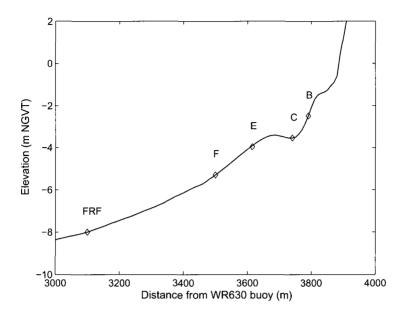
Figure 5.14: Profile of the barred beach at Duck, measured on 97/10/30, showing the locations of the nearshore arrays.

The pier, running along shore normal, is orientated at 72° TN. The bathymetry at the FRF is approximately prismatic, making it ideal for the evaluation of a model that is restricted to one-dimensional bottom variation, such as the investigated two-equation model. During September to November 1997 a large experiment was conducted to study coastal processes, featuring detailed measurements of wind, wave and tidal conditions, currents and sediment transport. In the nearshore, waves were measured by longshore arrays of pressure sensors, at the locations identified as the FRF, F, E, C and B arrays in Figure 5.14. Considering the limited depth penetration of pressure signals from the shorter frequencies, the spectra processed from these observations are reliable only up to a frequency of about 0.30 Hz. Wind and mean water level data were recorded at the seaward end of the FRF pier, about 470 m offshore. The wave climate at Duck is characterised by swell-dominated conditions from distant storms on the Atlantic. For the present investigation, however, a pure wind sea condition, directed perpendicular to the coast, was sought. During the duration of the SandyDuck '97 experiment, a few such conditions were recorded. The most energetic of these conditions occurred on November 13, 1997, during which the wind, as measured at the FRF, was blowing from 64° TN (approximately perpendicularly onshore) for a duration of about 18 hours, reaching a maximum speed of $U_{10} = 13$ m/s. This created a single-
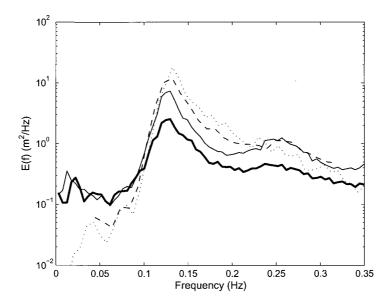
Figure 5.15: Frequency spectra observed during the SandyDuck '97 field experiment on 13/11/1997 at 19:00. Shown are the spectra offshore at the WR630 buoy (dots), at the FRF Array (dash), the E Array (thin solid line) and the B Array (thick solid line).

peaked wind sea spectrum offshore ($H_{m0} = 3.19$ m and $f_p = 0.13$ Hz), as observed at the WR630 buoy, situated 4 km from the shore, at a depth of 17 m. This wave field has a dimensionless frequency of $f_p^* = 6.6 \times 10^{-3}$, so that it can be considered as near maturation. Figure 5.15 presents the evolution of the observed, directionally integrated spectra from the offshore WR630 to the shoreline, whereas Figure 5.16 presents the corresponding directional spectra. Figure 5.15 shows that the observed directionally-integrated spectrum at WR630 has a characteristic deep water shape. Moving towards the coast, a clear first harmonic and significant low-frequency energy develop in the spectrum, followed by a large reduction of energy levels at the spectral peak and eventually a flattening out of the spectral tail. The observed directional spreading is large at the FRF Array, and reduces somewhat moving toward the shore.

5.4.2   Simulations

The simulations of the event of November 13, 1997 at 19:00 were conducted for the two model variants investigated above: The first is SWAN using the LTA triad expression
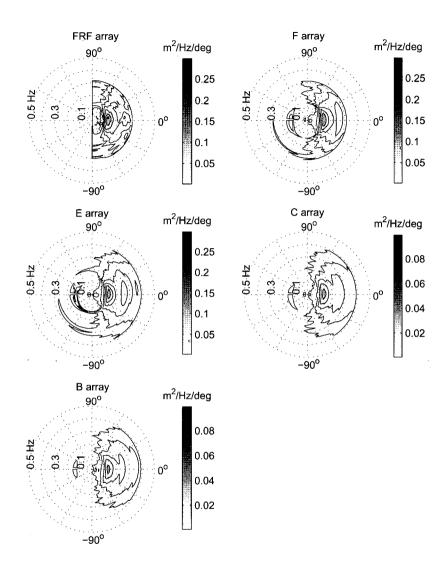
Figure 5.16: Observed directional spectra at the five nearshore arrays, for the event of 13/11/1997 at 19:00, during the SandyDuck '97 field experiment. Contours of spectral density are logarithmically distributed, having the values 0.3, 0.1, 0.0333, 0.0111, 0.0037, 0.0012 and 0.0004 m²/Hz/deg. Spokes indicate direction in which wave components are travelling, relative to shore normal.

(with $\alpha_{EB} = 0.05$ and $f_{max,EB} = 2.5f_{m01}$) with the Battjes and Janssen (1978) breaker model (with $\alpha_{BJ} = 1.0$, $\gamma_{BJ} = 0.73$ and a frequency-independent distribution). This configuration closely resembles the default SWAN model, and will be referred to simply as the LTA model variant hereafter. The second variant is the two-equation model, featuring the SAM1D triad expression with $\beta_D = \beta_{NL} = 1.5$ and the CRAD breaker model. By comparing simulated and observed significant wave heights in a number of trial runs, the parameter values for the CRAD model were set at $r_0 = 0.1$, $\alpha_{CR} = 1.0$ and $\gamma_{CR} = 0.73$. The last of these parameters is lower than the value used by Janssen (2006) and found for the laboratory cases above, but yielded a better fit to the observations for the present (single) field case. The choice of a lower value for γ_{CR}, however, does not constitute a re-calibration of the CRAD model.

The LTA and two-equation model variants were both combined with the same set of expressions for the deep water processes. For wind input and whitecapping, two sets of source terms were considered, namely those of Komen *et al.* (1984) and the saturation-based model presented in Chapter 4. Quadruplet nonlinear interaction was modelled with the DIA. All these expresisons were applied with their default parameter values. For the process of bottom friction, the formulation of Hasselmann *et al.* (1973) with $C_{JON} = 0.067$ m^{2}s^{-3} is used, which is the SWAN default and recommended for wind sea conditions (Bouws and Komen 1983).

Considering discretisation, both model variants were run in one-dimensional mode (alongshore parallel contours and a directional wave field). The computational axis was directed perpendicularly towards the beach with its origin at the depth contour of the WR630 buoy. In this Cartesian frame of reference, waves arriving from 72° TN travel in the direction 0°, waves from the NE quadrant travel in the directional sector [0° 90°] and waves from the SE quadrant travel in the sector [0° −90°]. The discretisation in cross-shore geographical space is 1 m. In SWAN (in both the default and two-equation model variants), a directional discretisation of $\Delta\theta = 2°$ is applied on the full circle of directions and the frequencies are logarithmically distributed with $\Delta f/f = 0.1$, running from 0.01 to 0.5 Hz. In the SAM1D sub-module, the frequency space up to 0.5 Hz is spanned by 45 equidistant frequency bins and the longshore wavenumber space by 101 equidistant wavenumber bins running between ±1 rad/m. This longshore wavenumber domain is sufficiently large so that no aperture limitation is imposed on incoming wave directions, i.e. all spectral components on the incoming semi-circle are included in SAM1D's spectral domain. The directional wave field observed at the WR630 buoy was input on the offshore model boundary. The observed wind velocity and an observed mean water level of +1.03 m NGVT (both measured at the seaward end of the FRF pier) were applied spatially uniformly over the computational domain. The one-dimensional nearshore depth profile used in the simulations was taken from bathymetry observations made on 30/10/97 (Figure 5.14). Considering the relatively short propagation distance from the WR630 buoy to the shore (4 km), all simulations were conducted in stationary mode. Using this model setup, computations with the two-equation model required about 100 times as much simulation time those of the LTA model.

Triads with deep water source terms

Figure 5.17 compares the evolution of the simulated and observed frequency spectra over a distance of 4 km, when all deep water and shallow water source terms are active. It is seen that there are significant differences between the simulated and observed spectra. At the FRF and F arrays, the first harmonic is somewhat underestimated by both models. However, closer to shore at the B array, the LTA model variant shows a strong growth of energy density concentrated around the first superharmonic. Also, between the spectral peak and the first superharmonic there are signs of an additional smaller peak that does not appear in the observations. The spectra produced by the two-equation model are also at quite a variance with the observations. At the nearshore C and B arrays, energy levels at the first superharmonic and the high frequency tail of the spectrum are strongly overestimated. This is in contrast to the simulation results obtained for the laboratory cases above, where these energy levels where generally well reproduced.

Figures 5.18 and 5.19 present the directional spectra produced by the LTA and two-equation model variants. At the FRF Array, both model variants produce similar spectra, both with a relatively large directional spreading. From this point to the shore, however, the complexity of the simulated directional spectra increases significantly. For the LTA model variant, the simulated directional spectra at arrays F and E correspond rather well to those of the observations, although the directional spreading of the model is somewhat smaller. At the nearshore C and B arrays, however, the simulated spectra differ strongly from the observations: the distribution of energy becomes irregular and narrower than that of the observations, and the first superharmonic becomes pronounced. Furthermore, two small additional interaction peaks develop at $\pm 30^o$ relative to the spectral peak direction, which are not found in the observations. For the two-equation model, the difference between simulation results and observations is even greater: From Array F to the shore the directional spreading becomes larger that observed values. High energy levels develop at the first superharmonic and at frequencies above it. As found with the LTA variant, additional interaction peaks develop at $\pm 30^o$ to the spectral peak direction, which are not supported by the observations.

Figure 5.20 compares the integral parameters of the two simulations with the observations, which were obtained by integration over the frequency range 0.05–0.30 Hz. The results of significant height of both model variants agree well with observations, with the two-equation model producing somewhat lower values in the surf zone. The difference between the simulation results of the mean period is more pronounced. The LTA model variant yields a good general prediction of the mean period (except at the shoremost B Array, at 3790 m), despite the inaccuracy of its computed spectra. By contrast, the two-equation model underestimates the mean period quite strongly, due to the large increase in energy over the higher frequencies of the spectrum, as seen above. The bottom panels of Figure 5.20 compare the simulated skewness and asymmetry to those derived from observations at the nearshore arrays. The observations show that skewness reaches a maximum
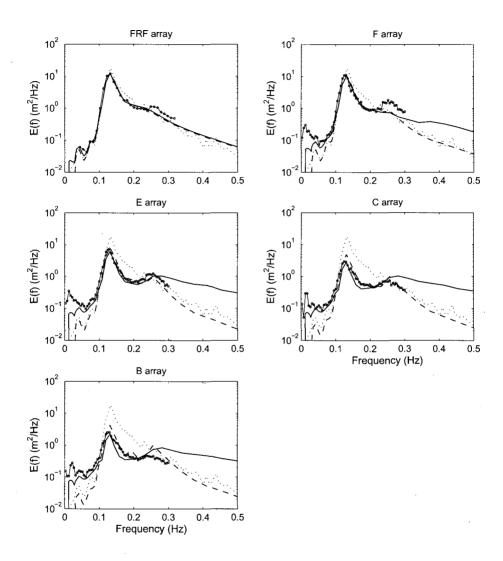
Figure 5.17: Comparison between simulated and observed frequency spectra, for Sandy-Duck '97 event of 13/11/1997 at 19:00. Simulation including both shallow and deep water source terms, active over the entire domain. Shown are the results of the LTA model (dashed line), the two-equation model (solid line) and observations (line with circles). Input spectrum at the WR630 buoy indicated by dotted line.
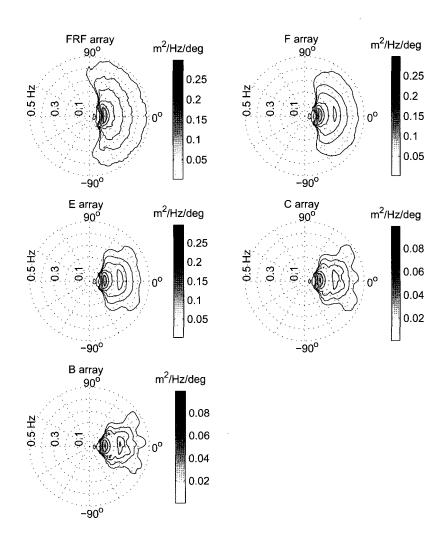
Figure 5.18: Simulated directional spectra for the SandyDuck '97 event of 13/11/1997 at 19:00, produced by the LTA model with both shallow and deep water source terms active. Spokes indicate direction in which wave components are travelling, relative to shore normal.
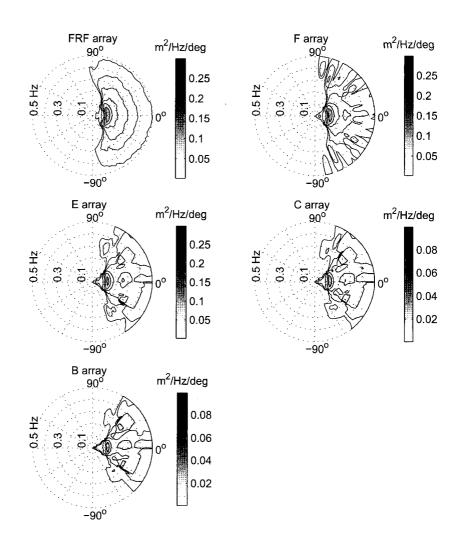
Figure 5.19: Simulated directional spectra for the SandyDuck '97 event of 13/11/1997 at 19:00, produced by the two-equation model with both shallow and deep water source terms active. Spokes indicate direction in which wave components are travelling, relative to shore normal.
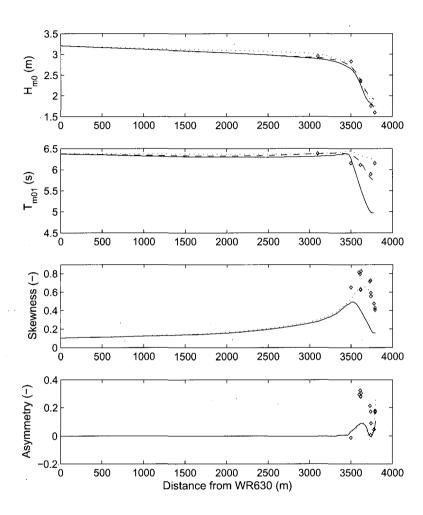
Figure 5.20: Comparison between simulated and observed integral parameters for Sandy-Duck '97 event of 13/11/1997 at 19:00. Simulation with with both shallow and deep water source terms active over the entire computational domain (quadruplet interactions modelled with the DIA). Shown are the results of the LTA model (dashed lines), the two-equation model (solid lines) and, as reference, the two-equation model with only triads and depth-induced breaking active (dotted lines). Observations indicated with diamonds.

over the bar and decreases again behind it. The observed asymmetry has a small value offshore of the bar (F Array, at 3500 m), reaches a local maximum at the crest of the bar, a local minimum behind it, and increases again closer to the shore. The skewness and asymmetry simulated by the two-equation model follow this observed trend, but the magnitudes of both are significantly below the observed values.

To investigate the effect that the addition of deep water source terms has had on the results of the two-equation model, Figure 5.20 includes the results of a sensitivity run where all deep water source terms were deactivated. With the deactivation of the deep water source terms, the results of the significant wave height are fairly similar, but the mean period increases strongly in the surf zone. The higher-order statistics, in particular the skewness, increases upon the deactivation of the deep water source terms. The latter result suggests that in the base model run the nonlinearity of the wave field has been suppressed by the activity of the deep water source terms.

Interplay between source terms

To gain insight into these results, Figure 5.21 presents the strength of the nonlinear source terms, in terms of absolute values integrated over spectral space, for a number of model variants. The top panel of Figure 5.21 presents the respective strengths of the LTA, SAM1D and DIA terms over the simulation domain when each of these is active in isolation. From this it can be concluded that, acting in isolation (i.e. without quadruplet interactions), the triad source terms are weak in the offshore and increases strongly toward the coast, as expected. The SAM1D expression yields generally stronger interaction than the LTA expression, as was also seen in Figure 5.10 above. Acting in isolation, the DIA quadruplet expression has its highest interaction value offshore and generally becomes weaker towards the coast. The middle panel of Figure 5.21 presents the situation when the LTA and DIA are active simultaneously, as in the LTA model variant. The interaction strength of the LTA term reduces somewhat relative to the values it has when in isolation, but in the nearshore that of the DIA increases by up to nearly two orders of magnitude relative to its value in isolation. This reveals that the DIA expression is strongly influenced by the changes that the LTA triad expression brings to the nearshore spectrum. The lower panel of Figure 5.21 shows that the response of the DIA expression to spectral changes brought about by the SAM1D term is even more pronounced—in the very nearshore the strength of the DIA expression increases by nearly five orders of magnitude. The strength of the SAM1D expression, on the other hand, is reduced somewhat throughout the simulation domain.

There are a number of possible explanations for the observed interplay between the triad and quadruplet source terms in the nearshore. Considering the approximate nature of the DIA, the most obvious reason might be that the fault lies with its parameterization or with the depth scaling of Herterich and Hasselmann (1980) applied in SWAN. Simulations conducted with a depth-dependent version of the WRT exact quadruplet method (results not presented here) showed that the interaction effect indeed reduces significantly, but
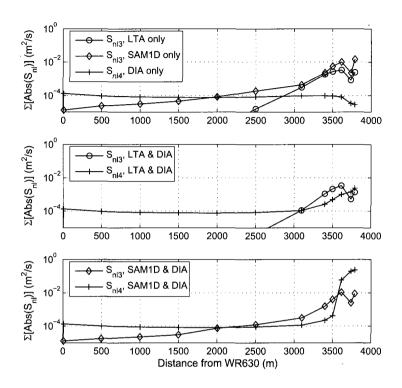
Figure 5.21: Integrated magnitudes of the nonlinear source terms during simulation of the SandyDuck '97 event of 13/11/1997 at 19:00. Results for various combinations of the LTA, the two-equation model and the DIA.

that increases in the strength of quadruplet interaction of an order of magnitude in the nearshore remain. Another possible cause of the observed behaviour is that SWAN adds a so-called parametric tail to the computed (prognostic) spectrum beyond the highest bin in the computational frequency domain. This parametric tail is used to facilitate the computation of quadruplet interaction, and has a fixed shape. In SWAN, a default tail shape of $\propto f^{-4}$ is used, in order to agree with the spectral tail shape produced by quadruplet interaction in deep water (Tolman 1992). However, when in the nearshore the computed spectral tail reduces in gradient due to shallow water nonlinearity (specifically in the two-equation model), the fixed gradient of the parametric tail starts to differ from that of the prognostic tail. This results in a discontinuity in the gradient of the spectral tail. The quadruplet source term subsequently labours to correct this discontinuity, leading to the presented errors. A solution would therefore be to define an adjustable parametric tail

that would adapt to the prognostic tail. Attempts at solving this problem by parametric tails ranging from $\propto f^{-4}$ to $\propto f^{-1}$ shapes were unsuccessful, in part due to the complicated two-dimensional nature of the full frequency-directional spectrum.

A third explanation is of a more fundamental nature, namely that the formulation for quadruplet interaction taken up in the DIA is based on assumptions of homogeneity and Gaussianity. In the nearshore the wave field becomes strongly nonlinear, so that the assumption of Gaussianity is violated. It was seen also, based on the computed skewness values (Figure 5.20), that the nearshore wave field is in fact forced back towards Gaussianity if this expression for quadruplet interaction is included nonetheless. A theoretically justified solution to the present problem would therefore be to discontinue the calculation of quadruplet interaction in areas of strong nonlinearity. A number of criteria can be used for this purpose: Janssen and Onorato (2007) show that quadruplet interaction goes to zero at $kd = 1.363$, and that for $kd << 1.363$ quadruplet expressions such as (4.5) become invalid. They refer to Zakharov (1999), who shows that for quadruplet interaction to take place the wave components must satisfy $(ak)^2 << (kd)^5$, where a is the amplitude of the wave component. A more practical measure, that describes the same balance as the latter, is the Ursell number, for which a spectrally-based expression is given by (5.2) above. A further option is to use the computed skewness as criterion, following on the conclusion of Ochi and Wang (1984) that below a skewness value of about 0.2 the wave field can be considered to be Gaussian. Since the behaviour of the skewness follows that of the Ursell number, and the skewness is only computed in the two-equation model, in what follows the Ursell number will be used as a practical measure of wave field nonlinearity.

Ursell number limit on quadruplet interaction

In what follows, the influence of deactivating quadruplet interaction in strongly nonlinear wave fields is investigated, for which the Ursell number is used as criterion. Quadruplet interaction is disabled for values of $Ur > 0.1$ which, in the present case, agrees with a computed skewness of about 0.25, and a dimensionless depth at the spectral peak of $k_p d = 0.9$. This is reached at a distance of $x \approx 2900$ m shoreward of the WR630 buoy, just offshore of the FRF Array (see Figure 5.20). Although quadruplet interaction (and the limiter) is deactivated over this domain, the remaining deep water source terms (wind input, whitecapping and bottom friction) stay active.

Figures 5.22 and 5.23 present the directional spectra simulated by the LTA and two-equation models respectively. Comparison with Figures 5.18 and 5.19 show that these results differ significantly from the situation where quadruplet interaction remained active throughout the surf zone. The directional spectra produced by both models become less erratic, the additional peaks at $\pm 30°$ off the peak direction disappear, and the amount of directional spreading reduces, especially for the two-equation model. Comparison with Figure 5.16 shows that the directional spreading in the results of both models now underpredict the observed values. Because of the assumption of collinear interaction, the directional spreading produced by the LTA model variant tends to broaden towards higher
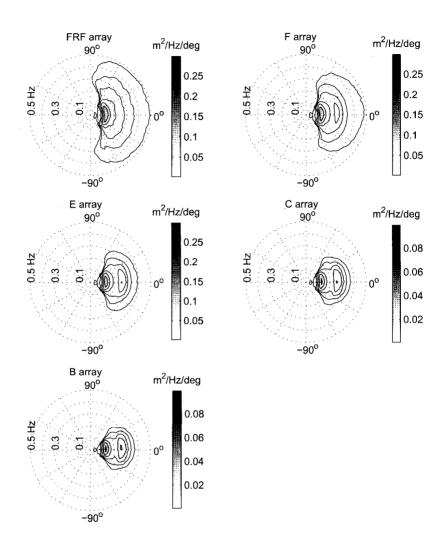
Figure 5.22: Simulated directional spectra at three stations for the conditions of 13/11/1997 at 19:00. Results obtained using the LTA model including deep water source terms, but with quadruplet interaction (DIA) active only for Ursell values $Ur < 0.1$. Spokes indicate direction in which wave components are travelling, relative to shore normal.
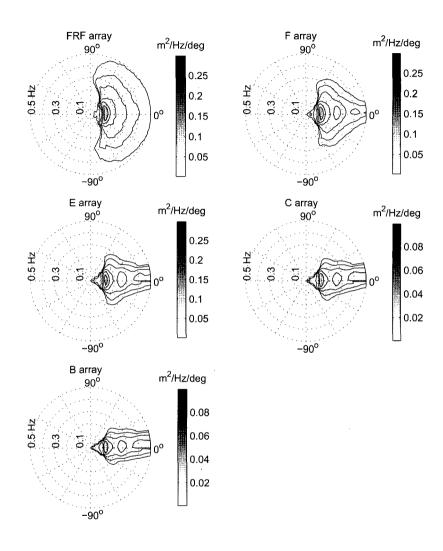
Figure 5.23: Simulated directional spectra at three stations for the conditions of 13/11/1997 at 19:00. Results obtained using the two-equation model including deep water source terms, but with quadruplet interaction (DIA) active only for Ursell values $Ur < 0.1$. Spokes indicate direction in which wave components are travelling, relative to shore normal.
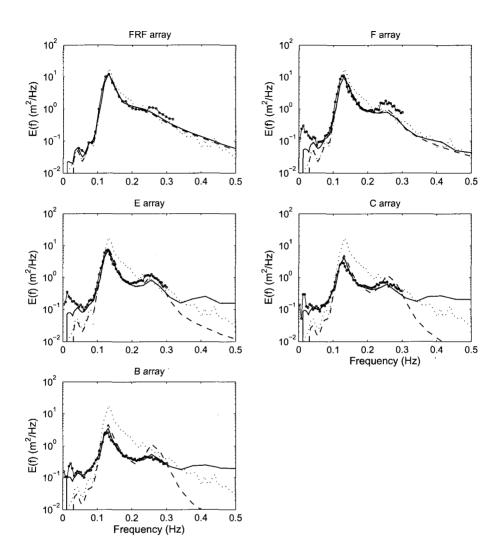
Figure 5.24: Comparison between simulated and observed frequency spectra, for Sandy-Duck '97 event of 13/11/1997 at 19:00. Simulation including both shallow and deep water source terms, but with quadruplet interaction (DIA) only active for $Ur < 0.1$. Shown are the results of the LTA model (dashed line), the two-equation model (solid line) and observations (line with circles). Input spectrum at the WR630 buoy indicated by dotted line.
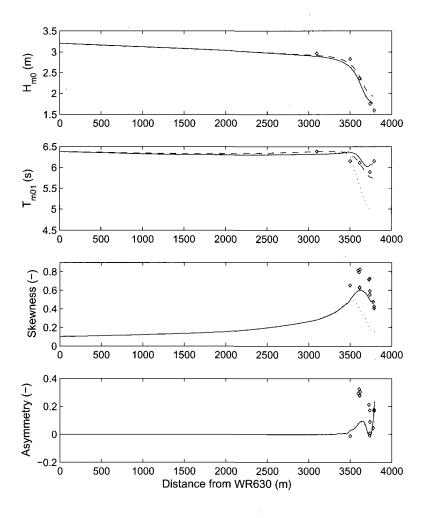
Figure 5.25: Comparison between simulated and observed integral parameters for Sandy-Duck '97 event of 13/11/1997 at 19:00. Simulation with all source terms active, except the quadruplet interaction term, which is only active for Ursell number values $Ur < 0.1$. Shown are the results of the LTA model (dashed lines), the two-equation model (solid lines) and, as reference, the two-equation model with both shallow and deep water source terms active over the entire domain (dotted lines). Observations indicated with diamonds.

frequencies, which agrees fairly well with the observations. By contrast, the two-equation model produces directional spreading results that tend to reduce towards higher frequencies, which does not appear to agree with the observations.

Figure 5.24 compares the directionally integrated spectra of these simulations. As found above, the simulated development of the first harmonic outside of the surf zone is slow, so that it is underestimated at the FRF Array by both models. Closer to shore, however, the LTA is again seen to induce strong growth of the first superharmonic. At the C and B arrays this results in an overestimation of energy levels at this harmonic. The LTA model also underestimates energy levels below the spectral peak, owing to the omission of difference interactions. By contrast, the two-equation model produces a good estimate of energy levels at the first superharmonic, more realistic energy levels at frequencies higher than this, and also predicts the subharmonic components well. Figure 5.25 compares the corresponding integral parameters with the observations, and also with the results obtained in the previous section (in which the quadruplet term was always active). The most notable changes with respect to the earlier results are in the mean period and the skewness. The predicted mean period produced by the two-equation model is increased by the partial deactivation of the quadruplet term, and the magnitude of the skewness is considerably larger. Both of these quantities are now in reasonable agreement with the observations. Close to the shore, the results of the asymmetry are also seen to increase, bringing them closer to the observations. With reference to the discussion in Section 5.1, the results of the sections above would suggest that the recommendation of Bottema (2001a), to keep quadruplet interaction (and the limiter) active in combination with triad interaction, leads to unrealistic model behaviour in the surf zone. Model behaviour appears to improve when quadruplet interaction is deactivated where triad interaction becomes the dominant nonlinearity.

Finally, it is investigated to what extent the choice of the deep water source terms of wind input and whitecapping affect the results obtained above. Figures 5.26 and 5.27 present the frequency spectra and integral parameters computed using the saturation-based deep water source term combination, presented in Chapter 4. It was seen in Chapter 4 that this deep water source term combination corrects the underprediction of the peak and mean periods in deeper water, in part due to higher dissipation over the spectral tail than with the Komen *et al.* (1984) formulations. The difference in energy levels in the tails of the simulated spectra at the seaward FRF Array (at 3100 m) can be seen by comparing Figures 5.24 and 5.26. Considering integral parameters in this geographical region, it is seen that the mean period remains at the level observed at the WR630 up to the FRF array, and does not decrease as with the Komen *et al.* (1984) formulations (Figure 5.27). However, from the FRF Array to the shore, the differences in model results due to the alternative deep water terms are minor. Considering the higher-order statistics, Figure 5.27 shows that these are also unaffected by the application of alternative deep water source terms. This would imply that the shallow water source terms of triad interaction and depth-induced breaking are sufficiently dominant in the surf zone so that, given that the simulated wave
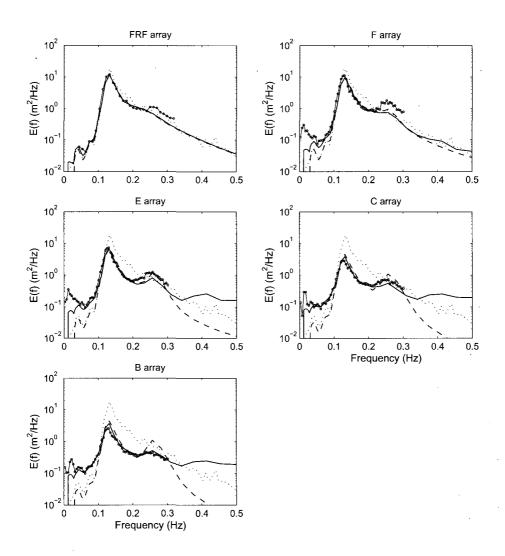
Figure 5.26: Comparison between simulated and observed frequency spectra, for Sandy-Duck '97 event of 13/11/1997 at 19:00. Simulation including both shallow and deep water source terms, the latter according to the saturation-based combination. Quadruplet interaction (DIA) only active for $Ur < 0.1$. Shown are the results of the LTA model (dashed line), the two-equation model (solid line) and observations (line with circles). Input spectrum at the WR630 buoy indicated by dotted line.
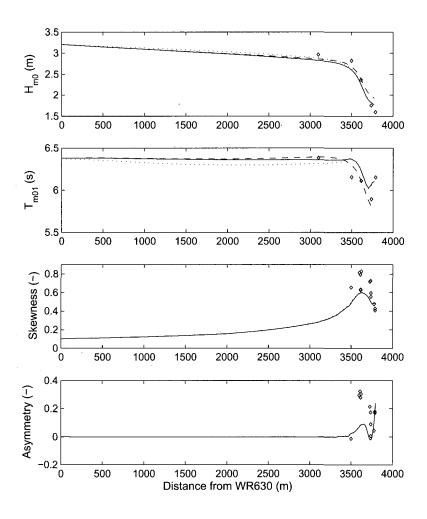
Figure 5.27: Comparison between simulated and observed integral parameters for Sandy-Duck '97 event of 13/11/1997 at 19:00. Simulation including both shallow and deep water source terms, the latter according to the saturation-based combination. Quadruplet interaction (DIA) only active for $Ur < 0.1$. Shown are the results of the LTA model (dashed lines), the two-equation model (solid lines) and, as reference, the two-equation model with the deep water source terms of Komen *et al.* (1984) in dotted lines. Observations indicated with diamonds.

fields arriving from deeper water have comparable peak frequencies, the results within the surf zone are rather insensitive to the combination of deep water source terms applied.

5.5 Conclusions

In this chapter it was investigated whether the performance of SWAN in the surf zone can be improved by applying a less parameterized expression for triad interaction and a modified expression for depth-induced breaking. To this aim, the performance of SWAN with the LTA—the current default expression for triad interaction—was reviewed and compared with that when using a two-equation model for triad interaction in which the spatial evolution of the bispectrum is fully computed. For this, the state-of-the-art two-equation model SAM1D of Janssen (2006) was implemented as a sub-module into SWAN. Due to the first-principle nature of this model, the simulations with the two-equation model are computationally intensive and intended only to serve as a benchmark for future parameterizations. The comparisons were made both for idealised laboratory flume situations and for a field case representing a wind-sea propagating through the surf zone, in which all deep water source terms are active also. The following conclusions can be drawn from this investigation:

(a) Considering the performance of the default triad and depth-induced breaking expressions in the absence of deep water source terms, it was found that with some calibration the LTA is able to reproduce the general variation of the mean period in the surf zone with reasonable accuracy for all the cases considered. For the range of cases considered here, the setting $\alpha_{EB} = 0.05$ and $f_{max,EB} = 2.5 f_{m01}$ yielded the best results. Considering the reproduction of the significant wave height, the finding of Becq-Girard et al. (1999) that energy density is spuriously created in non-dissipative propagation over a bar, is confirmed. This spurious growth of energy density does however not detract from model performance in the surf zone, since here this behaviour is overshadowed by depth-induced breaking dissipation. Although, with calibration, it is possible to reproduce integral parameters well, the underlying spectra are still reproduced poorly: too much energy is concentrated at the first harmonic, too little energy is found in the high frequency tail and energy is underestimated at the subharmonics.

(b) Considering the performance of the two-equation SWAN-SAM model in the absence of deep water source terms, it was found that this model yields a better representation of the observed frequency spectra, including a better reproduction of the overall spectral shape at frequencies above the spectral peak, and the inclusion of subharmonics. This is the result of the inclusion of all resonant and near-resonant sum and difference interactions. Accordingly, the integral parameters of mean period are also predicted well. In addition, the higher-order statistics are predicted with reasonable accuracy.

These improvements come at the cost of significantly higher computational times than required for the LTA. In the idealised flume cases the effect of frequency scaling of depth-induced dissipation and of adjustment to the degree of triad relaxation were investigated. Although alternative settings yield better results in some cases, it is confirmed that the best overall results are found for $r_0 = 0.1$ and $\beta_D = \beta_{NL} = 1.5$, as proposed by Janssen (2006). In other words, the best results were obtained for relatively strong relaxation in the fourth-order closure term, and a frequency-squared weighting of the dissipation due to depth-induced breaking.

(c) In the field case application, the combination of deep water source terms with triad interaction was found to lead to unexpected model behaviour. This was found for both the LTA and SAM1D. Energy levels at higher frequencies were strongly overestimated and additional directional interaction peaks developed, which are not found in the observations. It is hypothesised that this model behaviour stems from the fact that the currently-used expressions for quadruplet interaction are not valid in the surf zone. The quadruplet interaction source term appears to react strongly to the reduction of the spectral tail slope in the surf zone, which is caused by triad interaction. Since the SAM1D expression alters the spectrum more strongly than the LTA, the reaction of the quadruplet term appears to be the strongest for the former. A practical manifestation of this interplay between the nonlinear terms is that quadruplet interaction attempts to force shallow water spectral shapes back to a self-similar, deep water shape.

(d) A number of solutions to the erroneous interplay between the triad and quadruplet source terms were investigated. The most effective and theoretically justified of these was to deactivate quadruplet interaction in the surf zone where nonlinearity is strong, for which the Ursell number was used as criterion. This alteration removed the apparent spurious model behaviour, yielding model results that were in better general agreement with the observations than when the quadruplet term was active everywhere. This result implies that the recommendation of Bottema (2001a), to keep the quadruplet source term active in combination with triad interactions, does not lead to realistic modelling results in the surf zone when using the current expressions for quadruplet interaction. This finding alters the conclusion (d) of Chapter 3, in which it was concluded, from the point of view of numerics, that the combination of the action limiter and quadruplet interaction could be left activated in the surf zone. As was shown in Chapter 3, deactivating quadruplet interaction, and hence the limiter, has the added benefit of significantly reducing the number of model iterations required to reach convergence.

(e) Alternative expressions for deep water physics, namely the saturation-based whitecapping expression presented in Chapter 4, have some impact offshore of the surf zone, but have little impact inside it.

(f) In terms of directional spreading, the final results of the LTA model agree favourably

with the observations. By contrast, the final results of the SAM1D model were found to underpredict the observed values of directional spreading, which is in agreement with the finding of Janssen (2006). The present study showed that in combination with quadruplet interaction the directional spreading can be considerably enhanced, although, for the reasons given, the general model results are poorer. Possible further explanations for the observed underprediction of directional spreading, as discussed by Herbers *et al.* (2003) and Janssen (2006), are that wave components may be directionally scattered by depth-induced breaking, or that components with shorter wavelength may be directionally scattered due to interaction with ambient currents.

Chapter 6

General Conclusions

In this study it was investigated whether the overall accuracy of the wind wave model SWAN could be improved by using alternative formulations for source terms in deep and shallow water, and by implementing more accurate numerical methods for solving the source terms in the action balance equation. This was done by firstly considering the impact of a number of numerical choices, in particular the action limiter and stopping criteria, on the accuracy of SWAN in deep and swallow water. Thereafter, the modelling of processes that are dominant in deep water, namely generation by wind, whitecapping dissipation and quadruplet nonlinear interaction, were considered. Finally, it was investigated to what extent the accuracy of SWAN in the surf zone can be improved by implementing more detailed expressions for triad nonlinear interaction and depth-induced breaking.

Concerning the impact of the numerics employed in solving the action balance equation during stationary simulation, the following conclusions are drawn:

(a) The action limiter, which is used to ensure stable convergence behaviour whenever quadruplet interaction is active, does not significantly influence the outcomes of converged stationary simulations either in deep water or in shallow water. This is despite the finding that the limiter is typically heavily used throughout the computational domain, and during the entire simulation. This result implies that, from a point of view of accuracy, alternative less intrusive measures to ensure model stability (such as under-relaxation) appear not to be necessary. Action limiting therefore appears to remain the most effective way of ensuring stability in operational versions of SWAN.

(b) Although the action limiter does not influence converged model results, it can greatly increase the number of iterations required for model convergence in shallow water where triad interaction and depth-induced breaking are active. This happens because the action limiter has been developed for deep water application, with an f^{-5} shape, in close agreement to the high-frequency equilibrium shape of the frequency spectrum

in deep water. As a result, only small changes in the action at high frequencies are allowed per iteration, slowing down the formation of higher harmonics and the rapid loss of energy through depth-induced breaking in the surf zone. It would therefore be beneficial to the convergence speed in operational versions of SWAN to deactivate the action limiter, and therefore quadruplet interaction, in the surf zone.

(c) Frequency-dependent under-relaxation is an effective alternative method by which to enhance the stability of SWAN simulations. This method has the advantage of yielding smoother iteration behaviour than action limiting. However, depending on the amount of under-relaxation applied, this method can slow down the rate of convergence significantly, so that many more iterations are required to reach convergence. This method therefore appears to be only suitable for academic application.

(d) The default criteria for run termination are insufficient, as they typically end the simulation before full convergence is reached. These unconverged results can differ from those obtained at full convergence by more than 10%, adding significantly to model inaccuracy. The numerical accuracy of SWAN can be significantly improved by supplementing the current criteria with a criterion that considers the curvature of the curve traced by the significant wave height as a function of the iteration level.

Concerning the use of alternative and more detailed expression for the physical processes that are dominant in deep water, the following conclusions are drawn:

(e) Combining the default expressions of Komen et al. (1984) with an exact method for quadruplet interaction yields some improvement in model results over those obtained with the DIA in idealised deep water and finite depth situations. These improvements include a more accurate estimation of the spectral peak frequency and the reproduction of bimodal directional distributions at higher frequencies. However, the use of an exact quadruplet computation method does not fully remove the overprediction of the spectral peak frequency by the model, and energy remains overpredicted at higher frequencies. Furthermore, despite possibilities for improving the computational efficiency of such exact methods (Van Vledder 2005b), this model variant is at present only suitable to academic application.

(f) Combining the DIA with a saturation-based whitecapping expression after Alves and Banner (2003) that, for breaking waves, is a function of frequency-local variables, and a wind expression based on Yan (1987), yields significant improvement in both the peak and mean period measures. This is found in a wide range of applications in deep water and intermediate depths. Combining these wind input and whitecapping expressions with an exact method for computing quadruplet interaction improves these results further, but the high additional computational cost is considered to outweigh the marginal improvement in accuracy obtained.

(g) The investigated saturation-based whitecapping expression, which, for breaking waves, is a function of frequency-local variables only, provides more accurate estimates of wind wave growth in combined swell and wind sea conditions than the default white-capping expression of Komen *et al.* (1984), which is a function of the spectral mean wavenumber and steepness. However, the investigated model may need to be extended with additional physical descriptions of interactions within the wind sea field and interactions between swell and wind sea (e.g. Meza *et al.* 2000; Young and Babanin, 2006).

(h) Although the investigated combination of a whitecapping expression based on Alves and Banner (2003) and wind input based on Yan (1987) was found to yield generally better results than the default model, the investigated model appears to overestimate wind wave growth at very short dimensionless fetches. This model behaviour could have various sources, such as inaccurate specification of wind fields over land-sea boundaries, overestimation of wind forcing at small wave ages (Donelan *et al.* 2006), insufficient dissipation of very young waves, or even non-self-similar behaviour in very young wave fields, as suggested by Badulin *et al.* (2005).

Concerning the advances in accuracy that can be achieved by using more detailed expressions for shallow water source terms, the following is concluded:

(i) Concerning the performance of the default triad and depth-induced breaking expressions in the absence of deep water source terms, it was found that with some calibration the LTA is able to reproduce the general variation of the mean period in the surf zone with reasonable accuracy for all cases considered. However, although it is possible to reproduce integral parameters well with calibration, the underlying spectra are reproduced poorly: too much energy is concentrated at the first harmonic, too little energy is found in the high frequency tail and energy is underestimated at the subharmonics.

(j) Concerning the performance of the two-equation model of Janssen (2006) in the absence of deep water source terms, it was found that this model yields a better representation of the observed frequency spectra than the LTA, including a better reproduction of the broadband spectral shape at frequencies above the spectral peak, and the inclusion of subharmonics. Accordingly, the integral parameters of mean period are also predicted well. In addition, the higher-order statistics are predicted with reasonable accuracy.

(k) The combination of the source term expressions for triad interaction (especially the two-equation model) with those for deep water source processes was found to lead to unexpected model behaviour in the surf zone. Although the directional spreading tended to agree rather well with the observations, energy at higher frequencies in the spectrum was found to be overestimated and additional spectral peaks, not found in

the observations, were found to develop. It is hypothesised that this model behaviour stems from the fact that, in the surf zone, the expressions for quadruplet interaction—which have been derived for Gaussian and homogenous sea states—are applied to non-Gaussian and inhomogenous sea states, and therefore to conditions for which they are not defined.

(1) From the preceding conclusion, it would therefore be preferable, also from the point of view of model physics, to deactivate quadruplet interaction in shallow water. In this study, a spectrally-based Ursell number was used as an indicator of shallow water wave field nonlinearity—at high Ursell numbers quadruplet interaction and the limiter are deactivated. This alteration restored the model behaviour to within reasonable bounds. However, in the absence of quadruplet interaction, it was found that the model tends to underpredict the observed values of directional spreading, which is in agreement with the finding of Janssen (2006).

Chapter 7

Discussion

In this study, a number of aspects have been investigated that affect the accuracy of spectral wind-wave models designed for coastal application. This has been done within the context of the wind wave model SWAN, with the overall aim of improving the model's predictive accuracy. In pursuing this goal, this study was aimed at developing two types of model variants: a first that would represent detailed, state-of-the-art formulations of physics and high demands on numerical accuracy without consideration of computational cost (termed academic versions), and a second type that was aimed at operational application, in which efficient formulations of physics and numerics have the preference. Within this framework, topics that have been considered are the impact of currently implemented numerical techniques on model accuracy, and alternative formulations of source terms for improving model performance in deep water, in intermediate depths and in the surf zone. The progress made in this study on each of these topics, and the outlook towards further development in these areas, are discussed below.

7.1 Impact of numerics on model accuracy

Concerning the numerics of SWAN, the topics that have been considered in this study are the model's iteration behaviour, the impact of numerical measures designed to stabilise and speed up this iteration process, and the convergence criteria according to which the iteration process is ended. The default stopping criteria of SWAN, based on the slope of the iteration curve, were shown to typically fail to locate the true point of model convergence, with a detrimental effect on model accuracy. More dynamical, stricter criteria were developed in this study, which are based on the second derivative, or curvature, of the iteration curve. These criteria were shown to be more effective at locating the point of model convergence. The use of these stricter convergence criteria leads to improved model accuracy, but, if the underlying iteration behaviour remains the same, this will inevitably

167

result in longer computational time (more iterations).

At first glance, applying stricter convergence criteria therefore appears to be only useful for academic model versions. However, if the improved convergence criteria are taken as a starting point in the model development, future challenges lie in the reduction of the iteration time required to achieve these converged solutions. This may be achieved either by reducing the number of iterations that are required to reach convergence, or by reducing the time spent per iteration. An example of how the number of iterations may be reduced is by adapting the first guess used by SWAN. The closer the directional spectrum computed in the first guess resembles the simulated spectrum at the point of convergence (both in frequency and directional dimensions), the fewer iterations are required for convergence. This implies that theoretical spectra (such as JONSWAP) are not necessarily sufficient to use as first guess, but that the spectrum applied should agree with the particular set of source terms used in SWAN. One way to achieve this demanding goal is to use SWAN itself, run on coarser geographical and spectral grids, to generate a first guess spectrum. Successful application of such an approach has been shown by Van Vledder (2005a).

Concerning the reduction of time spent per iteration, the most common method applied is simulation on a parallel computer using, for example, domain decomposition in geographical space (e.g. Zijlema 2005). However, it may also be possible to speed up simulations that are performed on serial processors. One method would be to adapt the iteration process over a particular geographical area to the degree of model convergence in that area. For example, the simulation results of the Battjes and Janssen (1978) experiment (Figure 3.13) show that many more iterations are required inside the surf zone than in deeper water, when the action limiter is active everywhere (compare Figure 3.2). A gain in computational time per iteration may therefore be achieved by deactivating the iteration process in those geographical areas where convergence has already been reached. Therefore, methods are available or could be developed to achieve higher degrees of convergence using less computational time, making stricter convergence criteria a practical measure for operational purposes.

As outlined above, this study was aimed mainly at understanding the impact and accuracy of the numerics involved in the integration of the source terms of the action balance equation. The attention may subsequently be shifted to other numerical issues, such as improvements to the accuracy of wave energy propagation—a topic last addressed by Rogers *et al.* (2002). Another numerical issue that has received recent attention is the improvement in the discretisation of the geographical domain, something that is increasingly being achieved with the application of unstructured geographical grids (e.g. Sørensen *et al.* 2005 and Hsu *et al.* 2005). The further development of both these numerical topics should be pursued, and their influence on the accuracy of SWAN evaluated.

7.2 Source terms in deep water

Simulation studies performed in deep water and at intermediate depth (e.g. Ris *et al.* 1999 and Rogers *et al.* 2003) have shown that in situations of pure wind sea growth the default version of SWAN yields adequate estimates of significant wave height, but that the spectral mean period is typically underestimated by about 10%. In these studies, the inaccuracy in the mean period has been related to an overestimation of the peak spectral frequency and to an overestimation of the amount of energy in the spectral tail. Under conditions where wind sea is generated over an existent swell field, studies have shown that wind sea growth in the default SWAN model is significantly stronger in the presence of the swell than without it (Hurdle 1998 and Holthuijsen and Booij 2000), an effect that is not supported by field observations (Ardhuin *et al.* 2007). This spurious effect of swell on wind sea growth has been related to the parameterisation of the whitecapping dissipation in terms of the spectrally averaged quantities of mean steepness and mean wave number. In the present study, the unsatisfactory model behaviour outlined above was addressed by investigating the performance of alternative expressions for the source terms active in deep water, namely quadruplet interaction, whitecapping dissipation and wind input.

This study has shown that the reformulation of wave breaking (whitecapping) as a local function in frequency space, as opposed to a one depending on spectral mean quantities, improves the model's overall performance in combined swell and wind sea conditions. To this basic premise a number of refinements are possible: firstly, whitecapping dissipation, which in this study was made a function of the directionally-integrated saturation at a particular frequency, can be made dependent on directional characteristics of the spectrum. For example, the saturation threshold could be normalised by the directional spreading at each frequency, as suggested by Banner *et al.* (2002) and Banner *et al.* (2004), or the dissipation can be defined as a function of the saturation in a particular frequency–direction bin. The latter, directionally-decomposed approach is expected to be a valuable extension with which directionally bi-modal spectra could be dealt with more appropriately.

Secondly, a question that is still actively being researched is whether the dissipation at a particular frequency is indeed only dependent on frequency-local spectral characteristics, or whether it is also influenced by the breaking of waves at other frequencies. The method followed in this study of considering dissipation as local in frequency space is supported by findings of, amongst others, Phillips *et al.* (2001) and Melville and Matusov (2002). On the other hand, Banner *et al.* (1989), Meza *et al.* (2000) and recently Young and Babanin (2006) have shown that dissipation may be due to both breaking at the frequency in question as well as a broadband contribution of dissipation from waves breaking at lower frequencies. If the latter is indeed the case, then the dissipation expression applied in this study could be extended by a term representing the effect of dissipation at lower frequencies, as proposed by Young and Babanin (2006).

Thirdly, an objection that can be raised against the complete decoupling of the generation

and dissipation of wind sea from the presence of non-breaking swell is that some interaction between these spectral regions may indeed exist in nature. Reports of the influence of swell on wind sea growth in nature are varied and sometimes contradictory. In flume experiments, Donelan (1987) found that the presence of following low-frequency waves reduces the growth of the wind-sea part of the spectrum, whereas Mitsuyasu and Yoshida (1989) found that opposing low-frequency waves increases the growth of wind sea. More recently, Kudryavtsev and Makin (2004) have presented a theoretical model for the impact of swell on the atmospheric boundary layer, which can be significant for low wind speeds ($U_{10} < 6$ m/s) combined with steep swell. In the field, however, Ardhuin *et al.* (2007) found that wind sea growth was not effected by opposing swell. From these findings no clear conclusions can be drawn at present. However, since the spurious effect of swell on wind sea growth has been removed, a platform has been created for adding future parameterisations of this effect.

Finally, the dissipation of non-breaking, low frequency waves can be refined. In the present study these spectral components were dissipated using the Komen *et al.* (1984) expression, as in the default SWAN model. However, specific expressions for dissipation by turbulence exist, such as that proposed by Tolman and Chalikov (1996) and recently Ardhuin and Jenkins (2006). Such expressions can be introduced into the dissipation function to yield a more theoretically-based representation of the influence of turbulence processes.

7.3 Source terms in shallow water

It has been known from a number of studies (e.g. Ris *et al.* 1999 and Groeneweg *et al.* 2003) that in the surf zone SWAN predicts significant wave height adequately, but that the details of the spectra and mean period measures tend to be inaccurate. Compared to deep water, where the default model formulations produced a typical underprediction of period measures, in the surf zone, the scatter in the predicted period measures is large, implying modelling uncertainty. Since within the surf zone, the dominant source terms in the action balance are depth-induced breaking and triad nonlinear interaction, these two terms were considered with the view to improving model performance. The main focus of this part of the study was to investigate the impact on model results of replacing the current expression for triad interaction with a more complete, but more computationally expensive expression.

Concerning the practical application of the triad implementations investigated in this study, there is a clear division between variants suitable for operational use and those intended for academic application. Due to its computational efficiency, the LTA is well-suited to operational application. The recalibration proposed in this study appears to provide some improvement in the results of integral parameters. The combined two-equation model of SAM1D and SWAN is defined only for situations with one-dimensional variation in

topography and is computationally expensive. This model combination should therefore be considered as an academic variant. However, there are a few points on which this combined mode can yet be sped up and extended: efficiency can be improved by redefining SAM1D on the same frequency-directional spectral space as that used by SWAN. This would have the advantage that interpolation would be avoided (saving time and improving accuracy) and that fewer directional bins would be required. If knowledge on the spatial propagation of bispectral characteristics would be improved, it may be possible to lift the current restriction of one-dimensional (or one-dimensionally dominant) topographical variation. Further increases in efficiency could be obtained by parameterising the evolution of the bispectrum to some degree. Examples of such expressions are Rasmussen (1998) and Becq-Girard *et al.* (1999), where the bispectrum is made a local function in geographical space, but all interactions (both sum and difference) are retained in the interaction term. Such models lie between the LTA and the complete two-equation models as far as both accuracy and computational speed are concerned.

It was shown in this study that the combination of deep water source terms—in particular quadruplet interaction—with shallow water source terms strongly affects the spectra in the surf zone. Both with the LTA and with the two-equation model, the amount of energy accumulated in the first harmonic is decreased, and additional interaction peaks appear. In the case of the two-equation model, the directional spreading of wave energy was shown to increase significantly. It is hypothesised that the observed behaviour is due to the fact that the expressions for quadruplet interaction used in SWAN are derived for deep water, Gaussian conditions, which are violated in the surf zone. The interplay between the spectral shape created by triad interaction, and the quadruplet interaction term was found to be the largest for the two-equation model. This is because the latter produces shallow water spectra that are, in terms of the high frequency tail, further removed from the self-similar deep water spectral shapes than those produced by the LTA.

Two solutions appear to be available to prevent the unexpected interplay between quadruplet interaction and shallow water spectra. The pragmatic solution pursued in this study is to deactivate quadruplet interaction in the surf zone, where presently-used expressions are invalid, and where theoretical studies show these interactions to go to zero. An alternative, more fundamental approach would be to include quadruplet (cubic) interactions alongside the quadratic interaction in the derivation of a stochastic surf zone model. This would result in a system of equations including the spectrum, bispectrum and trispectrum, with an inherent transition from quadruplet nonlinearity to triad nonlinearity moving towards the coast.

Chapter 8

Recommendations

In this study various ways were investigated to improve the accuracy of the wind wave model SWAN. From the results of this investigation, and on the basis of the conclusions drawn in the previous chapter, a number of recommendations can be made. In terms of the numerics of SWAN, the following is recommended:

(a) Considering the analysis carried out on convergence-enhancing methods available to stabilise the iteration behaviour of SWAN during stationary simulation, it is recommended to maintain the use of the action limiter in deep and intermediate water depths. Although the iteration behaviour can be poor, this method allows relatively fast convergence and does not significantly affect the converged solution in either deep water or in water of finite depth.

(b) Since it was found that the action limiter can significantly increase the number of iterations required for convergence in the surf zone, it is recommended that the limiter be deactivated here. This implies that the quadruplet interaction term, which the limiter is designed to stabilise, should also be deactivated in the surf zone. The deactivation of the quadruplet term (as currently formulated) in the surf zone is also to be recommended on the basis of model physics. It is recommended to use the Ursell number as a robust criterion for the deactivation of both the quadruplet term and the action limiter.

(c) Frequency-dependent under-relaxation has been shown to be an effective way of smoothing the iteration behaviour of SWAN. However, since under-relaxation was found to significantly slow down the speed of convergence, it is not recommended to apply this technique in operational wave modelling.

(d) The default convergence criteria used in SWAN, which are based on the slope of the curve traced by successive iterates (iteration curve), has been shown to be insufficient

in locating the actual point of model convergence. It is recommended to use the stopping criterion which is based on the second derivative or curvature of the iteration curve.

(e) The implementation of stricter convergence criteria has highlighted the fact SWAN requires a relatively large number of iterations to converge. Therefore, a need has been identified to reduce the time required to reach convergence. It is recommended *to investigate ways to either reduce the number of iterations required or to minimise the time required per iteration.*

Considering the study into the deep water source terms of SWAN, the following recommendations are made:

(f) It is not recommended to replace the DIA approximation for quadruplet interaction by an exact expression (such as the WRT) in operational modelling aplications, since the computational cost of using the latter proves to outweigh the gains in accuracy. It is, however, recommended to investigate the optimalisation and speeding-up of such exact expressions, so that they can be applied in selected cases.

(g) It is recommended to replace the whitecapping expression of Komen *et al.* (1984), which contains strong dependencies on mean spectral qantities, by the investigated saturation-based whitecapping expression, in which the dissipation of the breaking portion of the spectrum is dependent on frequency-local variables only.

(h) The decoupling of the dissipation of the swell and wind sea frequencies was shown to improve the performance of SWAN in combined swell and wind sea conditions. This decoupling can also be extended to the directional space. It is recommended to investigate the effect of decoupling the dissipation across directions, basing it on the level of saturation of individual frequency–directional bins.

(i) Considering recent theoretical and experimental findings (e.g. Kudryavtsev and Makin (2004) and Young and Babanin (2006)), it is recommended to investigate the effect of including broadband input and dissipation features in the wind input and whitecapping source terms.

(j) There is potential to model the dissipation of the non-breaking part of the spectrum in SWAN in greater detail. It is recommended to implement an advanced turbulence-based dissipation formulation (e.g. Ardhuin and Jenkins 2006) for the lower frequency, non-breaking part of the spectrum. This will provide a source of dissipation in addition to the dissipation caused by the breaking (whitecapping) of higher frequency spectral components.

(k) It is recommended to investigate and correct the sources of the difference between model results and observations over very short fetches. These differences may have

their root in the quality of the wind forcing, the energy transfer by the wind input expression, the level of dissipation in the saturation-based model or in the wave observations.

Considering the investigation into the use of alternative source term expressions for surf zone physics, the following recommendations are made:

(l) It is recommended to replace the LTA triad expression with one that would include the transfer of energy to subharmonics and that would give a better estimate of energy levels at the first superharmonic. A basis for such a new model could be the SAM1D model investigated in this study.

(m) It was found that the expressions currently used for modelling quadruplet interaction give unexpected results in the surf zone, where they are not strictly valid and where spectra are strongly altered by surf zone physics. It is recommended to derive a stochastic expression for the transition of cubic (quadruplet) to quadratic (triad) nonlinearity that would yield valid results both in the Gaussian and non-Gaussian wave fields. The basis for such a stochastic model could be the deterministic expressions derived by Janssen (2006).

(n) In this study it was found that the SAM1D model yields directional spreading results that appear to be too narrow. It is recommended to investigate and correct the causes for this inaccuracy.

(o) It is recommended to extend the stochastic models of Janssen (2006) (SAM1D and SAM2D) to a fully isotropic form.

Appendix A

Source term scaling

Below, the scalability of the whitecapping and wind input expressions (4.13) and (4.15) is demonstrated for weakly and strongly forced waves in deep and shallow water.

A.1 Weakly forced waves

For weakly forced waves, the wind input expression is taken to be of the form (4.2), which has the following scaling:

$$
\begin{aligned}
S_{in,Snyder}(\sigma, \theta) &\propto \frac{u_*}{c} \sigma E(\sigma, \theta) \\
&\propto k E(\sigma, \theta) \quad , \quad \text{using} \ \ c = \sigma/k \ .
\end{aligned}
\tag{A.1}
$$

Under weak wind forcing, the whitecapping expression (4.13) has been parameterised to have $p = 2$, so that its proportionality becomes:

$$
\begin{aligned}
S_{wc,p=2}(\sigma, \theta) &\propto [B(k)] \ g^{\frac{1}{2}} k^{\frac{1}{2}} E(\sigma, \theta) \\
&\propto \left[g^{-\frac{1}{2}} k^{\frac{1}{2}} \right] g^{\frac{1}{2}} k^{\frac{1}{2}} E(\sigma, \theta) \\
&= k E(\sigma, \theta) \ .
\end{aligned}
\tag{A.2}
$$

For the scaling of $B(k)$, expression (4.14) is applied, in combination with the Jacobian transformation $E(\sigma) = \frac{1}{c_g} F(k)$ and the spectral shape of $F(k) \propto k^{-2.5}$ proposed by Resio *et al.* (2001). From (A.1) and (A.2) it is seen that wind input and whitecapping dissipation

177

Ochi, M. K. and W. C. Wang (1984). Non-gaussian characteristics of coastal waves. *Proc. 19th Int. Conf. on Coastal Engineering*, 516–531.

Peirson, W. L. and S. E. Belcher (2005). Growth response of waves to the wind stress. *Proc. 29th Int. Conf. Coastal Eng.*, 667–676.

Peirson, W. L., A. W. Garcia, and S. E. Pells (2003). Wave attenuation due to opposing wind. *J. Fluid Mech. 407*, 345–365.

Phillips, O. M. (1957). On the generation of waves by turbulent wind. *J. Fluid Mech. 2*, 417–445.

Phillips, O. M. (1985). Spectral and statistical properties of the equilibrium range in wind-generated gravity waves. *J. Fluid Mech. 156*, 505–531.

Phillips, O. M., F. L. Posner, and J. P. Hansen (2001). High range resolution radar measurements of the speed distribution of breaking events in wind-generated ocean waves: Surface impulse and wave energy dissipation. *J. Phys. Oceanogr. 31*, 450–460.

Pierson, W. J. and L. Moskowitz (1964). A proposed spectral form for fully developed wind seas based on the similarity theory of S. A. Kitaigorodskii. *J. Geophys. Res. Vol. 69*, 5181–5190.

Pierson, W. J., G. Neumann, and R. W. James (1955). Practical methods for observing and forecasting ocean waves by means of wave spectra and statistics. *Hydrogrphic Office, U.S. Navy, H.O. Pub. 603*.

Plant, W. J. (1982). A relation between wind stress and wave slope. *J. Geophys. Res. Vol. 87, No. C4*, 1961–1967.

Press, W. H., B. P. Flannery, S. A. Teukolsky, and W. T. Vetterling (1993). *Numerical recipes in Fortran 77. The art of scientific computing (2nd edition)*. Cambridge University Press.

Rasmussen, J. H. (1998). Deterministic and stochastic modelling of surface gravity waves in finite depth, Ph.D Thesis. Technical report, Institute of Hydronamics and Hydraulic Engineering (ISVA), Denmark.

Resio, D. T., C. E. Long, and C. L. Vincent (2004). Equilibrium-range constant in wind-generated wave spectra. *J. Geophys. Res. Vol. 109, C01018*, doi:10.1029/2003JC001788.

Resio, D. T. and W. Perrie (1991). A numerical study of nonlinear energy fluxes due to wave-wave interactions, part I, Methodology and basic results. *J. Fluid Mech. 223*, 609–629.

Resio, D. T., J. H. Pihl, B. A. Tracy, and C. L. Vincent (2001). Nonlinear energy fluxes and the finite depth equilibrium range in wave spectra. *J. Geophys. Res. Vol. 106, No. C4*, 6985–7000.

Ris, R. C. (1997). Spectral modelling of wind waves in coastal areas, Ph.D Thesis. Technical report, Fac. of Civil Engineering, Delft University of Technology.

Ris, R. C. (1999). Model convergence of SWAN in the Westerschelde estuary. Technical report, WL|Delft Hydraulics Report H3496.

Ris, R. C., L. H. Holthuijsen, and N. Booij (1999). A third-generation wave model for coastal regions, Part II, Verification. *J. of Geophys. Res. 104 (C4)*, 7667–7682.

Ris, R. C., L. H. Holthuijsen, J. M. Smith, N. Booij, and A. R. van Dongeren (2002). The ONR virtual testbed for coastal and oceanic wave models. *Proc. 28th Int. Conf. Coastal Eng.*, 380–391.

Rogers, W. E., P. A. Hwang, and D. W. Wang (2003). Investigation of wave growth and decay in the SWAN model: Three regional scale applications. *J. Phys. Oceanogr. 33*, 366–389.

Rogers, W. E., J. M. Kaihatu, L. Hsu, R. E. Jensen, J. D. Dykes, and K. T. Holland (2007). Forecasting and hindcasting waves with the SWAN model in the Southern California Bight. *Coastal Engineering 54*, 1–15.

Rogers, W. E., J. M. Kaihatu, H. A. H. Petit, N. Booij, and L. H. Holthuijsen (2002). Diffusion reduction in an arbitrary scale third generation wind wave model. *Ocean Engineering 29*, 1357–1390.

Schneggenburger, C., H. Günther, and W. Rosenthal (2000). Spectral wave modelling with non-linear dissipation: validation and apllications in a coastal tidal environment. *Coastal Engineering 41*, 201–235.

Snyder, R. L., F. W. Dobson, J. A. Elliot, and R. B. Long (1981). Array measurements of atmospheric pressure fluctuations above surface gravity waves. *J. Fluid Mech. 102*, 1–59.

Sørensen, O. R., H. Kofoed-Hanssen, M. Rugbjerg, and L. S. Sørensen (2005). A third-generation spectral wave model using an unstructured finite volume technique. *Proc. 29th Int. Conf. Coastal Engineering, ASCE*, 894–906.

Sverdrup, H. V. and W. H. Munk (1944a). Breakers and surf: Principles in forecasting. *Hydrogrphic Office, U.S. Navy, Publ. No. 235.*

Sverdrup, H. V. and W. H. Munk (1944b). Wind waves and swell: Principles in forecasting. *Hydrogrphic Office, U.S. Navy, Misc. 11, 275.*

Taylor, P. A. and R. J. Lee (1984). Simple guidelines for estimating wind speed variations due to small scale topographical features. *Climat. Bull. Vol. 18*, 3–32.

Toba, Y. (1973). Local balance in the air-sea boundary processes. III. On the spectrum of wind waves. *J. Oceanogr. Soc. Japan 29*, 209–220.

Tolman, H. L. (1991). A third-generation model for wind waves on slowly varying, unsteady and inhomogeneous depths and currents. *J. Phys. Oceanogr. 21*, 782–797.

Tolman, H. L. (1992). Effect of numerics on the physics in a third generation wind-wave model. *J. Phys. Oceanogr. Vol. 22, No.10*, 1095–1111.

Tolman, H. L. (2002). Limiters in third-generation wind wave models. *Global Atmosphere and Ocean System 8*, 67–83.

Tolman, H. L. and D. Chalikov (1996). Source terms in a third-generation wind-wave model. *J. Phys. Oceanogr. 26(11)*, 2497–2518.

Tracy, B. A. and D. T. Resio (1982). Theory and calculation of the nonlinear energy transfer between sea waves in deep water. Technical report, WIS Rep. 11, U.S. Army Engineer Waterways Experiment Station, 48 pp.

UN-Oceans (2007). United Nations Atlas of the Oceans. *www.oceanatlas.org*.

Van der Westhuysen, A. J., M. Zijlema, and J. A. Battjes (2005). Improvement of the numerics and deep-water physics in an academic version of SWAN. *Proc. 29th Int. Conf. Coastal Engineering, ASCE*, 855–867.

Van der Westhuysen, A. J., M. Zijlema, and J. A. Battjes (2007). Nonlinear saturation-based whitecapping dissipation in SWAN for deep and shallow water. *Coastal Engineering 54*, 151–170.

Van Vledder, G. P. (2001a). Extension of the discrete interaction approximation for computing nonlinear quadruplet wave-wave interactions in operational wave prediction models. *Proc. 4th Int. Symp. on Ocean Wave Meas. and Analysis*.

Van Vledder, G. P. (2001b). Iteration behaviour of SWAN 40.11 in the markermeer. Technical report, Alkyon Report A637.

Van Vledder, G. P. (2005a). Numerical wave modelling in the Dutch coastal waters. *Proc. ICECOAST 2005 Symposium, Höfn, Iceland*.

Van Vledder, G. P. (2005b). The WRT method for the computation of non-linear four-wave interactions in discrete spectral wave models. *Coastal Engineering 53*, 223–242.

Van Vledder, G. P. and M. Bottema (2003). Improved modelling of nonlinear four-wave interactions in shallow water. *Proc. 28th Int. Conf. Coastal Engineering, ASCE*, 459–471.

Van Vledder, G. P., T. H. C. Herbers, R. J. Jensen, D. T. Resio, and B. A. Tracy (2000). Modelling of non-linear quadruplet wave–wave interactions in operational wave models. *Proc. 27th Int. Conf. Coastal Engineering, ASCE*, 797–811.

WAMDI Group (1988). The WAM model - a third generation ocean wave prediction model. *J. Phys. Oceanogr. 18*, 1775–1810.

Webb, D. J. (1978a). Non-linear transfers between sea waves. *Deep-Sea Research 25(3)*, 279–298.

Webb, D. J. (1978b). The wave-wave interaction machine. *Turbulent fluxes through the sea surface, Wave dynamics and prediction. Proc. NATO Symposium, Sept. 1977, Marseille*, 335–345.

Wesseling, P. (1992). *An introduction to multigrid methods*. John Wiley and Sons, Chichester, 269pp.

Wu, J. (1982). Wind-stress coefficients over sea surface from breeze to hurricane. *J. of Geophys. Res. 87 (C12)*, 9704–9706.

Yan, L. (1987). An improved wind input source term for third generation ocean wave modelling. Technical report, Rep. No. 87-8, Royal Dutch Meteor. Inst.

Young, I. R. (1999). *Wind generated ocean waves.* Elsevier Ocean Engineering Book Series, 288pp.

Young, I. R. and A. V. Babanin (2006). Spectral distribution of energy dissipation of wind-generated waves due to dominant breaking. *J. Phys. Oceanogr 36*, 376–394.

Young, I. R. and G. P. van Vledder (1993). A review of the central role of nonlinear interactions in wind-wave evolution. *Phil. Trans. Royal Soc. London , A., Vol. 342*, 505–524.

Young, I. R. and L. A. Verhagen (1996a). The growth of fetch-limited waves in water of finite depth. Part 1. Total energy and peak frequency. *Coastal Engineering 29*, 47–78.

Young, I. R. and L. A. Verhagen (1996b). The growth of fetch-limited waves in water of finite depth. Part 2. Spectral evolution. *Coastal Engineering 29*, 79–99.

Zakharov, V. E. (1999). Statistical theory of gravity and capillary waves on the surface of a finite-depth fluid. *Eur. J. Mech. B/Fluids 18*, 327–344.

Zijlema, M. (2005). *Parallelization of a nearshore wind wave model for distributed memory architectures. In: Parallel Computational Fluid Dynamics—Multidisciplinary Applications, G. Winter, A. Ecer, J. Periaux, N. Satofuka and P. Fox, Eds.* Elsevier.

Zijlema, M. and A. J. Van der Westhuysen (2005). On convergence behaviour and numerical accuracy in stationary SWAN simulations of nearshore wind wave spectra. *Coastal Engineering 52*, 237–256.

List of Tables

List of Figures

193

Nomenclature

This section summarises the most common symbols used in this thesis.

Roman letters

a	Wave amplitude
B	Azimuthal-integrated spectral saturation
Br	Threshold saturation level
$C_{\sigma,\sigma}^{\lambda,\lambda}$	Bispectrum in the SAM1D model
C_{JON}	Friction coefficient of Hasselmann *et al.* (1973)
C_{ds}, C'_{ds}	Proportionality coefficients in whitecapping formulations
C_{nl4}	Proportionality coefficient in DIA of Hasselmann *et al.* (1985)
c	Phase velocity
$\vec{c}_g$	Group velocity vector
c_x, c_y	Components of geographic velocity vector $\vec{c}_g + \vec{U}$
c_σ, c_θ	Propagation velocities in spectral space (σ, θ)
D	Rate of total energy dissipation per unit horizontal area
D_σ	Dissipation due to depth-indiced breaking in SAM1D
d	Time-averaged water depth
$\tilde{d}$	Water depth non-dimensionalised in terms of U_{10}
E	Variance density
E_{tot}	Total variance
E^*	Total variance non-dimensionalised in terms of u_*
$\tilde{E}$	Total variance non-dimensionalised in terms of U_{10}
F	One-dimensional wavenumber spectrum
f	Frequency
f_{br}	Transition function between breaking and non-breaking dissipation modes
f_p	Peak frequency
f_p^*	Peak frequency non-dimensionalised in terms of u_*
$\tilde{f}_p$	Peak frequency non-dimensionalised in terms of U_{10}
G	Coupling coefficient in the quadruplet expression of Hasselmann (1962)
g	Gravitational acceleration
H_b	Breaking wave height

H_{m0}	Significant wave height, defined as $H_{m0} = 4\sqrt{m_0}$
H_r	Reference wave height
H_{rms}	Root-mean-square wave height, defined as $H_{rms} = \sqrt{8m_0}$
I	Identity matrix
i	Imaginary number
J	Interaction coefficient in the LTA exprression
k	Wavenumber
$\tilde{k}$	Spectral mean wavenumber
m	Parameter of the Alves and Banner (2003) whitecapping expression
$m_n, \tilde{m}_n$	Moments of the variance density and flux spectra respectively
N	Action density
n	Parameter of the Alves and Banner (2003) whitecapping expression *or* time level (see Superscripts)
p	Parameter of the Alves and Banner (2003) and saturation-based whitecapping expressions
p_0	Parameter of the Alves and Banner (2003) whitecapping expression
q	Parameter of the Komen *et al.* (1984) whitecapping expression
r	Parameter of the Komen *et al.* (1984) whitecapping expression *or* coefficient of linear correlation
r_n	Frequency weighting factors for depth-induced breaking dissipation
S_{bot}	Source term for bottom friction dissipation
$S_{dis,break}$	Dissipation contribution due to wave breaking
$S_{dis,non-break}$	Dissipation contribution by other means than breaking
S_{in}	Source term for wind input
S_{nl3}	Source term for triad interaction
S_{nl3}^+, S_{nl3}^-	Positive and negative contributions to spectral density by triad interactions
S_{nl4}	Source term for quadruplet interaction
S_{surf}	Source term for depth-induced breaking
S_{tot}	Sum of all source terms
S_{wc}	Source term for whitecapping
s	Iteration level (see Superscripts)
$\tilde{s}$	Spectral mean wave steepness
$\tilde{s}_{PM}$	Spectral mean wave steepness of Pierson Moskowitz spectrum
T_p	Peak period
T_{m01}	Mean wave period, defined as $T_{m01} = m_0/m_1$
t	Time
Δt	Time step
$\vec{U}$	Mean current velocity vector
Ur	Ursell number
U_z	Wind speed at an elevation of z m
u_*	Friction velocity
$W_{\sigma,\sigma}^{\lambda,\lambda}$	Coupling coefficient in the SAM1D model
w	Shape factor in the saturation-based whitecapping expression

X	Fetch
X^*	Fetch, non-dimensionalised in terms of u_*

Greek letters

α	Magnitude of frequency-dependent under-relaxation
α_{BJ}	Proportionality coefficient in the Battjes and Janssen (1978) breaker model
α_{CR}	Proportionality coefficient in the CRAD breaker model
α_{EB}	Proportionality coefficient in the LTA expression
α_{PM}	Phillips constant for a Pierson-Moskowitz spectrum
$\alpha_{P,L,R,T,B}$	Coefficient in matrix system for the action balance equation
$b_{P,L,R,T,B}$	Source term entries in matrix system for the action balance equation
β	Dimensionless wind growth rate
$\beta(\sigma, \sigma)$	Biphase (phase of the bispectrum)
β_D, β_{NL}	Relaxation coefficients in the SAM1D model
δ	Dirac delta function
δS_{nl}	Contribution to spectral density by quadruplet interaction
$\Delta x, \Delta y$	Increments in geological x- and y- space
$\Delta \theta, \Delta \sigma$	Increments in spectral θ- and σ- space
Δf	Increment in frequency space
ε_C	Limiting curvature of the iteration curve of H_{m0}
$\varepsilon_H^a, \epsilon_T^a$	Limiting values for the absolute change in H_{m0} and T_{m01}
$\varepsilon_H^r, \epsilon_T^r$	Limiting values for the relative change in H_{m0} and T_{m01}
η, ν	Parameters determined the blend between central and upwind discretisation in σ and θ spaces respectively
γ	Magnitude of the action density limiter
γ_{BJ}	Breaking criterion in the Battjes and Janssen (1978) breaker model
γ_{CR}	Breaking criterion in the CRAD breaker model
λ	Longshore wave number in the SAM1D model or interaction parameter of the DIA
$\Lambda_{\sigma,\sigma}^{\lambda,\lambda}$	Phase mismatch between wave components in the SAM1D model
$\mu_{\sigma,\sigma}^{\lambda,\lambda}$	Relaxation term in the SAM1D model
Φ	Polar wavenumber spectrum
σ	Intrinsic radian frequency
$\tilde{\sigma}$	Spectral mean intrinsic radian frequency
$\sigma_{min}, \sigma_{max}$	Lower and upper bounds of the radian frequency space
τ	Pseudo time step
θ	Wave direction
ξ_σ^λ	Flux spectrum in the SAM1D model

Acronyms

CRAD	Consistent Rayleigh Dissipation
DIA	Discrete Interaction Approximation

JONSWAP   Joint North Sea Wave Project
LTA   Lumped Triad Interaction
SAM   Stochastic Angular-spectrum Model
SWAN   Simulating WAves in the Nearshore
WAM   WAve Model
WRT   Webb-Resio-Tracy (quadruplet interaction model)

Subscripts

i, j Grid counters in x and y spaces
l, m Grid counters in σ and θ spaces
x, y x and y directions, respectively
θ, σ θ and σ directions, respectively
P, L, R, T, B Relative position (centre, left, right, top and bottom) in sub-block of
                matrix system for the action balance equation

Superscripts

$*$ Nondimensional in terms of u_*
$\sim$ Nondimensional in terms of U_{10}
n Time level
s Iteration level

Other

$\nabla_{\vec{x}}$ Horizonal gradient operator

Acknowledgments

When reading the history of scientific development, one realises that the great names of science did not develop their theories or make their discoveries in isolation. Instead, they where surrounded by colleagues and competitors, who all contributed to the final product to a lesser or greater extent (but who were finally beaten to the publisher's office!). My undertaking of this PhD study was no different. During the course of this project, I have been fortunate to meet and work with some of the best researchers in my field. I am therefore deeply indebted to many people for the success of this project.

Firstly, I would like to express my gratitude to Rijkswaterstaat Rijksinstituut voor Kust en Zee (RIKZ) for financing this project, and for Leo Holthuijsen and Guus Stelling for conceiving and arranging it. I have been very fortunate to be one of the last PhD students to be supervised by Jurjen Battjes. I am very thankful to him for his guidance and constructive criticism on my work. I am also grateful to Marcel Zijlema for guiding me through the SWAN source code and for his expert knowledge of numerics. I would like to sincerely thank my User's Group committee, comprising Marcel Bottema, Carolien Gautier, Jacco Groeneweg, Annette Kieftenburg and Gerbrant van Vledder, who helped to steer the course of this project. In addition, I would like to thank all the participants of the WISE Group, and in particular Alex Babanin, for many stimulating discussions and useful comments. I also have the support staff of the Fluid Mechanics Section, in particular Otti Kievits, Andre Brouwer and Arie, to thank for the smooth execution of this project.

But living abroad has added additional challenges (and pleasures) to this endeavour. In this regard, friends and colleagues have helped much to smooth the ride. First of all, I would sincerely like to thank Hans and Betty Mulder, who have taught me the ropes of the Netherlands, and who have offered me a home away from home. Then I would like to thank my former colleagues and fellow PhD students at the sections of Fluid Mechanics and Hydraulic Engineering for moral support and countless social activities (ranging from snowball fights to cycling and wadlopen expeditions): Alexander, Ad, both Basses, Bram, Claire, David, Francesca, Frederico, Gerben, Guus, Han, Harmen, Jaap, Jasper, Julie, Ketut, Maarten, Marije, Martijn, Michel, Olga, Petra, Rob, Robert Jan, Sander, Stephan, Tim, Walter and both Wims. Thanks is also due to my new colleagues at WL | Delft Hydraulics, for their support during the final stage of writing this thesis. Finally, I would

like to expresses my deepest gratitude to Annemarie for her patience and loving support during this challenging period in my life.

André van der Westhuysen

Delft, August 2007.

Curriculum Vitae

André van der Westhuysen was born is East London, South Africa in 1975. He attended secondary school at Hoërskool Tygerberg in Parow and at Hoërskool Sentraal in Bloemfontein. He received his bachelor's degree in Civil Engineering *cum laude* from the University of Stellenbosch in 1998. During this time he was a member of the organising committee for a programme promoting studies in engineering, and in his final year was the chairman of the Engineering Student Council.

In 1999, he started working at the CSIR, the national scientific research council of South Africa, in Stellenbosch. Here he conducted applied research into numerical wave models, applied wave models wave climate studies and set up wave prediction systems. He also conducted numerical ship manoeuvring and ship motion model studies for harbour design and for decision support systems. During his time at the CSIR, André completed a master of science degree in Civil Engineering part-time through the University of Stellenbosch. He was awarded this degree *cum laude* in 2002, with a thesis entitled: 'The application of the wind wave model SWAN to a selected field case on the South African southeast coast.'

In 2002, André started his PhD in numerical wave model development at the Environmental Fluid Mechanics section of the Faculty of Civil Engineering and Geosciences at the Delft University of Technology. The results of his work are this thesis, four refereed journal articles, two of which have already been published, and two conference proceedings. The results of this work have also been presented at various international workshops on numerical wave modelling. He is currently a researcher and specialist consultant at WL | Delft Hydraulics.

Alongside his scientific work, André is an avid reader, and enjoys travelling and listening to music.